

Spectroscopy and nuclear dynamics of starburst galaxies

Spectroscopy and nuclear dynamics of starburst galaxies

Proefschrift

ter verkrijging van
de graad van Doctor aan de Universiteit Leiden,
op gezag van de Rector Magnificus prof. mr. P. F. van der Heijden,
volgens besluit van het College voor Promoties
te verdedigen op woensdag 11 januari 2012
klokke 13:45 uur

door

Liesbeth Vermaas

geboren te Nieuw-Dordrecht
in 1977

Promotiecommissie

Promotor: Prof. dr. F. P. Israël
Co-promotor: Dr. P. P. van der Werf

Overige leden: Dr. K. M. Dasyra Observatoire de Paris
Prof. dr. H. J. A. Röttgering
Prof. dr. A. G. G. M. Tielens
Prof. dr. K. H. Kuijken

Cover photo: the VLT Laser Guide Star in operation at Paranal in January 2007;
credit: ESO/H.H.Heyer.

Table of contents

1	Introduction	1
1.1	Starburst galaxies	2
1.2	Ultraluminous Infrared Galaxies (ULIRGs)	2
1.3	This thesis	4
1.4	Conclusions and outlook	5
2	The asymmetric nuclear region of M83 and its off-centre starburst	7
2.1	Introduction	9
2.2	Observations and data reduction	10
2.2.1	SINFONI observations	10
2.2.2	SINFONI data reduction	11
2.2.3	IRAC2 data	11
2.2.4	VLA data	12
2.3	Results	13
2.3.1	Morphology of the nuclear region of M83	13
2.3.2	Near-IR continuum	14
2.3.3	Br γ emission	14
2.3.4	[FeII] emission	14
2.3.5	H ₂ emission	15
2.3.6	Spectra	15
2.4	Analysis	17
2.4.1	Extinction	17
2.4.2	Star forming regions	20
2.4.3	Comparison with 15 GHz radio emission	27
2.4.4	[FeII] emission and supernova activity	28
2.4.5	H ₂ emission	31
2.5	Kinematics	34
2.5.1	Gas velocity field	34
2.5.2	Stellar velocity field	34
2.5.3	Rotating ring structure	36
2.5.4	Nature of the optical peak	37
2.6	Summary	38
3	The nuclear dynamics of Arp 220	43
3.1	Introduction	45
3.2	Observations and data reduction	47
3.3	Results	47

3.3.1	Spectra	49
3.3.2	Gas kinematics	49
3.3.3	Stellar kinematics	51
3.3.4	Velocity profiles	51
3.4	Discussion: nuclear dynamics	53
3.4.1	Mass estimate from stellar kinematics	53
3.4.2	Mass estimate from gas kinematics	54
3.4.3	Mass to light ratio	55
3.5	Conclusions	56
4	Nuclear stellar dynamics and K-band mass-to-light ratios of Ultraluminous Infrared Galaxies	61
4.1	Introduction	63
4.2	Observations and data reduction	64
4.3	Results and analysis	66
4.3.1	Method	66
4.3.2	IRAS 01388-4618	68
4.3.3	IRAS 05189-2524	70
4.3.4	IRAS 09111-1007	71
4.3.5	IRAS 17208-0014	71
4.3.6	IRAS 20551-4250	74
4.4	Discussion	75
4.4.1	Uncertainties in mass determinations	75
4.4.2	Uncertainties in luminosity determinations	75
4.4.3	M/L_K : expectations and implications	76
4.4.4	An evolutionary path with M/L_K ?	76
4.5	Conclusions and outlook	77
5	Nuclear gas dynamics of Ultraluminous Infrared Galaxies	79
5.1	Introduction	81
5.2	Observations and data reduction	82
5.3	Results and analysis	84
5.3.1	Spectra and images	84
5.3.2	Tilted ring fitting	84
5.3.3	Rotation curves, dynamical masses and M/L_K	84
5.3.4	IRAS 01388-4618	88
5.3.5	IRAS 05189-2524	90
5.3.6	IRAS 09111-1007	92
5.3.7	IRAS 17208-0014	94
5.3.8	IRAS 20551-4250	96
5.4	Discussion	99
5.4.1	Rotation curve fitting and the role of the effective radius, R_{eff}	99
5.4.2	Mass from gas dynamics vs. mass from stellar dynamics	99

5.4.3	ULIRG evolution: starburst ages and mass fractions	101
5.4.4	ULIRG evolution: the fundamental plane	101
5.5	Conclusions	103
	Nederlandse samenvatting	107
	Curriculum vitae	113
	Nawoord	115

Introduction

1

1.1 Starburst galaxies

The term ‘starburst’ denotes a period of star formation at a very high rate. In a normal spiral galaxy, star formation occurs in the spiral arms with a rate of $\sim 1 M_{\odot} \text{yr}^{-1}$ (for the whole galaxy), while in a starburst galaxy this rate can be $10 - 100 M_{\odot} \text{yr}^{-1}$ for a normal starburst galaxy, up to $10^2 - 10^3 M_{\odot} \text{yr}^{-1}$ in the more extreme (merging) galaxies, like Ultraluminous Infrared Galaxies (ULIRGs, see section below). One thing they have in common is that the burst can only be sustained for a limited period of time, typically $10^7 - 10^8$ years, until the gas supply for star formation is exhausted.

Starbursts are commonly associated with galaxy interactions and can occur in locations spread over the whole galaxy, but often the burst is confined to a region of a few $\times 100$ pc near the galaxy nucleus. In most cases collisions of clouds are the scene of enhanced star formation, with the collisions occurring either in perturbed disks or between clouds originally belonging to different galaxies. In some cases the interacting galaxies are far apart and the disks are rather undisturbed, so that internal effects of tidal stress must be responsible. One example of how galaxy interaction can induce star formation without signs of direct merging is in the presence of a bar: the companion induces the formation of a bar, which in some cases can last much longer than the encounter itself. This can help substantial amounts of gas from the outer parts to loose angular momentum and reach the nuclear region, possibly leading to a nuclear starburst. Another example is a companion that can perturb the disk potential causing the gas to collapse. This is supported by the fact that the regions in spiral galaxies where star formation is observed coincide with regions in which gas is unstable by the Toomre (dynamical) criterion (Toomre 1964).

A starburst can be recognised by several characteristics. Starbursts have spectra similar to those of HII-regions, with strong recombination lines, e.g. the Balmer, Paschen and Brackett series. They can be luminous in the blue and ultraviolet (UV), because of the contribution from massive young stars, but also, and even more, in the infrared, because of the dusty environment in star forming regions, with the dust absorbing the UV radiation and re-radiating it at longer wavelengths. There may be strong radio continuum emission as well, in the form of thermal radiation from HII-regions or non-thermal synchrotron radiation from supernova remnants.

The absorption of radiation by dust is a serious problem when observing starburst galaxies. The solution is to move to infrared wavelengths, the near-infrared ($1.0\text{-}2.5 \mu\text{m}$), where extinction is less but stellar light is still observed, or at longer wavelengths in the mid- and far-infrared, where it is possible to look further into the dust.

1.2 Ultraluminous Infrared Galaxies (ULIRGs)

Ultraluminous infrared galaxies (ULIRGs) share the definition that they are very luminous and emit the bulk of their energy in the infrared, with $L_{\text{IR}} \geq 10^{12} L_{\odot}$, but they have much more in common. This luminosity criterion selects merging galaxies or merger remnants with large amounts of molecular gas, while the infrared luminosity is predominantly powered by

star formation rates as high as $10^2 - 10^3 M_{\odot} \text{yr}^{-1}$, although a central AGN may also contribute to the nuclear power.

ULIRGs can be divided into two groups by their infrared colours, often expressed by the ratio of flux in the $25 \mu\text{m}$ and the $60 \mu\text{m}$ bands: “cool” ULIRGs have a typical ratio $f_{25}/f_{60} \leq 0.10$, whereas “warm” ULIRGs have $f_{25}/f_{60} > 0.2$. The warm ULIRGs have more compact and brighter nuclei compared to cool ULIRGs.

It has been proposed that cool ULIRGs are dust-obscured precursors of Quasi Stellar Objects (QSOs) (e.g. Sanders et al. 1988). On this evolutionary path, the AGN disperses the dust and gas, shifting the bulk of energy toward shorter wavelengths (the cool ULIRG gradually becomes a warm ULIRG), AGN feedback terminates star formation, and the ULIRG eventually becomes an optically bright QSO. This is also a conceptually simple explanation for the relation that has been found between stellar mass and black hole mass of spheroidal systems like bulges of galaxies and ellipticals. This mechanism is explained in the next section.

ULIRGs and the AGN-starburst connection

It has been discovered that in spheroidal systems, the mass of the central black hole and the stellar velocity dispersion (or black hole mass and stellar mass) are related, suggesting a relation between starburst and AGN, the AGN-starburst connection (Magorrian et al. 1998, Ferrarese & Merritt 2000, Gebhardt et al. 2000). This relation should be established at the time of their formation. ULIRGs have high star formation rates, $10^2 - 10^3 M_{\odot} \text{yr}^{-1}$, and often host an AGN as well, and since we assume them to be ellipticals in formation, we may consider this process to be similar to that of the formation of old ellipticals in earlier times. Several studies have addressed this topic, indicating that local ULIRGs evolve into intermediate mass ellipticals rather than giant ellipticals (e.g., Genzel et al. 2001, Tacconi et al. 2002). Direct influence of the black hole on star formation would be the key to establishing the relation between the black hole mass and the stellar mass. The black hole grows by consuming its environment and stellar content grows by vigorous star formation. At some point the black hole becomes so massive that its feedback expels the gas, causing star formation to stop. But the dispersal of the gas also stops the growth of the black hole. The stellar mass is then given by the integral of star formation over time during the ULIRG phase, the black hole mass by the integral of accretion rate over time.

In the beginning of the merging process, the gas components flow towards the centre of the system very efficiently because the gas can dissipate mechanical energy, while the stellar components merge much slower by dynamical friction, the stars do not collide themselves. It has been shown that in ULIRGs the gas rotates regularly in a disk or a ring, showing a rotation that flattens at about 0.5 kpc or smaller (e.g., Downes & Solomon 1998). Such a molecular disk is initially stable against star formation, but as surface density continues to build up, it will get unstable and start to form stars. Because of the local conditions, the critical density that needs to be reached for instability is very high and when star formation starts, this will be in a burst at a very high rate. This process, too, can destroy the disk and disperse the gas, and the AGN that was previously hidden, becomes visible. This theory is described by Elmegreen (1994).

ULIRGs and the fundamental plane

Elliptical galaxies are a class of objects with surface brightness that can be well described by the surface brightness and a characteristic radius. The De Vaucouleurs' $r^{1/4}$ law fits this profile very well: $I(r) = I_0 \exp(-r/r_0)^{1/4}$. It is common to use the effective radius R_{eff} , the radius that contains half of the total light, and the surface brightness at this radius, I_{eff} . Together with the central stellar velocity dispersion, σ_0 , these parameters are closely related and the elliptical galaxies lie on the empirically found fundamental plane (FP). The physical explanation for this relation is that these elliptical galaxies are self-gravitating systems with roughly constant mass-to-light ratios.

If ULIRGs indeed evolve into elliptical galaxies, they should also show the characteristic scaling relations of elliptical galaxies and lie on the fundamental plane, or they should lie close with plausible evolution towards the FP. However, the location of a galaxy with respect to the FP depends on its mass to light ratio (M/L), and an important evolving young stellar population will have a different M/L than a quiescent elliptical galaxy.

1.3 This thesis

The aim of this work is to study starbursts and the dynamical processes involved, both from gas and stellar components. For this purpose, we selected a galaxy with a nuclear starburst, M83, that is nearby ($D=4.5$ Mpc), in order to be able to study processes in detail. This is described in **Chapter 2**. We observed the central region of 330×330 pc, which includes the optical peak, and a starburst that is displaced from the nucleus, as well as several young star clusters. Star formation is traced by Br γ , the molecular gas by H $_2$ ($2.12 \mu\text{m}$), and [FeII] emission features indicate shocks from supernova remnants, which are spread over the whole observed region, all stages of (massive) star formation can thus be localised. The stellar population code Starburst99 is used to determine ages of the young star clusters. All this plus the gas and stellar velocity fields contribute to our understanding of this galaxy, but also show that these regions can have complex structures while starburst triggering mechanisms are not always easily understood.

The next goal was to place this in a wider context and we observed a sample of 6 ULIRGs to test if we can find signs of ULIRG evolution as described above. In **Chapter 3** we first describe the nearby (the nearest, $z=0.018$ or $D=78$ Mpc) cool ULIRG Arp 220. In this ULIRG-merger both nuclei of the progenitor galaxies are still recognisable and the spatial resolution is relatively high, compared to more distant ULIRGs. Various studies have investigated the origin of the infrared luminosity, provisionally indicating that the starburst is the (major) power source. We show that the two nuclei can still be recognised as dynamically independent entities, while most of the gas is already rotating in a single disk. We derive dynamical masses both from stellar dynamics and from gas dynamics and derive the near-IR mass-to-light ratio, which is used to roughly constrain the age of the starburst.

The other 5 ULIRGs of the sample, though local, are more distant with redshifts ~ 0.04 - 0.12 . They were selected to have a range in infrared colours (thus presumably stages of merging or evolution). All are classified as merger end-products with only one peak observed in

the (near-)infrared. However, we keep in mind what the nuclear region of a ULIRG can look like when observed with higher spatial resolution, as in the case of Arp 220. In Chapters 4 and 5, the rest of the ULIRG sample is described.

In **Chapter 4**, we focus on the stellar kinematics of the ULIRGs in the sample. Dynamical masses are calculated according to a model that approximates these objects as spherical bodies, a method that has been used in several studies before. The near-infrared (*K*-band) mass-to-light ratios are determined and are used to constrain the age of the starburst, as in the case of Arp 220.

In **Chapter 5**, we used the velocity fields of Pa α and/or H₂ for determination of the gas rotation curves. These curves were modelled with a spheroid (bulge) and a disk component. We used this model to derive the dynamical mass from gas kinematics, and compared these (and the mass-to-light ratios) to those from stellar dynamics. We argue which mass determination is the most reliable and finally, we placed the ULIRGs in (a projection of) the fundamental plane to find their location with respect to the elliptical galaxies that they are supposed to evolve into.

All observations were done with SINFONI, the Spectrograph for integral field observations in the Near-Infrared which is mounted on UT4 of the VLT on mount Paranal, Chile. All ULIRGs were observed with use of the laser guide star (LGS) facility for adaptive optics (AO), in order to achieve the best possible spatial resolution.

1.4 Conclusions and outlook

M83 From the analysis of the nuclear region of M83, we conclude that there is a separation between a compact and a diffuse component with large percentages in the diffuse emission in most lines. From our data in the central 330x330 pc, the diffuse component of [FeII] is 74%, the diffuse component of Br γ is 30% and the diffuse component of H₂ is 75%. The optical peak does not correspond to the dynamical centre. The gas dynamics show a rotating ring of gas, while the stellar dynamics show a different rotation pattern of regular rotation.

ULIRGs For the sample of 6 ULIRGs we compared the gas and stellar dynamics. The derived velocity fields are of excellent quality, and with the integral field spectroscopy it is possible to define the kinematic major axis with great confidence, which is which is a big improvement compared to older slit data studies. Even when our results are comparable to these literature data, these data give better accuracy. We conclude from our ULIRG analysis that

- the stellar dynamics is generally the better tracer of the mass than the gas dynamics, because the gas can still have disturbed morphology from the merger event. However, if the gas shows regular rotation and if an independent measurement of the gas mass is available (e.g. from mm CO observations), the gas kinematics can be used to derive the total mass which then agrees with the mass from stellar dynamics with high accuracy.

- there is no clear connection between the infrared colour (f_{25}/f_{60}) and K -band mass-to-light ratio (M/L_K); we explain this by concluding that we are observing the age of the most recent starburst instead of age of the system.
- the ULIRGs are offset from the fundamental plane by M/L_K , and passive evolution (the increase of M/L) will put the ULIRGs on the FP on the location of intermediate mass ellipticals, and not giants.

Outlook This study is far from completed. For most targets, our data provide a wealth of information, which has not been used fully. Several spectral lines in the ULIRG spectra, e.g. from H_2 , are left out of this study but could contain interesting information about the circumstances in these objects. More effort should be put in investigating the proposed sequence from cool to warm ULIRGs, which has still not been proved. The power of integral field spectroscopy (with adaptive optics) is essential for this purpose. The next thing that would be interesting to study in this sense is the ratio of gas mass to stellar mass, $M_{\text{gas}}/M_{\text{stars}}$. While the gas mass and stellar mass *an sich* highly depend on the properties of the merger progenitors, $M_{\text{gas}}/M_{\text{stars}}$ should decrease in an evolutionary sequence because the gas is consumed and the stellar mass is being built up. It would be worthwhile to work this out for a sufficiently large sample in the near future.

References

- Downes, D. & Solomon, P. M. 1998, ApJ, 507, 615
Elmegreen, B. 1994, in Violent Star Formation from 30 Dor to QSOs, ed. T. G.
Ferrarese, L. & Merritt, D. 2000, ApJ, 539, L9
Gebhardt, K., Bender, R., Bower, G., et al. 2000, ApJ, 539, L13
Genzel, R., Tacconi, L. J., Rigopoulou, D., Lutz, D., & Tecza, M. 2001, ApJ, 563, 527
Magorrian, J., Tremaine, S., Richstone, D., et al. 1998, AJ, 115, 2285
Sanders, D. B., Soifer, B. T., Elias, J. H., et al. 1988, ApJ, 325, 74
Tacconi, L. J., Genzel, R., Lutz, D., et al. 2002, ApJ, 580, 73
Toomre, A. 1964, ApJ, 139, 1217

The asymmetric nuclear region of M83 and its off-centre starburst



L. Vermaas and P. P. van der Werf
submitted to Astronomy & Astrophysics, 2011

Abstract

M83 is a nearby ($D=4.5$ Mpc) barred spiral hosting a nuclear starburst. Our near infrared integral field spectroscopic data show the complexity of the inner 330×330 pc. The nuclear region reveals a pronounced asymmetry, with the optical peak displaced eastwards from the centre of fainter isophotes, and the main starburst region displaced westwards. We find that $\text{Br } \gamma$ emission from young star clusters in the starburst region accounts for 70% of the total $\text{Br } \gamma$ emission (the rest of $\text{Br } \gamma$ emission being diffuse). Ages derived for the young star clusters show only a very small spread, suggesting a large-scale instability triggering this episode of star formation approximately simultaneously over 250 pc. In contrast to the $\text{Br } \gamma$ emission, the $[\text{FeII}]$ emission, tracing shocks from supernova remnants, is distributed in a large number of small and compact clumps and we show that these each correspond to one or at most a few supernova remnants. In contrast to $\text{Br } \gamma$, $[\text{FeII}]$ is dominated by diffuse emission (74% of the total $[\text{FeII}]$ emission), and we show that this diffuse emission also results from strong shocks. H_2 emission is found associated both with SNRs (where H_2 line ratios are found to be thermal) and with star forming regions (where H_2 line ratios indicate UV-pumped fluorescence), but like $[\text{FeII}]$, 75% of the total H_2 emission is diffuse in nature. Integrated over the central 330×330 pc, at most 10% of the $\text{H}_2 \nu = 1-0 \text{ S}(1)$ emission appears to be UV-excited.

We also study the velocity and velocity dispersion fields of both the stars and the gas. The stellar velocity dispersion shows no well defined peak and we rule out the presence of a large obscured mass concentration close to the centre of the faint isophotes, which had been suggested previously. The gas velocity field shows part of the molecular ring observed earlier using millimetre interferometry. Our data reveals a sharp inner edge to this ring, where a transition to a velocity field with a different kinematic major axis is seen; this transition may result from the presence of different orbital families in the barred potential. The gas velocity field also shows localised rotation centred on the optical peak, and we use this feature to determine a lower limit to the mass of the optical peak of $2.6 \cdot 10^7 M_{\odot}$. Our data furthermore show that the optical peak, while not currently forming stars, has undergone a recent episode of star formation, as shown by the presence of luminous supernova remnants. We discuss the implications of our results for our understanding of the remarkably asymmetric nuclear region of M83.

2.1 Introduction

The barred spiral galaxy M83 is one of the closest galaxies hosting a nuclear starburst. It is almost face-on ($i=24^\circ$ Comte 1981), and at a distance of 4.5 Mpc (Thim et al. 2003) it allows excellent spatial resolution ($1''=22$ pc) over the active region. The nuclear region has been studied in detail for many years, but disagreement still exists on the location of the dynamical centre of M83. Cowan et al. (1994) showed that the optical/NIR peak does not coincide with the radio emission peak. A $J - K$ colour image by Elmegreen et al. (1998) revealed two non-concentric rings of enhanced extinction in the nuclear region: an outer ring with a radius of $8.6''$ (190 pc), connecting to the two inner spiral arms and centred $2''$ south and $1.4''$ west of the optical peak, and an inner ring with a radius of $2.8''$ (62 pc) and centred on the the optical peak. An arc or partial ring of enhanced star formation (Gallais et al. 1991) is located in the region between these rings. Thatte et al. (2000) report that the centre of the K -band isophotes at radii more than $10''$ is offset from the optical peak, and located at approximately the same location as the centre of the outer ring found by Elmegreen et al. (1998). Furthermore, Thatte et al. suggest the existence of a second, obscured nucleus at this position, based on the fact that the stellar velocity dispersion as measured from long-slit spectroscopy of the $2.3 \mu\text{m}$ displays a second peak there. Finally, Sakamoto et al. (2004) used millimetre interferometry to study the velocity field of CO emission, and found the dynamical centre to be offset from the optical peak, at about the same location as Thatte’s “invisible nucleus”. Mast et al. (2006) combined optical Hubble Space Telescope data with ground-based integral field spectroscopy in the R -band and suggest the presence of a hidden mass concentration, more massive than the optical peak, at a different position: $4''$ northwest of the optical peak and $4''$ north from the dynamical nucleus of Sakamoto et al. (2004). Maddox et al. (2006) find several peaks in the radio regime, and confirm the offset of the brightest 20 cm radio peak from the optical peak.

In general, starbursts are associated with interacting or merging galaxies. M83 has a companion galaxy at a distance of 0.5 Mpc, NGC 5253, which hosts a nuclear starburst. However, no clear signature of interaction has been found in M83 itself. Furthermore, the last encounter with NGC 5253 was about 1 Gyr ago, which was too long ago to trigger the present starburst, which is much younger with an estimated age of 6 Myr (Houghton & Thatte 2008). It has been proposed that the capture of a small object by the galaxy has led to formation of the bar and triggered the starburst (e.g., Sakamoto et al. 2004, Díaz et al. 2006). Recent observations of gas kinematics show the gas flow from outer regions to the centre, and indicate that an inner Lindblad resonance can be responsible for the accumulation of gas in the nuclear region, resulting in a starburst (e.g., Fathi et al. 2008). Sakamoto et al. (2004) speculated that the optical peak, which is older than the other nuclear star clusters, could be the remnant of a captured dwarf galaxy. Both Harris et al. (2001) and Houghton & Thatte (2008) studied the ages of the star clusters in the nuclear region and found a clear age gradient, with the youngest clusters in a region west of the optical peak, with older clusters in an arc-like structure extending from this position towards the southeast. Recently, Knapen et al. (2010) confirmed these results and suggested that the offset of the optical peak from the photometric and kinematic centre is the result of an $m = 1$ perturbation in the nuclear gravitational potential.

Table 2.1 – Parameters of VLT/SINFONI observations

Night	band	pointings	$N_{\text{frames}}, t_{\text{int}}$
2 & 3 April 2005	<i>J, H, K</i>	3 pointings (ABC)	2x300 s/pointing
23 April 2005	<i>H</i>	2 pointings (AB)	2x300 s/pointing
Pointings (field centres)	A (northwest)	B (southwest)	C (optical peak)
RA (J2000)	13:37:00.2	13:37:00.3	13:37:00.8
DEC (J2000)	−29:51:51.6	−29:51:58.6	−29:51:56.6
SINFONI 0''25 platescale	<i>J</i>	<i>H</i>	<i>K</i>
FOV	8'' × 8''	8'' × 8''	8'' × 8''
spatial pixelscale	0''125 × 0''250	0''125 × 0''250	0''125 × 0''250
wavelength range	1.10 - 1.40 μm	1.45 - 1.85 μm	1.95 - 2.45 μm
spectral resolution $\lambda/\Delta\lambda$	2000	3000	4000

In this paper we present new near-infrared (near-IR) integral field observations of the nuclear region (inner 330×330 pc) of M83. We carry out an analysis of the starburst and its products (star formation rate, cluster ages and masses, supernova rate), and place this in the context of the nuclear dynamics, considering both gas and stars. We specifically investigate the reality of the putative “dark nucleus” using the distribution of stellar velocity dispersions in the nuclear region, and the role of the rotating gas ring detected using millimetre interferometry.

2.2 Observations and data reduction

2.2.1 SINFONI observations

We observed M83 with SINFONI, the Spectrograph for INtegral Field Observations in the Near-Infrared (1.1 - 2.45 μm), which is installed on UT4 (Yepun) of the ESO Very Large Telescope (Eisenhauer et al. 2003, Bonnet et al. 2004). Our observations were carried out in all three atmospheric windows available: the *J, H* and *K* bands. The largest platescale was used, with a field of view of $8'' \times 8''$ on 64×64 spatial pixels. The spectrum from each pixel is divided over ~ 2000 spectral elements (depending on the band), with spectral resolutions $\lambda/\Delta\lambda$ of 2000, 3000 and 4000 in *J, H* and *K*, respectively.

Three overlapping pointings were chosen in the nuclear region. One field was centred on the optical peak, and two pointings west of the nucleus include starburst and continuum peaks that were known from previous observations. Observations in the *J, H* and *K* bands were carried out on April 2 and 3 of 2005. Additional *H*-band observations (without the pointing on the optical peak) were taken on April 23 of 2005. The total integration time for

each pointing was 600 s, split into two observations of 300 s each. Sky frames of the same integration time were taken with each filter for each pair of observations. The *K*-band seeing during these observations was approximately $0.6''$. Further details are given in Table 2.1.

2.2.2 SINFONI data reduction

The data were reduced with the standard SINFONI pipeline, which was developed by ESO and the Max-Planck-Institut für extraterrestrische Physik. The default procedure included corrections for pixel non-linearity, distortion and wavelength calibration. Flux calibration as well as telluric feature correction was done with observations of a standard star. Each frame was also corrected for spatially variable transmission by applying an illumination correction.

The observations were done in ABA²-nodding mode, i.e. object-sky-object, with the A' frame slightly shifted with respect to the A frame. All observations were carried out with the same setup and the same integration time of 300 s. Thus, for each object frame there is a sky frame observation with the same integration time. However, variability of the sky even on these timescales caused problems, especially in the H-band, which is densest in OH lines. For this reason, in some cases the sky frames were corrected with a multiplication factor of typically a few percent, or a spectral shift up to 0.1 pixel.

A standard star was observed right after each object-sky-object observation at the same airmass. This was typically a B star containing few stellar lines in the NIR. Stars with known *J*, *H* and *K* magnitudes were selected from the Hipparcos catalogue, and were used for telluric feature removal as well as for flux calibration. The standard stars were reduced with the same setup as was used for the science frames. After reduction, the average stellar spectrum was extracted from each standard star frame, and stellar lines were removed (recombination lines, especially the Brackett-series in *H*-band). The one dimensional spectrum was divided by a blackbody of the same temperature to get a flat spectrum with atmospheric absorption features only. The number of counts was converted to flux using the literature values of the star's magnitude in that band. The spectrum in each pixel of the image was divided by this cleaned standard star spectrum. Telluric absorption features were removed satisfactorily. Flux calibration, however, appeared to be slightly variable between the frames and the observations were calibrated with *JHK* imaging data obtained with IRAC2 on the ESO/MPG 2.2 m telescope under photometric conditions (see Section 2.2.3).

Finally, for each band, all six datacubes, cleaned, calibrated and illumination corrected, were coadded with the correct shifts to obtain the final mosaic datacube. In every pixel of the SINFONI field of view, ionised and molecular gas spectral emission lines were fitted with single Gaussians. This procedure resulted in images of integrated line flux, velocity and velocity dispersion for the brightest emission lines detected in M83.

2.2.3 IRAC2 data

We established the absolute flux scale of the SINFONI data by comparing to unpublished *JHK* imaging obtained earlier with IRAC2 (Moorwood et al. 1992) at the ESO/MPG 2.2 m telescope at La Silla, Chile. The camera used a 256×256 HgCdTe array and the $0.27''/\text{pixel}$

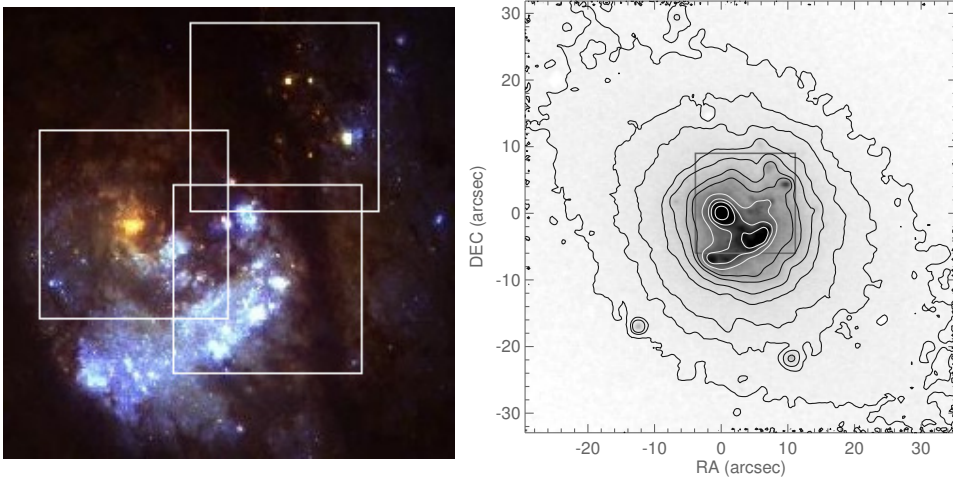


Figure 2.1 – Left: archival HST/WFPC2 image, composite blue (F300W), green (F547M) and red (F814W) filters. The white squares indicate the pointings of the SINFONI observations. Right: IRAC2 K -band image with contour overlay (black: $[5.0, 7.5, 10, 15, 20, 30, 40] \cdot 10^{-3} \text{ erg s}^{-1} \text{ cm}^{-2} \mu\text{m}^{-1} \text{sr}^{-1}$; white: $[60, 80, 100, 150] \cdot 10^{-3} \text{ erg s}^{-1} \text{ cm}^{-2} \mu\text{m}^{-1} \text{sr}^{-1}$); the grey square denotes the outer edges of the combined SINFONI image (as shown in Fig. 2.2).

image scale was employed under photometric conditions on June 17, 1993. Total integration time was 160 s, for K -band, 240 s for H -band and 320 s for J -band, with an equal amount of sky. Photometric calibration was achieved by observations of the F5V star HD 122414 with magnitudes $J = 8.536$, $H = 8.281$ and $K = 8.224$ (Carter & Meadows 1995) at a closely similar airmass. Standard procedures for sky subtraction, flatfielding and interpolation of bad pixels were used. Finally, the frames were aligned and averaged.

2.2.4 VLA data

In our analysis we will also use the radio emission from supernova remnants in M83. Unfortunately, high-quality radio continuum imaging of this region at a resolution comparable to our near-IR data is not available in the literature. We therefore used our own radio continuum imaging obtained earlier with the NRAO Very Large Array. In order to achieve a resolution similar to our near-IR data, we used the hybrid BC configuration (resulting in an approximately circular beam at the Declination of M83) at a frequency of 14.96 GHz. At this frequency, a combination of both thermal bremsstrahlung from HII regions and synchrotron radiation from supernova remnants is expected. The observations used the U-band receiver with a bandwidth of 100 MHz and 2 polarisations in 27 antennas. Total integration time was 5.3 hours, and phase calibration was carried out every 15 minutes. Flux calibration was established using observations of the radio source 3C 286 (assumed flux 538 mJy) before and after the M83 observations. Standard AIPS procedures were used for flagging bad data, amplitude and phase calibration, map making and cleaning. The resulting image has a full width at half

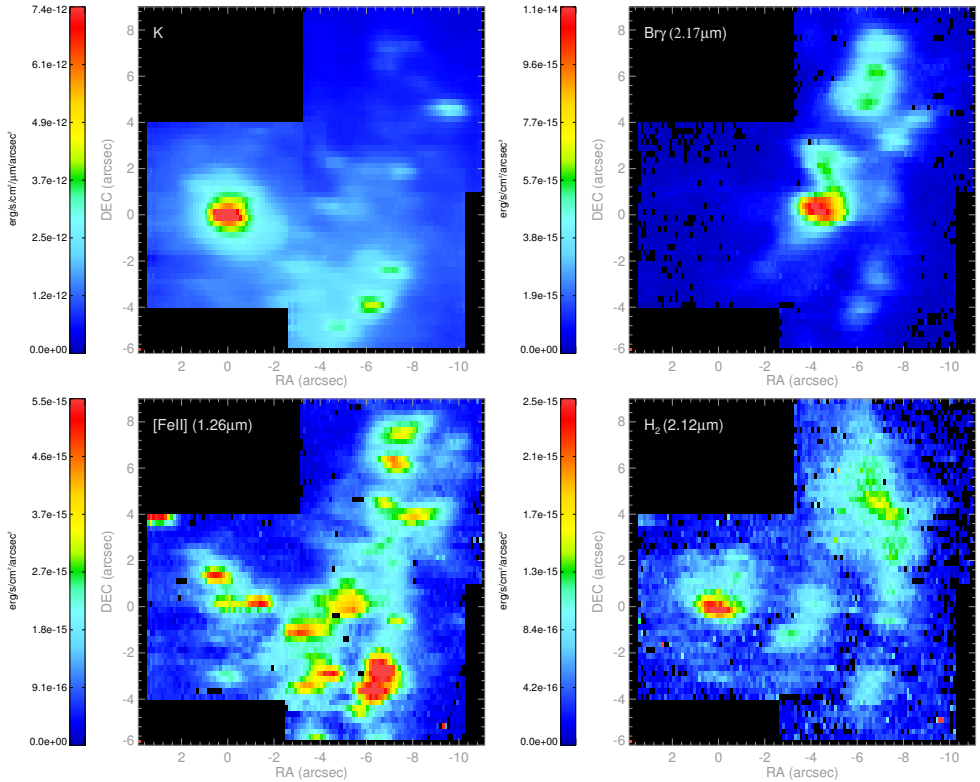


Figure 2.2 – Upper left: K band continuum; upper right: line image of $\text{Br}\gamma$ ($2.17\mu\text{m}$); lower left: line image of $[\text{FeII}]$ ($1.257\mu\text{m}$); lower right: line image of H_2 ($2.12\mu\text{m}$). Position (0,0) is in all cases at the peak of the K -band continuum.

maximum (FWHM) synthesised beam of $1.23'' \times 1.05''$, at a position angle of 62.2° , and an r.m.s. noise at the field centre of $58\mu\text{Jy beam}^{-1}$.

2.3 Results

Our extensive dataset contains a wealth of information on spectral lines (tracing various gas components) as well as stellar emission and absorption features. In order to present these features clearly, we begin with an overview of the region. We then discuss the stellar continuum, followed by the various spectral lines. We then define regions of spectral interest, discussing their integrated spectral properties.

2.3.1 Morphology of the nuclear region of M83

The left frame of Figure 2.1 shows a true-colour image of the nuclear region of M83 in the optical from HST/WFPC2 archival data (2002). The orange peak is the brightest optical/near-

IR feature, and is henceforth referred to as the “optical peak”. Its orange colour shows that it is older than the young star clusters in the region that show up in blue/white. The white contours indicate the borders of the SINFONI observations. The composed mosaic image ($15'' \times 15''$, as in Fig. 2.2) corresponds to 330×330 parsec.

2.3.2 Near-IR continuum

The K -band continuum (Fig. 2.2, upper left) is dominated by a strong peak. This peak is resolved with a FWHM of $1''.12$ (24 pc). The peak coincides with the brightest optical peak, the orange peak in the HST/WFPC2 composite image, Fig. 2.1 (left). Most of the young blue star clusters seen in the left frame of Fig. 2.1 have counterparts in the near-IR, such as the three peaks lining up in the lower right frame, and the peak in the upper right frame of the SINFONI K -band image.

As a reference, the IRAC2 image in Fig. 2.1 (right) shows the K -band out to a larger scale. Also here the luminous peak is recognised, but it can be seen that it is offset from the centre of the fainter isophotes, as was established already by Thatte et al. (2000). We therefore do not refer to the optical peak as “nucleus”, in order to avoid confusion with the isophotal centre or the dynamical centre.

2.3.3 Br γ emission

Br γ (HI 7-4, $2.166 \mu\text{m}$, Fig. 2.2, upper right) is, together with Pa β (HI 5-3, $1.281 \mu\text{m}$), one of the strongest of the hydrogen and helium recombination lines that are visible in the near-IR. These lines originate in HII regions around the hot, young stars that ionise their surrounding interstellar medium and therefore trace recent massive star formation. The line emission peaks in a well defined region that is located $4''$ (~ 90 pc) westward of the optical peak. Although diffuse Br γ emission is detected over the whole observed field, no feature is in particular associated with the optical peak. A second, fainter peak is found in the northwest frame of the mosaic image. Most Br γ features have counterparts in the K -band continuum image, but these are relatively faint.

2.3.4 [FeII] emission

The most prominent iron features are the forbidden emission lines of [FeII] in the J -band at $1.257 \mu\text{m}$ and in the H -band at $1.644 \mu\text{m}$. The distribution of $[\text{FeII}]_{1.26\mu\text{m}}$ is shown in the lower left frame of Fig. 2.2. The line is emitted in peaks that are distributed over the whole field of view. Three of the peaks are associated with the optical peak, while others partly overlap with local peaks of the K -band continuum (southwest) and Br γ (northwest). As will be discussed in Section 2.4.4, these lines trace fast shocks associated with supernova remnants (SNRs), and each [FeII]-peak presumably represents several supernovae. In this scenario the strong shocks associated with the SN-explosion destroy the grains, thereby liberating the iron-atoms that were originally locked up in grains. The iron atoms are then singly ionised, producing the [FeII] lines.

2.3.5 H₂ emission

Warm molecular hydrogen gas is detectable in the near-IR through molecular rotation-vibration lines, of which most are found in the *K*-band. The strongest is the H₂ 1-0 S(1) transition line at 2.12 μm, see the lower right frame of Fig. 2.2. The line is mostly concentrated around the optical peak. An arc-shaped structure overlaps with the second peak of Br γ emission, about 6'' from the optical peak. Some of the excited H₂ (2.12 μm)-emission is associated with peaks of [FeII], such as the fainter double peak in the centre of the field and in the lower right, which also lines up with the three peaks in continuum emission. The arc-shape of H₂ (2.12 μm) in the western half of the field can be recognised in the fainter Br γ-emission as well.

2.3.6 Spectra

Regions of special interest were selected for which spectra were combined. The lines of these spectra were fitted manually with the IDL-based package ISAP. The regions, as indicated by the contours in Fig. 2.3, were defined for pixel values above some threshold of *K*-band continuum (A; white), Br γ (B; red) and [FeII]_{1.26 μm} (C; green). The *J*, *H* and *K* spectra of regions A1, B1 and C2 are shown in Figs. 2.4 and 2.5.

Region A1: continuum peak

The top three spectra (top to bottom: *J-H-K*) in Fig. 2.5 are from region A1, the optical peak region where the near-IR continuum is strong. Several absorption features that arise in the cooler atmospheres of giants/supergiants are detected in *H* and *K*. The most prominent features in our data are the deep ¹²CO 0-2 at 2.29 μm (first overtone), ¹³CO 1-3 at 2.32 μm and ¹³CO 0-2 at 2.34 μm in the *K*-band, and ¹²CO 3-6 at 1.62 μm in *H*, but also a large number of less prominent absorption features are recognisable, e.g., Si I (1.59 μm), Mg I (1.71 μm), Na I (2.21 μm) and Ca I (2.26 μm). Some of the strong absorption features in the *H*-band (1.57 μm, 1.58 μm, 1.66 μm), however, are of telluric origin and result from a combination of high airmass and a discrepancy in airmass between the standard star and the observations of this particular frame, leading to imperfect correction in the data.

As expected, the H₂ (2.12 μm) line is visible, as well as [FeII] (1.257 μm) although the [FeII] (1.644 μm) hardly stands out because of lower data quality. Also Br γ (2.17 μm) and Pa β (1.28 μm) are clearly recognisable despite the fact that this is only “diffuse” extended emission, not directly associated with the optical peak (see Fig. 2.2).

Region B1: Br γ peak

The three top spectra in Fig. 2.4 are from the strongest Br γ peak, and show the typical spectral lines of bright HII regions. Br γ (2.17 μm) and Pa β (1.28 μm) are very strong, and the Brackett series (Br10-Br19 and further) especially stands out in the *H*-band. Helium recombination lines are visible in all of the *J* (1.28 μm), *H* (1.70 μm) and *K* (2.06 μm) bands. In addition to the HII region lines, lines of OI and [PII] are found in *J*. The OI 1.317 μm line is a fluorescent line excited by UV radiation in the neutral gas very close to ionisation fronts

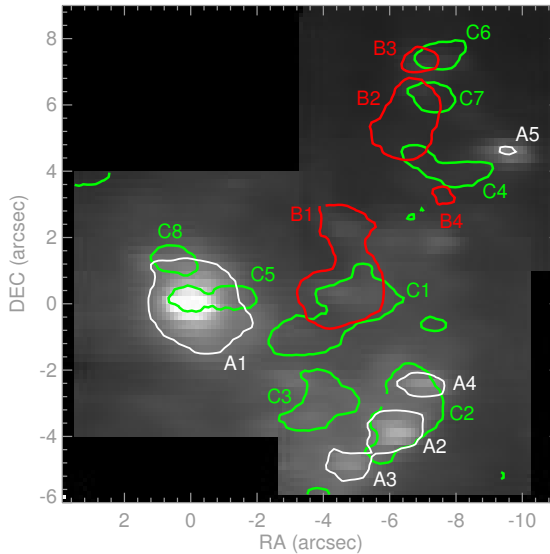


Figure 2.3 – Regions defined by specific thresholds. White (A1-A5): K -continuum $> 2.5 \cdot 10^{-12} \text{erg s}^{-1} \text{cm}^{-2} \mu\text{m}^{-1} \text{arcsec}^{-2}$; red (B1-B4): $\text{Br}\gamma$ ($2.17 \mu\text{m}$) $> 3.8 \cdot 10^{-15} \text{erg s}^{-1} \text{cm}^{-2} \text{arcsec}^{-2}$; green (C1-C8): $[\text{FeII}]$ ($1.257 \mu\text{m}$) $> 2.6 \cdot 10^{-15} \text{erg s}^{-1} \text{cm}^{-2} \text{arcsec}^{-2}$. Line fluxes of different regions are given in Table 2.2, spectra of regions A1, B1, B2 and C2 are in Figs. 2.4 and 2.5. The underlying grayscale shows the K -band continuum.

(Walmsley et al. 2000). The $[\text{P}II]$ line at $1.188 \mu\text{m}$ traces partially ionised regions irradiated by X-rays from an Active Galactic Nucleus (AGN) or, in the present case, in the hot UV-illuminated layers of Photon-Dominated Regions (PDRs), as argued by Oliva et al. (2001). The $\text{Br}\gamma$ region overlaps with a region of $[\text{FeII}]$ (C1) which also shows H_2 emission, and many stronger and weaker emission lines of both are visible in all bands ($[\text{FeII}]$ in J and H , H_2 mainly in K). The continuum is about 3 times lower than on the optical peak, but most of the absorption features are visible.

Region C2: $[\text{FeII}]$ peak

The three spectra at the bottom of Fig. 2.5 are from a region that has strong $[\text{FeII}]$ emission, that peaks between two continuum peaks and is also slightly enhanced in $\text{Br}\gamma$. $[\text{FeII}]$ especially stands out in the H -band spectrum ($1.64 \mu\text{m}$), where the Brackett lines are totally absent, although $\text{Br}\gamma$ and $\text{Pa}\beta$ are moderately strong and even HeI is present at $2.06 \mu\text{m}$. Weaker lines of $[\text{FeII}]$ are not as abundant as may be expected, and may be masked by photospheric features in the strong continuum. The CO absorption bands in K are strong, and also many absorption features are visible in H . It is noteworthy that the $[\text{P}II]$ line at $1.188 \mu\text{m}$, which has very similar excitation requirements to the $[\text{FeII}]$ lines, is totally absent. As argued by Oliva et al. (2001), this indicates a strongly enhanced abundance of gas-phase iron, and is direct evidence of grain destruction in fast shocks.

Region B2: second Br γ (and H₂) peak

The bottom three spectra in Fig. 2.4 are from region B2, the second brightest Br γ peak which also coincides with the concentration of H₂ on the arc-like structure (see Fig. 2.2, lower right). The continuum in this region is faint, and the CO-absorption bands in *K* are shallow, but present. All the Brackett lines and important [FeII] lines are detected, as well as OI and [PII], and in this case also many H₂ lines show up over the whole wavelength range. Besides the first order rotation-vibrational lines of $J = 1-0$ and $2-1$, such as H₂ 1-0 S(1) at 2.12 μm , several higher order lines of the 3-1 and 2-0 bands are detected (see Table 2.6).

2.4 Analysis

In this section we will relate the starburst tracers in M83 to underlying physical processes and quantify these in order to understand the temporal and spatial evolution of this circumnuclear starburst. Extinctions are calculated from two different line ratios, star formation properties are derived from recombination lines and cluster ages are modelled with Starburst99 (Leitherer et al. 1999, Vázquez & Leitherer 2005). [FeII] is used as a tracer of supernova activity. Pinning down the origin of the H₂ emission is not trivial, but is enabled by the detection of many lines from many different levels. The morphology of the emission from different species is compared both with the VLA-2cm radio map and mid-infrared PAH emission. The continuum, linestrengths and extinction estimates for the regions as defined in Fig. 2.3, as well as for two background regions, are listed in Table 2.2.

2.4.1 Extinction

Foreground extinction can be calculated using line pairs that have (almost) fixed intrinsic ratios by comparing the observed ratio to the theoretical line ratios, and several lines are available for this purpose. The [FeII] lines in the *J* and *H* bands (at 1.257 and 1.644 μm , respectively), originate from the same upper level with an intrinsic ratio of 1.36 (Nussbaumer & Storey 1988). Also Pa β (5-3), Br γ (7-4) and the Brackett-series in the *H*-band (from upper levels 9-22 to 4, have almost fixed intrinsic ratios, adopted here from Hummer & Storey (1987) for a temperature of 10^4 K. The extinction can be calculated from the observed line ratios, using the assumption that the dust is located in an absorbing foreground screen and an the extinction law at near-IR wavelengths of the form $A_\lambda \propto \lambda^{-1.8}$ (Martin & Whittet 1990). Figure 2.6 shows the distribution of visual extinction (A_V), derived from from the Pa β /Br γ and the [FeII]_{1.26 μm }/[FeII]_{1.64 μm }/ ratios. These distributions are similar in their broad features with values ranging from $A_V=1$ in low-extinction regions, to 10 and higher in high-extinction peaks. The Pa β /Br γ extinction distribution agrees well with that derived from H α and Pa β by Houghton & Thatte (2008). A dust lane can be identified in the northwest, roughly from (-4,8) to (-9,0), and is clearest in the Pa β /Br γ extinction image. Nevertheless, some remarkable differences exist between the Pa β /Br γ and [FeII] derived extinction distributions, indicating that the young star formation regions traced in Pa β and Br γ are not located in the same dust complexes as the supernova remnants responsible for the [FeII] emission. Generally, peaks of}}

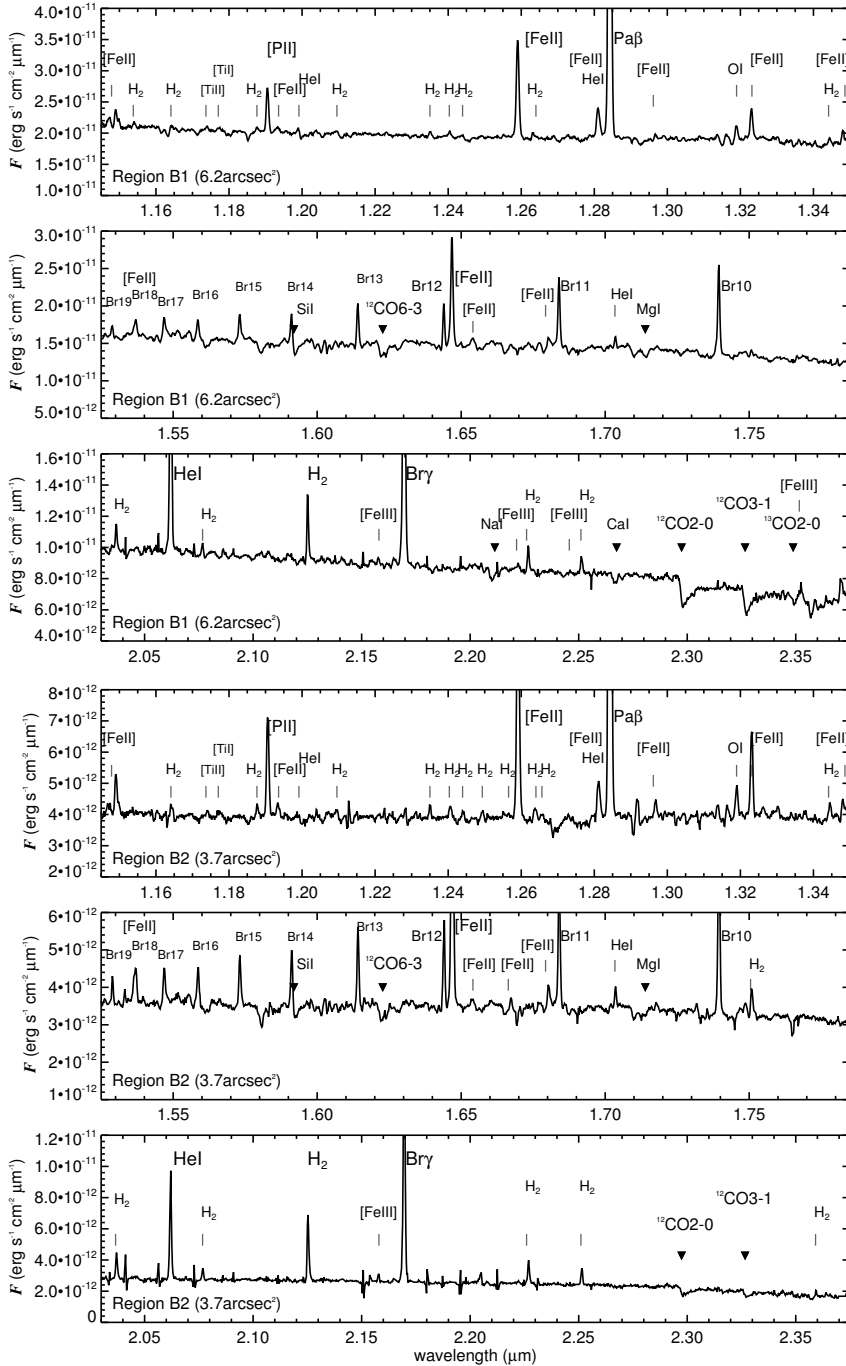


Figure 2.4 – Integrated spectra of Br γ -defined starburst regions B1 (top 3) and B2 (bottom 3) as indicated in Fig. 2.3. Some emission lines are marked with vertical lines, stellar absorption features are marked with filled triangles.

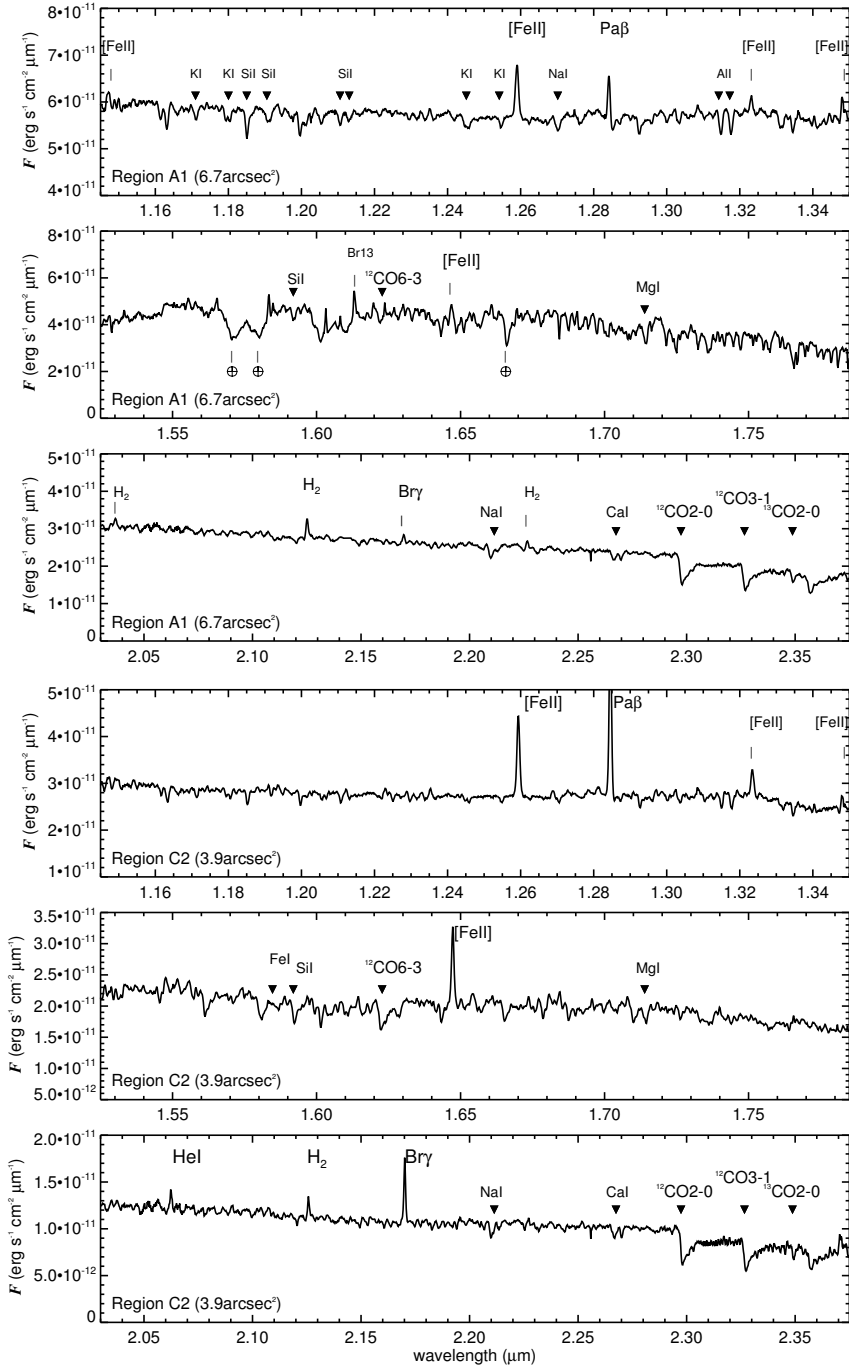


Figure 2.5 – Integrated spectra of regions A1 (top 3, K-band continuum-defined), and C2 (bottom 3, [FeII] $_{1.26\mu\text{m}}$ -defined) as indicated in Fig. 2.3. Some emission lines are marked with vertical lines, stellar absorption features are marked with filled triangles, and the earth symbols in the H-band spectrum of region A1 indicate telluric absorption features that could not be removed.

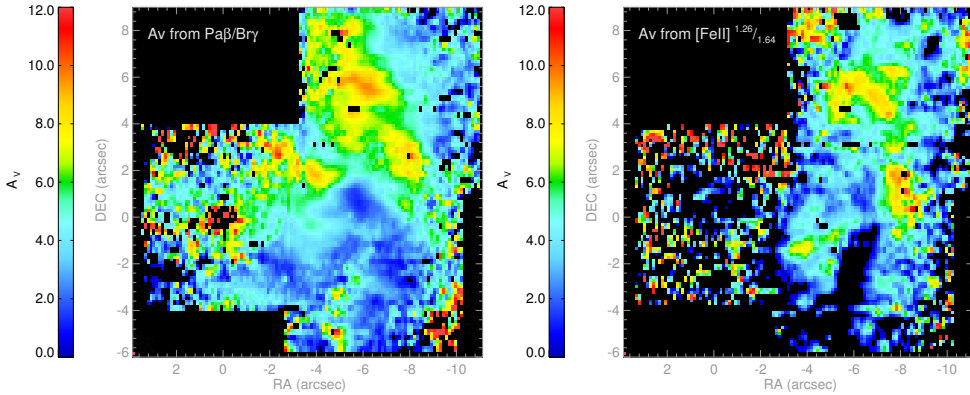


Figure 2.6 – Left: extinction map (A_V) from line ratio $\text{Pa}\beta/\text{Br}\gamma$; right: extinction map A_V from line ratio $[\text{FeII}]_{1.26\mu\text{m}}/[\text{FeII}]_{1.64\mu\text{m}}$. Note that the poor data quality in H-band in the eastern frame precludes reliable extinction determination from the iron lines in that region. The high extinction on the optical peak (0,0) in the lefthand panel is an artifact resulting from imperfect atmospheric absorption correction in this region.

extinction derived from the $\text{Pa}\beta/\text{Br}\gamma$ correspond to local peaks in the $\text{Pa}\beta$ and $\text{Br}\gamma$ emission, but the most prominent $\text{Br}\gamma$ peak is remarkably extinction-free. In contrast, peaks in the $[\text{FeII}]$ derived extinction cannot be readily identified with local peaks in the $[\text{FeII}]$ emission. These results suggest that the $\text{Pa}\beta/\text{Br}\gamma$ -derived extinction is more sensitive to dust directly associated with young regions of star formation, while the $[\text{FeII}]$ lines trace the more general dust distribution in the starburst region.

2.4.2 Star forming regions

We here refer only to the regions with high $\text{Br}\gamma$ -flux (Fig. 2.3) as (high-mass) star forming regions, although star formation tracers are widespread in the whole field. Extinction-corrected line fluxes and derived properties are in Table 2.3, for the $\text{Br}\gamma$ -defined regions as well as for the K -band continuum defined regions.

Ionising radiation field and massive stellar content

The ionisation rate in HII regions is expressed by $Q_{\text{Ly}\alpha}$, the number of photons per second that can ionise hydrogen (Lyman continuum), i.e. photons with energies >13.6 eV. $Q_{\text{Ly}\alpha}$ can be estimated from recombination line fluxes, e.g., it relates to $\text{Br}\gamma$ ($2.17\mu\text{m}$):

$$Q_{\text{Ly}\alpha} = 1.0 \cdot 10^{51} \left(\frac{F_{\text{Br}\gamma}}{10^{-13} \text{ erg s}^{-1} \text{ cm}^{-2}} \right) \left(\frac{D}{\text{Mpc}} \right)^2 \text{ s}^{-1} \quad (2.1)$$

where D is the distance and $F_{\text{Br}\gamma}$ is the $\text{Br}\gamma$ flux.

Obviously, stars of a range of spectral types contribute to the ionisation of a single cluster, but it is convenient to follow the approach of Vacca (1994) and translate $Q_{\text{Ly}\alpha}$ into the equiv-

Table 2.2 – Integrated continuum and line fluxes and average extinctions of the regions as indicated in Fig. 2.3. The regions with boldface in column (1) have their spectra presented in Figs. 2.4 and 2.5.

Region ^d	Size ^a (pix)	S_K (10^{-13}) ($\text{erg s}^{-1} \text{cm}^{-2} \mu\text{m}^{-1}$)	$F_{\text{Br}\gamma}$	$F_{\text{Pa}\beta}$	$F_{\text{H}\alpha}(1.70\mu\text{m})$	$F_{[\text{FeII}]1.26\mu\text{m}}$	$F_{[\text{FeII}]1.64\mu\text{m}}$	$F_{\text{H}_2}(2.12\mu\text{m})$	A_V	
			(4)	(5)	(6)	(7)	(8)	(9)		(10)
(1)	(2)	(3)	(4)	(5)	(6)	(7)	(8)	(9)	(10)	(11)
A1	408	252	30	70	-	128	83	10.4	7.5	-
A2	110	54	31	131	12	75	53	10.3	2.7	-
A3	56	25	4.2	13	-	8.3	-	2.6	5.2	-
A4	54	24	16	74	-	36	32	3.2	2.0	2.3
A5	10	4.3	2.0	10	-	2.1	1.7	0.5	1.3	1.2
B1	394	89	392	1340	13	146	140	37	4.5	3.3
B2	226	25	170	408	4.3	72	87	39	7.3	6.2
B3	42	6.5	29	100	0.7	17	19	4.8	4.4	5.3
B4	20	2.8	13	29	0.2	6.3	7.6	3.4	7.9	6.2
C1	300	76	250	954	7.7	156	160	32	3.5	4.2
C2	256	105	75	312	-	178	137	25	2.8	0.57
C3	156	54	25	102	-	85	71	8.4	3.0	1.6
C4	106	15	57	166	-	52	77	19	5.7	8.8
C5	92	78	8.6	22	-	49	62	22	6.8	6.8
C6	60	8.2	32	118	-	28	30	4.5	3.8	4.7
C7	52	6.4	37	108	1.24	29	36	6.9	5.7	6.6
C8	54	21	4.2	16	-	31	20	6.9	3.5	-
bg1 ^e	36	6.0	1.4	4.6	-	3.2	2.7	1.2	4.7	1.7
bg2 ^e	36	6.3	1.2	5.2	-	3.2	3.3	1.5	2.5	4.2

^a 1 pixel = $0''.125 \times 0''.125 = 2.725 \text{ pc} \times 2.725 \text{ pc} = 7.4 \text{ pc}^2$

^b Extinctions from line ratio $F_{\text{Pa}\beta}/F_{\text{Br}\gamma}$ (intrinsic ratio 5.88), and $A_\lambda \propto \lambda^{-1.8}$ (Martin & Whittet 1990).

^c Extinctions from line ratio $F_{[\text{FeII}]1.26\mu\text{m}}/F_{[\text{FeII}]1.64\mu\text{m}}$ (intrinsic ratio 1.36), and $A_\lambda \propto \lambda^{-1.8}$ (Martin & Whittet 1990).

^d The region numbers correspond to the regions as defined in figure 2.3.

^e Background measurements from regions of 6×6 pixels with no particular features in the NIR continuum, Br γ , [FeII] or H₂. Regions bg1 and bg2 are centred at (1,-3.5) and (-9,0), respectively.

Table 2.3 – Derived properties of star forming regions. Emission line fluxes and the quantities derived from them have been corrected for extinction using the Pa β /Br γ ratio.

(1)	(2)	(3)	(4)	(5)	(6)	(7)	(8)	(9)	(10)	(11)	(12)
Region	Size ^a (pix)	$F_{\text{Br}\gamma\text{ec}}$ ($\text{erg s}^{-1}\text{cm}^{-2}$) $\cdot 10^{-16}$	$L_{\text{Br}\gamma}$ (L_{\odot}) $\cdot 10^3$	$F_{\text{Pa}\beta\text{ec}}$ ($\text{erg s}^{-1}\text{cm}^{-2}$) $\cdot 10^{-16}$	$L_{\text{Pa}\beta}$ (L_{\odot}) $\cdot 10^3$	W(CO) (\AA)	Q^c (s^{-1}) $\cdot 10^{51}$	SFR ^d ($M_{\odot}\text{yr}^{-1}$)	N_{O7}^e	$\frac{F_{\text{HeI}(1.7\mu\text{m})}}{F_{\text{Br}\gamma 10}}$	T (model) (K) $\cdot 10^4$
B1	394	555	34.8	3260	205	1.7	11.2	1.1	2240	0.121	3.45
B2	226	300	18.8	1769	111	5.3	6.0	0.6	1200	0.102	3.4
B3	42	41	2.6	239	15.0	6.0	0.83	0.08	166	0.088	3.35
B4	20	24	1.5	142	8.9	12.1	0.49	0.05	98	0.093	3.3
A1	408	54	3.4	318	20.0	13.2	1.1	-	220	-	-
A2	110	38	2.4	225	14.1	14.7	0.77	0.15	154	-	-
A3	56	6.3	0.40	37	2.3	14.4	0.13	0.11	26	-	-
A4	54	19	1.2	110	6.9	11.3	0.38	0.08	76	-	-
A5	10	2.2	0.14	13	0.82	11.9	0.04	0.006	8	-	-
bg1 ^f	36	2.0	0.13	4.7	0.30	13.1	-	0.0004	8	-	-
bg2 ^f	36	1.5	0.09	2.5	0.16	10.2	-	0.0003	6	-	-

^a 1 pixel = $0''.125 \times 0''.125 = 2.725 \text{ pc} \times 2.725 \text{ pc} = 7.4 \text{ pc}^2$

^b Extinctions from line ratio $F_{\text{Pa}\beta 1.28\mu\text{m}}/F_{\text{Br}\gamma 2.17\mu\text{m}}$ (intrinsic ratio 5.88), and $A_{\lambda} \propto \lambda^{-1.8}$ (Martin & Whittet 1990).

^c Using equation (2.1).

^d Calculated by dividing stellar mass formed by age.

^e Taking $Q_{\text{O7V}} = 5 \cdot 10^{48} \text{ s}^{-1}$ from Martins et al. (2005).

^f Background measurements, see Table 2.2 for the definitions of bg1 and bg2.

alent number of O7V-stars for a specific ionised region. Based on Martins et al. 2005), we take $Q_{O7V}=5 \cdot 10^{48} \text{ s}^{-1}$. Calculated values of Q from $F_{Br\gamma}$ are in column (7) of Table 2.3. The largest and most luminous star formation regions contain a few 1000 (equivalent) O7V-stars (of $\sim 25 M_{\odot}$), in a region of a few 1000 pc^2 . The smaller regions (few 100 pc^2) contain a few hundred (equivalent) O7V-stars. Compared to local star forming regions, the large star forming regions are similar to the giant HII region 30 Doradus in the LMC, which contains $\sim 10^4 M_{\odot}$ in young stars in its central 10 pc core.

Temperature of the radiation field

Photons with energies above 24.6 eV can ionise helium, thus the ratio of He over H recombination lines will give a measure of the hardness of the ionisation field. Although bright, the HeI ($2.06 \mu\text{m}$) line is not suitable for this purpose, because the population of the 2^1P state (the upper level of the $2.06 \mu\text{m}$ line) is affected by radiative transfer effects and excitation from the 2^3S state (e.g., Shields 1993, Lancon & Rocca-Volmerange 1996, Lumsden et al. 2001, Rigby & Rieke 2004). Instead, we measured the ratio of HeI ($1.70 \mu\text{m}$) over Br 10 ($1.74 \mu\text{m}$), which lie close in wavelength and thus are only slightly affected by extinction. With the line ratio, it is possible to model the temperature of the ionisation field (Vanzi et al. 1996, Vanzi & Rieke 1997, Lumsden et al. 2003), which is approximately equivalent to the temperature of the hottest star in the region. This method is only unambiguous for T below $4 \cdot 10^4$ K, where the line ratio saturates (i.e., both the HeI and HI Strömgren spheres are maximally filled). Results for M83 are in Table 2.3, columns (11-12). The radiation field in the brightest Br γ -region (B1) has a temperature of $34.5 \cdot 10^3$ K, which matches an O7 star. The hottest star at the second Br γ -peak (B2) has only a slightly lower temperature of $34 \cdot 10^3$ K matching an O7.5 star. Since in a passively evolving young star cluster the temperature of the radiation field evolves as massive stars move off the main sequence, the HeI/Br10 ratio is also age-sensitive, and we will use this property together with other age indicators in the next section.

Cluster ages and masses

In general, the K -band continuum traces late-type giants/supergiants, the more evolved stellar population. The near-IR luminosity resulting from a single burst comes from red (evolved) stars: first from massive stars that evolved into supergiants (~ 10 Myr), followed by intermediate giants (AGB-stars, ≥ 100 Myr) and finally low mass giants near the tip of the RGB (few Gyr).

In order to determine the ages of the star clusters, we modelled the stellar populations with Starburst99, version 5.0 (Leitherer et al. 1999, Vázquez & Leitherer 2005). A Salpeter IMF ($\alpha=2.35$) was used with mass cutoff values of $M_{\text{low}}=0.1 M_{\odot}$ and $M_{\text{up}}=100 M_{\odot}$. We modelled both a single burst (δ -function) up to 15 Myr, and continuous star formation up to 10 Gyr, with metallicities of $Z = 0.020$ (Z_{\odot}) and $Z = 0.040$ ($2Z_{\odot}$), the latter matching that of M83 (Zaritsky et al. 1994, Bresolin & Kennicutt 2002). In the continuous star formation model, the Br γ equivalent width starts with a sharp drop from $\sim 500 \text{ \AA}$ to $\sim 100 \text{ \AA}$ between

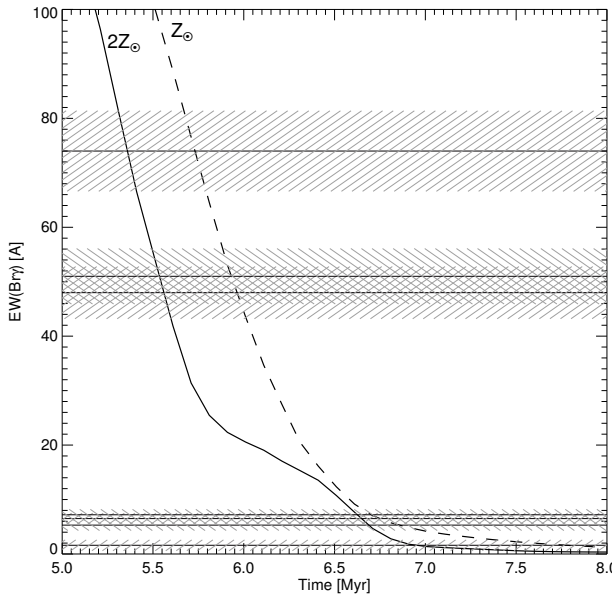


Figure 2.7 – $\text{EW}(\text{Br}\gamma)$ modelled with Starburst99 (instantaneous burst, $Z=Z_{\odot}$ (dashed line) and $Z=2Z_{\odot}$ (solid line). The horizontal lines represent $\text{EW}(\text{Br}\gamma)$ of regions A2-A5 and B1-B4, with the error range shaded. The derived ages are listed in Table 2.4.

8 and 10 Myr, then only slowly declining to $\sim 10 \text{ \AA}$ at 10 Gyr. In this case, the star forming $\text{Br}\gamma$ -defined clusters B1-B4 would have ages of 15 - 60 Myr, but the measured small values of $\text{EW}(\text{Br}\gamma)$ of the K -continuum defined clusters A1-A5 (Table 2.4) can never be reached with this mode of star formation. In a single burst model, the HeI -photons disappear at 6.5 Myr, while in the continuous model the HeI/HI ratio rises, to stabilise at some value at 8 Myr. HeI lines are not detected in A1-A5, and in the single burst model these clusters all have ages above 6.5 Myr. For these reasons, we used the instantaneous burst model to determine all the cluster ages.

Ages of the individual clusters were first estimated from the $\text{Br}\gamma$ equivalent widths, which essentially measures ages by comparing the number of OB stars to that of red supergiants. The results are in Table 2.4. No age is given for the optical peak cluster (A1), because there is no sign of recent star formation ($\text{Br}\gamma$ -emission) associated with the cluster and it is clearly older than the rest of the clusters as can be seen from its red colour in the optical HST image in Fig. 2.1 (left). We do derive ages for the other continuum-peaks (A2-A5), since these have enhanced $\text{Br}\gamma$, and show up as blue (young) clusters in the optical HST image. Cluster masses were then estimated by scaling the model $\text{Br}\gamma$ luminosity of the cluster to the measured $L_{\text{Br}\gamma}$.

Although the $\text{Br}\gamma$ equivalent width method is simple and quantitatively straightforward, it is in practise vulnerable to confusion by K -band (or, less importantly, $\text{Br}\gamma$) emission unrelated to the cluster under study, in particular when integrating over significant areas. We therefore

also explore two other methods for determining ages. For the Br γ -defined regions, where HeI lines are also detected, the HeI ($1.70\ \mu\text{m}$)/Br 10 ($1.74\ \mu\text{m}$) line ratio can also be used to give an age estimate (see Table 2.4). Using two nebular recombination lines has the advantage that the same volume is sampled and minimises the confusion by unrelated diffuse emission. The modelled ages from this line ratio are metallicity dependent and lower than those from EW(Br γ) for solar metallicity, but with twice solar metallicity (as appropriate for M83, see above) they are higher. Given the simplicity of our modelling, the agreement is generally satisfactory. It is however to be noted, that the high HeI ($1.70\ \mu\text{m}$)/Br 10 ($1.74\ \mu\text{m}$) ratio of the brightest Br γ source (B1) points to a younger age for this object than for the remaining star forming regions.

Cluster ages can also be derived from the equivalent widths of photospheric CO absorption bands. These bands originate in the cool atmospheres of red giants and supergiants and are sensitive to stellar temperature and luminosity. The CO-index is defined as the ratio between the fluxes integrated over narrow wavelength ranges (width $\sim 53\ \text{\AA}$), centred on the line and nearby continuum, expressed either in terms of magnitude or as equivalent width. We used the wavelength range definitions of Origlia et al. (1993). CO equivalent widths are stated in column (7) of Table 2.3. The strength of the CO absorption bands is one of the parameters modelled by Starburst99. However, Origlia & Oliva (2000) caution that the CO index is not reliable as an age indicator beyond $\sim 10\ \text{Myr}$, because it is observationally difficult to discriminate between strong absorption bands, and weak absorption bands with large widths (i.e., red supergiants and red giants) at these ages. We do see stellar absorption bands in all of our modelled clusters, from which we conclude the presence of stars in an evolved stage ($>5.5\ \text{Myr}$). The bands are deeper in the continuum peaks and shallower in the Br γ -defined star forming regions, which qualitatively confirms the relative ages. Again for cluster B1, a very young age of 5.3 to 5.9 Myr (depending on the choice of stellar evolutionary tracks) is indicated by its very low CO equivalent width, in agreement with the young age indicated by the HeI ($1.70\ \mu\text{m}$)/Br 10 ($1.74\ \mu\text{m}$) ratio.

Harris et al. (2001) studied 45 star clusters in the central 300 pc of M83 using optical HST data. They found that most of the clusters are in the age-range of 3 - 10 Myr, with the majority of ages between 5 and 7 Myr and the younger clusters located in region B1 in our data. The diffuse background population would be consistent with continuous star formation starting at least 1 Gyr ago. Houghton & Thatte (2008) also modelled the ages of the nuclear clusters of M83. Their single-burst model resulted in conflicting ages as derived from EW(Pa α) and W(CO), with discrepancies of a few Myr. They modelled the star formation history constructing a mixed population model by convolving several single stellar populations (SSPs) from single bursts. Their best fitting model is a sequence of bursts with a duration of 6 Myr and burst-separating times of 0.1 Myr. They again found ages in the range of 5 - 7 Myr, in agreement with Harris et al., but they did not find younger clusters and they ruled out the combination of a SSP contaminated with an old (Gyr) population. They also confirmed the supersolar metallicity. Again their youngest cluster is found in region B1.

The ages derived in this work are also in the range of 5 - 7 Myr, in good agreement with the ages from Harris et al. (2001) and Houghton & Thatte (2008). In this age range, the HeI ($1.70\ \mu\text{m}$)/Br 10 ($1.74\ \mu\text{m}$) ratio and W(CO) appear to work remarkably well as age

Table 2.4 – Cluster ages from Br γ and HeI_{1.70 μ m}/Br10_{1.74 μ m} ratio modelled with *Starburst99* (instantaneous burst), and derived star formation rates.

Region	EW(Br γ) (\AA)	Age		M_* (M_\odot) $\cdot 10^6$	$\frac{\text{HeI}_{1.70\mu\text{m}}}{\text{Br}10_{1.74\mu\text{m}}}$	Age	
		(Myr)				(Myr)	
		Z_\odot	$2Z_\odot$			Z_\odot	$2Z_\odot$
A1	0.6	-	-	-	-	-	-
A2	6.5	6.8	6.6	1.0	-	-	-
A3	1.6	7.7	7.0	0.8	-	-	-
A4	7.2	6.7	6.6	0.5	-	-	-
A5	5.3	6.9	6.7	0.04	-	-	-
B1	48	6.0	5.6	6.7	0.12	5.5	6.7
B2	74	5.7	5.4	3.5	0.10	5.7	6.8
B3	48	6.0	5.6	0.5	0.09	5.8	6.8
B4	51	5.9	5.5	0.3	0.09	5.8	6.8
bg1	2.9	6.8	7.3	-	-	-	-
bg2	2.3	6.9	7.5	-	-	-	-

indicators, giving consistent results. The fact that the young age of region B1 is not detected when using the Br γ equivalent width as age indicator is likely due to the inclusion of unrelated (foreground or background) K -band emission in the aperture, and cautions against the use of this indicator in crowded regions. Contrary to Houghton & Thatte (2008) we do not find a large discrepancy between ages derived using the various indicators (note that Houghton & Thatte did not have the HeI (1.70 μ m)/Br 10 (1.74 μ m) ratio available), and therefore no need to explore more complex star formation histories for the clusters. The fact that our (idealised) δ -function starburst models are able to represent the observables consistently, using 3 different age indicators, while continuous star formation cannot, can be taken as evidence that the individual bursts occur on timescales significantly shorter than the derived cluster ages.

Star formation in the nuclear region

The star formation rate (SFR) in the nuclear region, averaged over the past 7 Myr (slightly longer than the age of the oldest star forming region) can be estimated by using the masses derived for the star forming clusters (B1-B4 and A2-A5) and dividing by 7 Myr. The resulting nuclear star formation rate in clusters is $1.9 M_\odot \text{yr}^{-1}$. However, this star formation budget does not account for the significant amount of diffuse Br γ emission, not related to individual clusters. Typical (extinction corrected) flux levels for the diffuse Br γ are given in the “bg1” and “bg2” entries in Table 2.3. Integrated over the observed area, about 30% of the Br γ

emission comes from diffuse regions. This emission may be powered by Lyman continuum radiation leaking out of the bright HII regions, or by unclustered hot stars. In the latter case these stars may be formed in situ, or ejected from young star clusters as proposed by Kroupa & Boily (2002), or result from dissolved young star clusters. In an extensive study of young star clusters in the Antennae (NGC 4038/4039), Mengel et al. (2005) found that clusters dissolve on a timescale of approximately 10 Myr. This result is in agreement with the ages found for the clusters in the present study (all younger than 10 Myr) and the diffuse regions (older than 10 Myr), if we use the high-metallicity models. These results therefore suggest that the diffuse star formation results from clusters that have dissolved in the background field.

Including the contribution from diffuse star formation, the total star formation rate in the region observed here is $2.5 M_{\odot} \text{yr}^{-1}$ and the average star formation surface density is $3.4 \cdot 10^{-5} M_{\odot} \text{yr}^{-1} \text{pc}^{-2}$. In the brightest star formation region (B1), the star formation surface density is approximately a factor of 10 higher. The average star formation surface density found here is typical for circumnuclear starbursts of moderate luminosity, but significantly lower than that found in the active central regions of Ultraluminous Infrared Galaxies. The average star formation rate surface density found here is larger than that of 30 Doradus in the LMC, which has a star formation rate surface density of $1 - 10 M_{\odot} \text{yr}^{-1} \text{kpc}^{-2}$ over the entire HII-region, and $100 M_{\odot} \text{yr}^{-1} \text{kpc}^{-2}$ in the central 10 pc core.

2.4.3 Comparison with 15 GHz radio emission

The radio emission has both a thermal component from HII regions and a non-thermal contribution from synchrotron radiation. Qualitatively, this can be roughly confirmed by comparing the distribution of 2 cm flux to that of Br γ (HII-regions) and [FeII] from supernova remnants. In Fig. 2.8, from left to right, the 2 cm contours (red) are overlaid on Br γ , H₂ and [FeII] ($1.257 \mu\text{m}$), respectively. The Br γ -peak coincides with the brightest peak of 2 cm emission, while the three small radio peaks in region of the optical/NIR peak (i.e., near the 0,0 position in Fig. 2.8) and the small radio peak in the northeast at the edge of the SINFONI field

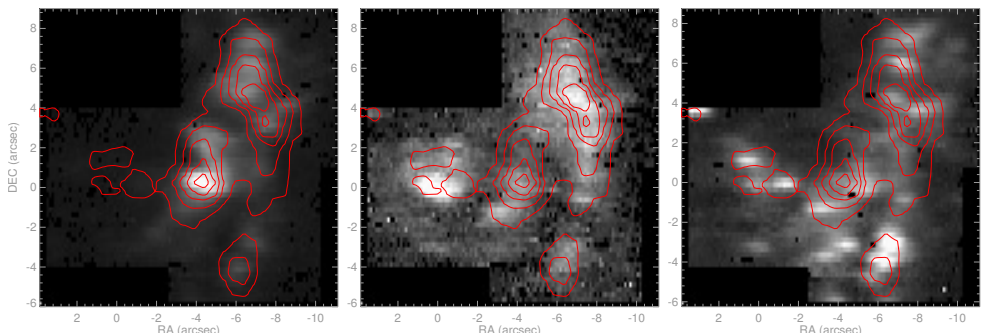


Figure 2.8 – VLA 15 GHz (2cm) radio contours, overlaid on Br γ (left), H₂ (middle) and [FeII]_{1.26 μm} (right). Contour levels are [0.25, 0.40, 0.55, 0.70, 0.85] mJy.

are identified with [FeII]-peaks. The main north-south arc of radio emission in the western part of the image closely follows the H₂-arcshape both in morphology and extent. However, this arc partly overlaps with Br γ as well as iron peaks. The thermal and non-thermal components can be separated quantitatively by means of the slope of the emission spectra, as in Turner & Ho (1994). These authors used 6 cm and 2 cm emission maps and assumed a slope of $\alpha = -0.1$ for the flat spectrum component, which they ascribed to thermal bremsstrahlung (free-free) from the brightest HII-regions, and $\alpha = -0.8$ for the steep spectrum component being non-thermal synchrotron emission.

2.4.4 [FeII] emission and supernova activity

Supernova rates in galaxies are usually estimated from the integrated radio continuum emission. The physical background and underlying assumptions are discussed in Condon (1992); see also Condon & Yin (1990), Pérez-Olea & Colina (1995) and Bressan et al. (2002). The observational basis for deriving supernova rates from radio continuum fluxes lies in the infrared-radio correlation, which is remarkably tight and linear (Condon 1992, and references therein), which is attributed to both infrared and radio emission scaling with star formation rate (however, see Bell 2003).

Supernova remnants (SNRs) also radiate strongly in near-IR [FeII] emission lines, with the brightest lines at 1.257 and 1.644 μm (Graham et al. 1987, 1990, Oliva et al. 1989, 1990). Grains in the interstellar medium are destroyed in the shock fronts of the supernova remnants, so that the iron atoms, which are normally mostly locked up in the cores of dust grains, are released into the gas phase and singly ionised by the ambient radiation field. Furthermore, rapid charge exchange with atomic hydrogen converts any Fe²⁺ rapidly into Fe⁺ (Neufeld & Dalgarno 1987), while further neutralisation by charge exchange with atomic hydrogen is prevented since that reaction is endothermic by 5.7 eV.

Based on these results, various authors attempted to use the [FeII] near-IR emission lines for a quantitative supernova rate measurement (Van der Werf et al. 1993, Calzetti 1997, Vanzì & Rieke 1997). The calibration of these relations relies on a comparison of the [FeII] line fluxes with the radio continuum at fixed frequency, and an adopted conversion factor between radio continuum flux and supernova rate (e.g., Huang et al. 1994). However, comparison of high resolution [FeII] line and radio continuum imaging of starburst galaxies indicated that the relation between [FeII] emission and radio emission was complex. Greenhouse et al. (1997) found that there was little direct correspondence between radio-luminous SNRs and peaks of [FeII] emission in M82 and suggested that [FeII] and radio emission select SNRs of different ages. In a high resolution HST imaging study of [FeII] emission of the nearby starburst galaxies M82 and NGC 253, Alonso Herrero et al. (2003) found that only 30-50% of the radio SNRs have a compact [FeII] counterpart, but 70% of the radio flux can be associated with radio SNRs if also diffuse emission is included. Only 22-27% of the [FeII] flux from M82 and NGC 253 is accounted for by discrete sources, so that most of the [FeII] emission from these galaxies is diffuse.

As can be seen in Fig. 2.8, our [FeII] image shows a substantial collection of compact sources, in marked contrast to the emission in Br γ and in H₂, which display larger continuous

Table 2.5 – Properties of the regions defined by [FeII] 1.257 μ m emission. Emission line fluxes have been corrected for extinction using the $F_{[\text{FeII}]1.26\mu\text{m}}/F_{[\text{FeII}]1.64\mu\text{m}}$ ratio, and derived quantities have been calculated from these extinction-corrected fluxes.

(1) Region	(2) ^a Size (pixels)	(3) ^b $F_{[\text{FeII}]1.26\mu\text{m}}$ eC ($\text{ergs}^{-1}\text{cm}^{-2}$) $\cdot 10^{-16}$	(4) ^c $L_{[\text{FeII}]1.26\mu\text{m}}$ (L_{\odot}) $\cdot 10^3$	(5) ^b $F_{[\text{FeII}]1.64\mu\text{m}}$ eC ($\text{ergs}^{-1}\text{cm}^{-2}$) $\cdot 10^{-16}$	(6) ^c $L_{[\text{FeII}]1.64\mu\text{m}}$ (L_{\odot}) $\cdot 10^3$
C1	300	372	23.4	273	17.1
C2	256	201	12.6	147	9.2
C3	156	87	5.5	119	7.5
C4	106	323	20.3	238	14.9
C5	92	202	12.7	149	9.4
C6	60	75	4.7	55	3.5
C7	52	114	7.2	84	5.3
C8	54	22	1.4	16	1.0
bg1 ^d	36	4.6	0.29	3.4	0.21
bg2 ^d	36	7.7	0.48	5.7	0.36

^a 1 pixel = $0''.125 \times 0''.125 = 2.725 \text{ pc} \times 2.725 \text{ pc} = 7.4 \text{ pc}^2$

^b Extinctions from line ratio $F_{[\text{FeII}]1.26\mu\text{m}}/F_{[\text{FeII}]1.64\mu\text{m}}$ (intrinsic ratio 1.36), and $A_{\lambda} \propto \lambda^{-1.8}$ (Martin & Whittet 1990).

^c Assuming $D = 4.5 \text{ Mpc}$

^d Background measurements, see Table 2.2 for the definitions of bg1 and bg2.

regions of emission. The large majority of [FeII] emission features has a counterpart in 15 GHz radio emission and *vice versa*, the only exceptions being the [FeII] emission region at coordinates $(-4, -4)$ and the radio emission region at coordinates $(-4, +2)$ in Fig. 2.8. We draw particular attention to the region around the optical peak (coordinates $(0,0)$) and northeast from that position, where a very close correspondence is observed between radio and [FeII] emission, while no Br γ emission is observed. The distribution of [FeII] emission in a large number of compact clumps, quite unlike the H₂ and Br γ distributions, suggests that most of these clumps represent remnants of individual supernovae, occurring stochastically in the nuclear region. The presence of 3 such sources in the region of the optical peak, where no active star formation occurs, indicates past star formation activity in this region, and shows directly that supernova activity can persist after active star formation has ceased.

Properties of the [FeII] emission peaks are presented in Table 2.5. After extinction correction, we find total [FeII] 1.64 μ m luminosities for the individual [FeII] peaks from 1000 to 17100 L_{\odot} . While the most luminous and extended [FeII] emission peaks may contain multiple SNRs, the least luminous and most compact regions probably represent individual SNRs, which therefore have typical [FeII] 1.64 μ m luminosities of a few thousand solar luminosities.

ties. Typical [FeII] 1.64 μm luminosities for optically selected Galactic SNRs are in the range from 0.1 to $6L_{\odot}$ (see the compilation in Morel et al. 2002), but the Galactic SNR RCW 103 is much more luminous with an [FeII] 1.64 μm luminosity of $720L_{\odot}$ (Oliva et al. 1990), and this object provides a fairer comparison, since we are here considering [FeII]-selected SNRs. The well-studied Galactic SNR IC 433 is fainter again with $L(1.257\mu\text{m})\approx 59L_{\odot}$ (Keller et al. 1995), implying an [FeII] 1.64 μm luminosity of $43L_{\odot}$. Lumsden & Puxley (1995) observed 8 extragalactic supernovae in M33, with typical [FeII] 1.26 μm luminosities of $800L_{\odot}$, implying [FeII] 1.64 μm luminosities of $580L_{\odot}$. Labrie & Pritchett (2006) found [FeII] 1.64 μm luminosities of 69 to $780L_{\odot}$ for 17 SNRs in the dwarf irregulars NGC 1569 and NGC 5253. Bright SNRs in the Large Magellanic Cloud have similar [FeII] line luminosities (Oliva et al. 1989). Morel et al. (2002) find [FeII] 1.64 μm fluxes from 6 to $695L_{\odot}$ for a sample of 42 optically selected SNRs in M33.

With [FeII] 1.64 μm luminosities of more than $1000L_{\odot}$, the [FeII] peaks found in the present data are approximately a factor of 10 more luminous than individual SNRs in the Milky Way and nearby galaxies, but comparable to the [FeII] peaks in the nearby starburst galaxy NGC 253, which have typical 1.64 μm line luminosities of $2.6 \cdot 10^3 L_{\odot}$ (Forbes et al. 1993). As shown by Morel et al. (2002), the [FeII] luminosity of a radiative SNR depends on the electron density of the post-shock gas, according to the empirical relation

$$\frac{L_{[\text{FeII}] 1.64\mu\text{m}}}{L_{\odot}} = 1.1 \frac{n_e}{\text{cm}^{-3}}. \quad (2.2)$$

This expression indicates that for a post-shock density of a few 1000 cm^{-3} , the [FeII] peaks detected in the present data are plausibly accounted for by single SNRs (with the possible exception of the most luminous and extended objects). The density of the post-shock gas can in principle be determined from the ratio of fainter [FeII] lines (Oliva et al. 1990), but none of the density-sensitive lines are detected in our data. However, the detection of thermally excited H_2 emission associated with the SNRs shows that densities of a few times 1000 cm^{-3} are readily achieved in the vicinity of the SNRs (see Sect. 2.4.5).

In our data, we also find significant diffuse [FeII] emission, accounting for 74% of the total [FeII] emission detected, and the [FeII] peaks C1-C8 indicated in Table 2.5 account for only 26% of the total emission. These proportions are quite similar to those found in M82 and NGC 253 (Alonso Herrero et al. 2003). What is the origin of this diffuse emission? In addition to strong shocks destroying the dust grains and single ionising the released iron atoms, [FeII] emission can also originate from partly ionised gas close to the ionisation fronts of HII regions (e.g., Walmsley et al. 2000, Takami et al. 2002) or in X-ray irradiated gas (e.g., Blietz et al. 1994, Mouri et al. 2000). As noted in Sect. 2.3.6, in partly ionised gas the [FeII] emission should be accompanied by [PII] line emission at $1.188\mu\text{m}$, and the absence of the [PII] line (as in our [FeII] peak regions, see Sect. 2.3.6) indicates that the [FeII] emission results from grain destruction in strong shocks. We have inspected our data for [PII] emission in regions of diffuse [FeII] emission (and not associated with recent star formation as revealed by $\text{Br}\gamma$), and find no detectable [PII] $1.188\mu\text{m}$ emission in these regions, while the [FeII] $1.26\mu\text{m}$ flux is quite high. This result directly demonstrates that also the diffuse [FeII] emission results from grain destruction in strong shocks. The diffuse emission likely results

from evolved SNRs which have lost their individual identity in but not yet cooled to general ISM temperatures. The highly shearing velocity field, as well as turbulence generated by mechanical energy injection into the ISM by the starburst, may cause the SNRs to dissolve into the ambient ISM more rapidly than in quiescent regions (such as in spiral arms or in the Milky Way), on timescales shorter than the cooling timescale of the post-shock gas.

What do these results imply for estimation of supernova rates from [FeII] line emission? It is clear that the relation between individual radio and [FeII] sources in starburst galaxies is not a simple one. Furthermore, while we have shown that the diffuse [FeII] emission also has a supernova origin, just like the diffuse non-thermal radio emission (e.g., Condon 1992), the range of luminosities and individual SNRs is very large and environment-dependent (see Eq. 2.2). While [FeII] and radio emission both correlate with supernova rate, there is with our present level of understanding no reason to expect a tight and linear relation between integrated [FeII] line fluxes of entire galaxies and their radio continuum fluxes. Indeed, while a relation between [FeII] and radio continuum fluxes for starburst galaxies exists (Forbes & Ward 1993), this relation is not linear and does not go through zero. We can only conclude that the derivation of supernova rates from [FeII] emission fluxes lies on weak grounds and should be avoided until a better understanding of the underlying physics and a proper calibration can be achieved.

2.4.5 H₂ emission

Several rovibrational H₂ lines are detected in our data and listed in Table 2.6. Low order ($v = 1-0$ and $2-1$) lines are present almost everywhere, peaking at the optical peak (region A1) and in the arc-shape that is also recognised in 2 cm radio emission (Fig. 2.8), whereas the higher order lines are exclusively present in the arc-peak (region B2), the location that coincides with the youngest star forming region (Table 2.4). Excitation mechanisms to populate the upper levels of these lines, which lie thousands of K above the ground state, are thermal excitation in shocks (e.g., supernova explosions, stellar winds, cloud collisions), or UV-photons from young OB-stars. Both of these processes can occur in star forming regions, but they populate the energy levels in different ways. In shocks, levels are populated by collisional excitation. The post-shock temperature is typically a few 1000 K, which will populate only the low energy levels (Draine et al. 1983, Hollenbach & McKee 1989, Flower & Pineau Des Forêts 2010). UV-photons have energies high enough to excite the H₂ molecules to higher electronic states, populating also the higher levels when cascading down by fluorescence (Black & Dalgarno 1976, Black & Van Dishoeck 1987). However, at high densities collisions will thermalise the lower levels even if the H₂ emission is fluorescently excited (Sternberg & Dalgarno 1989). In this case the resulting level population is characterised by thermal excitation for the lowest energy levels while higher energy levels are populated by fluorescence and thus show population levels far exceeding those expected for thermal excitation.

The H₂ line fluxes, upper level energies for the star forming region B2 are shown in Table 2.6. This table also gives N/g , the derived upper level column density N divided by the statistical weight g of the level, where the H₂ ortho/para ratio of 3 has been taken into account

Table 2.6 – H₂ emission lines from the star forming region B2. E_{up} denotes the upper level energy of the transition, and N/g is the derived column density N divided by the statistical weight g of the level.

transition	λ (μm)	E_{up}/k (K)	Flux (erg cm^{-2})	N/g (cm^{-2})
H ₂		$\cdot 10^3$	$\cdot 10^{-16}$	$\cdot 10^3$
3-1 S(3)	1.1857	19.1	11.9	0.410
3-1 S(1)	1.2330	17.8	9.60	0.629
3-1 S(0)	1.2621	17.4	13.6	6.800
2-1 S(3)	2.0735	13.9	77.8	5.360
2-1 S(2)	2.1542	13.2	6.92	1.872
2-1 S(1)	2.2477	12.5	15.4	2.095
2-0 S(1)	1.1622	12.5	14.3	2.340
2-0 Q(1)	1.2383	11.8	13.6	6.100
2-0 Q(2)	1.2419	12.1	7.03	7.990
2-0 Q(3)	1.2473	12.5	7.14	2.080
2-0 Q(4)	1.2545	13.2	3.98	2.810
1-0 S(7)	1.7480	12.8	13.1	0.852
1-0 S(6)	1.7879	11.5	5.58	1.049
1-0 S(3)	1.9576	8.36	44.1	3.933
1-0 S(2)	2.0338	7.58	21.3	7.647
1-0 S(1)	2.1218	6.95	65.9	12.140
1-0 S(0)	2.2233	6.47	22.5	25.060
1-0 Q(1)	2.4066	6.15	73.0*	28.790

in the calculation of g . The resulting values are shown in the Boltzmann diagram presented in Fig. 2.9.

The column densities of the five lowest $\nu = 1-0$ lines with upper level energies up to ~ 8000 K show a linear relation with E_{up} , and are therefore thermalised, and can be fit by a Boltzmann distribution with a corresponding excitation temperature of 1080 K. The population of the higher levels is dominated by UV-pumped fluorescence.

In contrast, at the optical peak, where no recent star formation is found, but supernova shocks are revealed in [FeII] emission, only the lowest H₂ lines are found, and with no indication for UV-excitation.

These results directly show that UV-pumping and shock excitation both occur in this starburst nucleus, and they can only be separated by the high spatial resolution of our data, which can associate particular H₂ line emission regions with either supernova shocks (traced by [FeII]) providing thermal excitation of star forming regions (traced by Br γ), providing

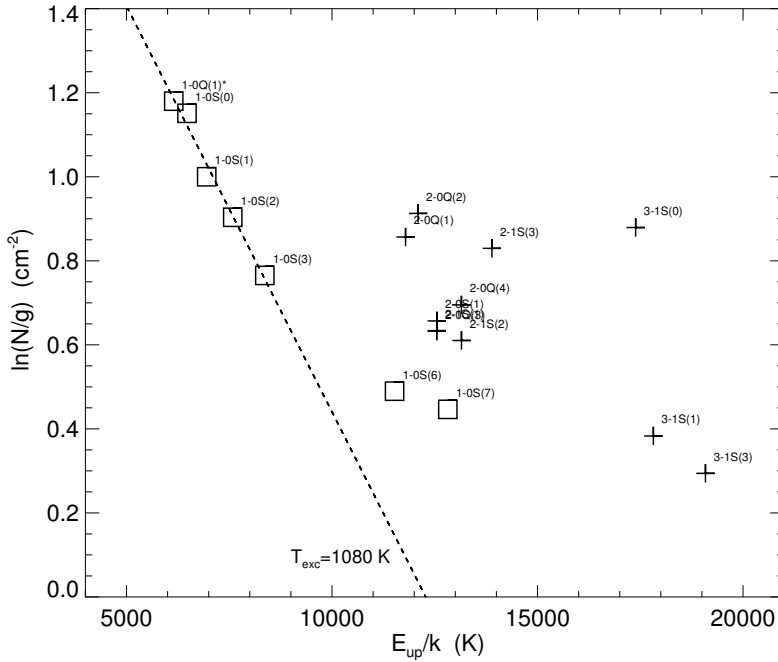


Figure 2.9 – H_2 excitation diagram for the star forming region B2. The data points are normalised to the column density of 1-0S(1). The dotted line corresponds to the Boltzmann distribution best fitting the five lowest $\nu = 1-0$ lines, with an excitation temperature of 1080 K. The $\nu = 1-0$ lines are indicated by squares, higher lines with + signs. E_{up} and N/g are as in Table 2.6.

UV-pumping. Without this spatially resolved information, separation of these two excitation mechanisms would be impossible. Summing the H_2 line fluxes in the star forming regions (B1-B4) and the shocked regions (C1-C8) in Table 2.2 shows that about two thirds of the H_2 emission results from shocks, and only one third is UV-pumped. However, approximately 75% of the total H_2 is diffuse. The diffuse emission may be either UV-excited by photons leaking out of HII regions or by widespread B stars, or shock-excited like the diffuse [FeII] emission. Pak et al. (2004) have argued that in the nearby starburst nuclei in M82 and NGC 253 and the central regions of IC 342 and NGC 6946, UV excitation is the dominant excitation mechanism when integrating over the central kpc (i.e., a region somewhat larger than considered here). In our dataset, the faintness of the $\text{H}_2 \nu = 2-11$ S(1) $2.25 \mu\text{m}$ line argues against this mechanism, since in the diffuse regions the gas is probably not sufficiently dense to thermalise the upper level of this transition. Our results would then argue for a dominant contribution of shock-excited H_2 , with at most 10% of the total $\text{H}_2 \nu = 1-0$ S(1) emission resulting from fluorescence.

2.5 Kinematics

2.5.1 Gas velocity field

Velocity fields were created for all emission lines from the shifts of the (Gaussian) fitted line centres. The velocity resolution corresponding to the instrumental dispersion is 150, 100 and 75 km/s in J, H and K respectively (see Table 2.1). Line centres are fitted with an accuracy of the order of $5 \cdot 10^{-5} \mu\text{m}$, or ~ 6 km/s. Figure 2.11 shows the velocity and velocity dispersion of H_2 (top left, right) and $\text{Br}\gamma$ (middle left, right). The velocity and velocity dispersion fields of $\text{Pa}\beta$ and $[\text{FeII}]$ are very similar to that of $\text{Br}\gamma$ and are therefore not shown. The velocity field of H_2 deviates from the other velocity fields in the region southwest of the optical peak, and this feature will be discussed below (Sect. 2.5.4). The $\text{Br}\gamma$ velocity dispersion (Fig. 2.11, middle right) displays a peak at $(-9, 6)$ and a ridge from $(-3, -4)$ to $(-6, 3)$. Both features can also be recognised in H_2 (top right), but are less clear because of low signal. On the other hand, the H_2 velocity dispersion shows a peak (~ 75 km/s) at the optical peak $(0, 0)$, which is not recognised in the other gas velocity dispersion maps.

2.5.2 Stellar velocity field

Due to their intrinsic sharpness, the stellar CO photospheric absorption bands at $2.3 \mu\text{m}$ offer an excellent feature for probing the stellar kinematics. We have used a set of 3 (late type) template stars, and used the PPXF (Penalised Pixel Fitting) package from Cappellari & Emsellem (2004) to derive the stellar velocity and velocity dispersion fields. The template stars had been observed with SINFONI, using the same settings as for the M83 data, in order to

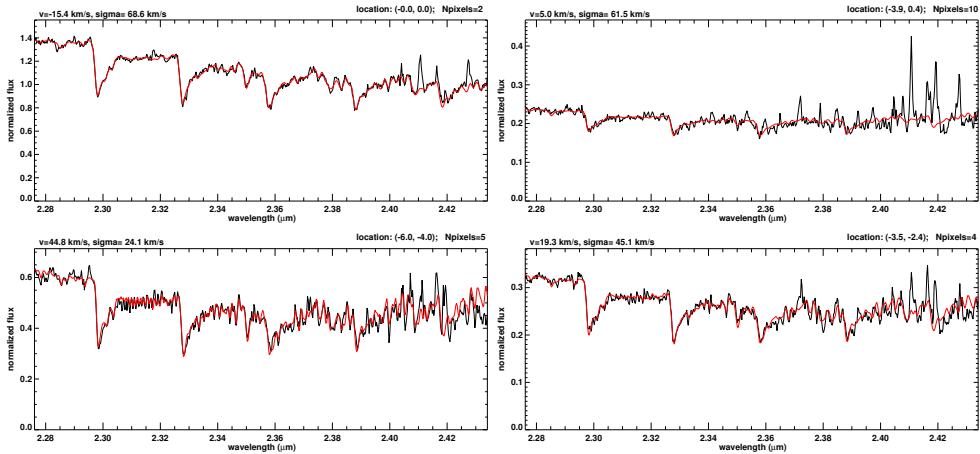


Figure 2.10 – Spectra (black) and PPXF-fits (red) with 3 stellar templates of the spectrum (a) at $(0, 0)$, the optical peak A1 (b) at $(-3.8, 0.2)$: the starburst location B1, (c) at $(-5.9, -4.1)$: cluster A2 and (d) at $(-3.4, -2.5)$ the centre of outer K -band isophotes. Velocities are relative to the systemic velocity.

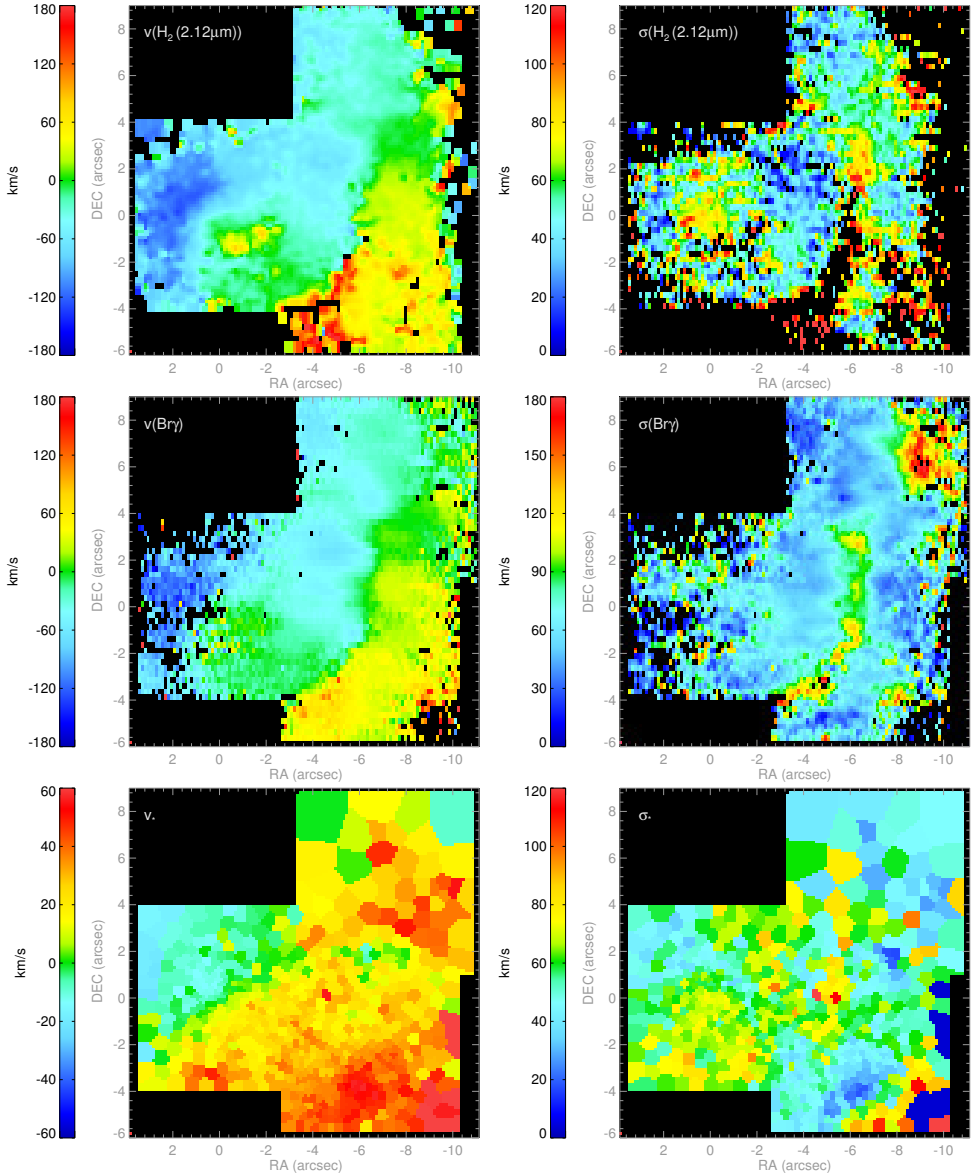


Figure 2.11 – Velocity (left) and velocity dispersion (right). From top to bottom: H_2 , $\text{Br}\gamma$ and stars (CO 2.29 μm). In all cases, v_{sys} is set to 520 km/s.

compensate for the effects of instrumental resolution on the fit results. First pixels were combined into bins using a Voronoi tessellation, requiring a S/N ratio of 50 for each bin. Then the combined spectrum of each bin was fitted with the best combination of stars, using a range of velocities and velocity dispersions. The resulting fitted spectra very accurately describe the

observed spectra, in the lower signal regions as well as in the highest continuum peaks, as shown in the sample spectra in Fig. 2.10.

The bottom panel of Fig. 2.11 shows the resulting stellar velocity and velocity dispersion fields. The stellar velocity field (left) looks quite regular, with a high gradient at the optical peak (0,0). The signal in the upper right field is somewhat low, as can be seen from the larger bins, resulting in a somewhat less regular appearance. Overall, the stellar velocity field shows a number of remarkable differences with respect to the gas velocity field, in particular in the region around the optical peak.

Turning now to the stellar velocity dispersion field (Fig. 2.11, lower right), it is remarkable that it does not show a clear peak in the entire region under study. There is a weak enhancement in stellar velocity dispersion at the position of the optical peak (~ 75 km/s) but this enhancement extends towards the south as well and does not seem to be centred at the optical peak. We also do not find a clear peak in stellar velocity dispersion west of the optical peak, at the position where the putative dark nucleus of Thatte et al. (2000) would be located. Comparing our data directly with the long-slit spectroscopy of Thatte et al. (2000), we do not confirm the peak in stellar velocity dispersion $2.7''$ southwest of the nucleus found by these authors. A very small enhancement in stellar velocity dispersion is found $5''$ west of the optical peak, but this position corresponds to one of the main star forming regions and is located outside the position error circle of the putative dark nucleus. In order to demonstrate that our data have more than sufficient S/N for this conclusion to hold, we explicitly include in Fig. 2.10 the central position of the fainter *K*-band isophotes, where the dark nucleus should be located. It can be seen that the observed spectrum is very well fit using the parameters indicated. We therefore firmly discard the scenario of a dark nucleus at the centre of the faint *K*-band isophotes, in agreement with Houghton & Thatte (2008).

2.5.3 Rotating ring structure

Sakamoto et al. (2004) have observed a ring of molecular gas, rotating around a point coincident with the centre of the fainter *K*-band isophotes, offset from the optical peak by about $3''$. In principle our kinematic data should allow us to fully determine the parameters of this ring, but in practise this is not possible since our velocity field covers only part of the ring. We therefore fix the centre of the ring at the position found by Sakamoto et al. (2004), and then fit rings of various position angles, inclinations and inner and outer radii to the H_2 velocity field. Of these parameters, the outer ring radius is not constrained at all by our data, and the other parameters are only weakly constrained. A possible geometry with a ring inclination of 55° , major axis position angle of 165° , and inner radius of 120 pc is shown in Fig. 2.12. While we do not insist on the precise values of these parameters (which can unfortunately not be determined accurately due to the partial spatial coverage of the ring), Fig. 2.12 shows a number of striking features, which are common to all acceptable solutions.

1. The ring has a very well-defined inner edge, seen quite clearly by the “jump” in rotation velocities in Fig. 2.12 in the western half of the ring. At positions inside the inner edge, the H_2 velocity field no longer follows the rotating of the ring, but shows a different

kinematic major axis. It is possible that this jump marks the transition between two orbit families in the barred potential of M83, as also suggested by Sakamoto et al. (2004). Indeed, Regan & Teuben (2003) show that nuclear rings in barred potentials are associated with the transition between two orbit families. The ridges of high values in the gas velocity dispersion fields now also have a simple explanation and result from beam smearing where the transition between the two velocity fields (and the two orbit families) occurs. We also note that within the inner edge of the rotating ring, there is little resemblance of the gas and stellar velocity fields, except in the vicinity of the optical peak.

2. A deviation in the velocity field is found at the position of the optical peak, and here the velocity field is dominated by rotation around the optical peak position, as is also seen for the stellar velocity field. Clearly, despite the lack of a stellar velocity dispersion peak, the optical peak represents considerable mass, and dominates the gravitational potential in its immediate surroundings. It is also striking that the optical peak is located quite close to the inner edge of the rotating gas ring.

2.5.4 Nature of the optical peak

Using our kinematic data we can try to constrain the dynamical mass of the optical peak. Taking a slice through the H₂ velocity field with a width of 0.8'' going through the optical peak at a position angle of 43° (maximising the velocity gradient) reveals a peak line-of-sight rotation velocity of 85 km/s at a radius 1.4'' (31 pc) from the optical peak. Assuming a spherical mass distribution, the enclosed mass is then $2.6 \cdot 10^7 / \sin^2 i M_{\odot}$ where i is the orbital inclination of the gas orbiting the optical peak. Unfortunately, i cannot be determined, and it is very uncertain whether its value would be the same as for M83 as a whole ($i=24^{\circ}$, Comte 1981). We therefore consider the derived mass a lower limit and note that it could be substantially higher.

With this mass, it is possible that the optical peak could be an evolved superstarcluster, which can have masses of the order to $10^7 M_{\odot}$, but we consider this unlikely. In the first place, this would require $i \sim 90^{\circ}$ in order not to exceed observed masses of such objects, and second, such superstarclusters are typically associated with mergers or in dwarf irregular galaxies, and not with grand-design spirals.

The only remaining possibilities are an accreted dwarf galaxy, or an $m = 1$ distortion leading to a displacement of the optical peak from the kinematic nucleus (which would also be the central position of the fainter isophotes). The various arguments are extensively discussed in Houghton & Thatte (2008) and Knapen et al. (2010) and we do not repeat that discussion here. Our results however provide several new elements in this discussion.

1. Our data show that the optical nucleus, while not actively forming stars now, has undergone an episode of star formation in the past, as shown by the presence of several luminous SNRs. This result does not favour any model in particular, but must form part of any scenario constructed to account for the nature of the optical peak.

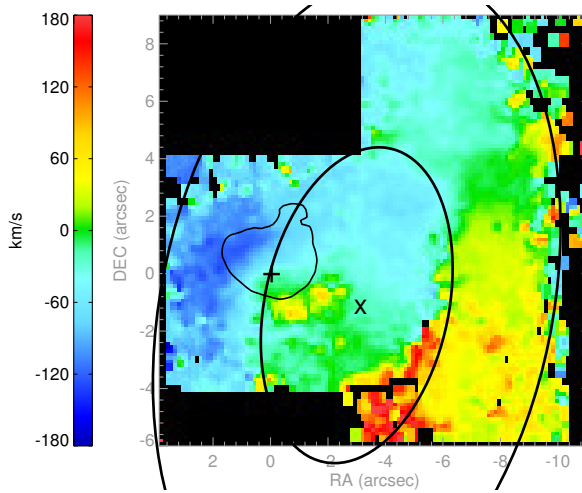


Figure 2.12 – H_2 velocity map. The plus-sign (+) indicates the centre of the optical peak, the cross (x) indicates the location of the centre of K -band isophotes. The ellipse indicates the rotating ring, centred on x (inclination 55° , PA of major axis 165°), also observed in CO by Sakamoto et al. (2004).

- Our data also indicate that the optical peak is located (in projection) quite close to the inner edge of the molecular ring (see Sect. 2.5.3). Obviously, in this complex region we cannot rule out a chance alignment, but if real, this geometry suggests a connection between the ring and the optical peak. It has been suggested that a dynamical relation exists between star clusters and gaseous rings (Van de Ven & Chang 2009) but in that scenario the star clusters would be expected to lie outside the gas ring, contrary to the present situation. An alternative possibility is that the optical nucleus is responsible for the sharp inner edge of the gas ring (Sect. 2.5.3) by accreting gas from its inner edge. Clearly a substantial mass concentration such as the optical peak should affect the structure of the circumnuclear ring if they are physically associated, and indeed Sakamoto et al. (2004) observe an asymmetry in the ring. Note also that the distribution of star formation is asymmetric and concentrated west of the dynamic centre, while the optical nucleus is located east of the dynamical centre. We finally note that the optical peak is displaced blueward in velocity by about 25 km/s from the systemic velocity, as noted by Houghton & Thatte (2008). It is therefore also possible that its motion lies not in the plane of M83, or in that of the circumnuclear molecular ring.

2.6 Summary

The inner 330×330 parsec of M83 is a complex region. Previous studies have shown that the optical peak does not lie at the centre of the fainter isophotes, leading to the suggestion that the galaxy would host a hidden mass concentration at that position. Millimetre observations

revealed that the centre of the fainter isophotes is also the kinematic centre of the galaxy, and forms the centre of a circumnuclear molecular ring.

Our new near-IR integral field spectroscopic data clearly reject the idea of a hidden mass concentration at the kinematic centre, in agreement with Houghton & Thatte (2008) and Knapen et al. (2010). The emerging picture is one where the nuclear region shows a pronounced asymmetry with respect to the kinematic centre. East of the kinematic centre the optical peak is found, which has a mass of at least $2.6 \times 10^7 M_{\odot}$ and possibly significantly higher. This optical peak may result from an $m = 1$ disturbance of the central region, or may be the remnant of an accreted dwarf galaxy. Whatever its origin, it shows no current star formation, but displays evidence of a recently terminated burst of star formation, given the presence of luminous supernova remnants. The optical peak lies close to the inner edge of the circumnuclear ring, although a chance alignment cannot be ruled out. If this association is real, the optical peak may be responsible for the sharp inner edge of the circumnuclear ring.

Active star formation is concentrated in the region west of the kinematic centre. The young clusters in this region have ages between 5 and 7 Myr, and account for 70% of the total Br γ emission in our dataset (the remaining 30% being diffuse emission). The small age spread suggests a coherent episode of star formation resulting over an approximately 250 pc region. Since the sound travel time over 250 pc would be about 600 Myr (for a 10 km/s sound speed), these results suggest a global instability over a 250 pc region as the trigger for the burst of star formation in this region.

[FeII] emission in our data reveals a large number of compact clumps, quite unlike the distribution of Br γ or H₂ emission. These clumps likely represent individual SNRs, or for the most extended and luminous clumps possibly a small number of SNRs. The integrated [FeII] emission is however dominated by a diffuse component, accounting for 74% of the total [FeII] emission line flux. The large [FeII] 1.257 μm /[PII] 1.188 μm line ratio in the diffuse regions shows that the diffuse [FeII] originates from strong shocks, likely resulting from supernova explosions, just like the compact [FeII] emission.

H₂ rovibrational line emission is found in compact regions associated both with SNRs (where purely thermal H₂ line ratios are found) and with star forming regions (where line ratios reveal UV-pumped fluorescence). Summing over the compact regions, one third of the emission is UV-pumped and two-thirds is shock-excited. However, like for [FeII], the total H₂ emission is dominated by a diffuse component accounting for 75% of the total emission. This diffuse emission is probably thermally excited, given the faintness of the H₂ $v = 2-1$ S(1) line.

In the gas velocity fields, the circumnuclear gas ring observed by Sakamoto et al. (2004) can be recognised. The velocity fields show that this ring has a well defined inner edge. Within the inner edge of the ring a sharp change in kinematic major axis is observed, which may be due to the different orbit families in a barred potential. The gas velocity fields also show rotation around the optical peak in a localised region centred on this peak, and we use this rotation to assign a lower limit to the mass of the optical peak.

Considering the central 330×330 pc of M83 as a whole, its strong asymmetry with respect to the kinematic centre is its most striking feature. This asymmetry manifests itself not only in the eastward displacement of the optical peak but also in the fact that active star

formation is concentrated in the west. It is likely that these two opposite displacements result from a common physical mechanism, and that the large-scale instability giving rise to the synchronised star formation west of the nucleus is related to the same mechanism that resulted in the eastward displacement of the optical peak.

References

- Alonso Herrero, A., Rieke, G. H., Rieke, M. J., & Kelly, D. M. 2003, *AJ*, 125, 1210
- Bell, E. F. 2003, *ApJ*, 586, 794
- Black, J. H. & Dalgarno, A. 1976, *ApJ*, 203, 132
- Black, J. H. & Van Dishoeck, E. F. 1987, *ApJ*, 322, 412
- Blietz, M., Cameron, M., Drapatz, S., et al. 1994, *ApJ*, 421, 92
- Bonnet, H., Abuter, R., Baker, A., et al. 2004, *The Messenger*, 117, 17
- Bresolin, F. & Kennicutt, Jr., R. C. 2002, *ApJ*, 572, 838
- Bressan, A., Silva, L., & Granato, G. L. 2002, *A&A*, 392, 377
- Calzetti, D. 1997, *AJ*, 113, 162
- Cappellari, M. & Emsellem, E. 2004, *PASP*, 116, 138
- Carter, B. S. & Meadows, V. S. 1995, *MNRAS*, 276, 734
- Comte, G. 1981, *A&AS*, 44, 441
- Condon, J. J. 1992, *ARA&A*, 30, 575
- Condon, J. J. & Yin, Q. F. 1990, *ApJ*, 357, 97
- Cowan, J. J., Roberts, D. A., & Branch, D. 1994, *ApJ*, 434, 128
- Díaz, R. J., Dottori, H., Aguero, M. P., et al. 2006, *ApJ*, 652, 1122
- Draine, B. T., Roberge, W. G., & Dalgarno, A. 1983, *ApJ*, 264, 485
- Eisenhauer, F., Abuter, R., Bickert, K., et al. 2003, in Presented at the Society of Photo-Optical Instrumentation Engineers (SPIE) Conference, Vol. 4841, Society of Photo-Optical Instrumentation Engineers (SPIE) Conference Series, ed. M. Iye & A. F. M. Moorwood, 1548–1561
- Elmegreen, D. M., Chromey, F. R., & Warren, A. R. 1998, *AJ*, 116, 2834
- Fathi, K., Beckman, J. E., Lundgren, A. A., et al. 2008, *ApJ*, 675, L17
- Flower, D. R. & Pineau Des Forêts, G. 2010, *MNRAS*, 406, 1745
- Forbes, D. A. & Ward, M. J. 1993, *ApJ*, 416, 150
- Forbes, D. A., Ward, M. J., Rotaciuc, V., et al. 1993, *ApJ*, 406, L11
- Gallais, P., Rouan, D., Lacombe, F., Tiphene, D., & Vauglin, I. 1991, *A&A*, 243, 309
- Graham, J. R., Wright, G. S., & Longmore, A. J. 1987, *ApJ*, 313, 847
- Graham, J. R., Wright, G. S., & Longmore, A. J. 1990, *ApJ*, 352, 172
- Greenhouse, M. A., Satyapal, S., Woodward, C. E., et al. 1997, *ApJ*, 476, 105
- Harris, J., Calzetti, D., Gallagher, III, J. S., Conselice, C. J., & Smith, D. A. 2001, *AJ*, 122, 3046
- Hollenbach, D. & McKee, C. F. 1989, *ApJ*, 342, 306
- Houghton, R. C. W. & Thatte, N. 2008, *MNRAS*, 385, 1110
- Huang, Z. P., Thuan, T. X., Chevalier, R. A., Condon, J. J., & Yin, Q. F. 1994, *ApJ*, 424, 114
- Hummer, D. G. & Storey, P. J. 1987, *MNRAS*, 224, 801
- Keller, L. D., Jaffe, D. T., Pak, S., Luhman, M. L., & Claver, C. F. 1995, in *Revista Mexicana de Astronomía y Astrofísica*, vol. 27, Vol. 3, *Revista Mexicana de Astronomía y Astrofísica Conference Series*, ed. M. Pena & S. Kurtz, 251–+
- Knapen, J. H., Sharp, R. G., Ryder, S. D., et al. 2010, *MNRAS*, 1301
- Kroupa, P. & Boily, C. M. 2002, *MNRAS*, 336, 1188
- Labrie, K. & Pritchett, C. J. 2006, *ApJS*, 166, 188
- Lancon, A. & Rocca-Volmerange, B. 1996, *New A*, 1, 215

- Leitherer, C., Schaerer, D., Goldader, J. D., et al. 1999, *ApJS*, 123, 3
- Lumsden, S. L. & Puxley, P. J. 1995, *MNRAS*, 276, 723
- Lumsden, S. L., Puxley, P. J., & Hoare, M. G. 2001, *MNRAS*, 320, 83
- Lumsden, S. L., Puxley, P. J., Hoare, M. G., Moore, T. J. T., & Ridge, N. A. 2003, *MNRAS*, 340, 799
- Maddox, L. A., Cowan, J. J., Kilgard, R. E., et al. 2006, *AJ*, 132, 310
- Martin, P. G. & Whittet, D. C. B. 1990, *ApJ*, 357, 113
- Martins, F., Schaerer, D., & Hillier, D. J. 2005, *A&A*, 436, 1049
- Mast, D., Díaz, R. J., & Agüero, M. P. 2006, *AJ*, 131, 1394
- Mengel, S., Lehnert, M. D., Thatte, N., & Genzel, R. 2005, *A&A*, 443, 41
- Moorwood, A., Finger, G., Biereichel, P., et al. 1992, *The Messenger*, 69, 61
- Morel, T., Doyon, R., & St-Louis, N. 2002, *MNRAS*, 329, 398
- Mouri, H., Kawara, K., & Taniguchi, Y. 2000, *ApJ*, 528, 186
- Neufeld, D. A. & Dalgarno, A. 1987, *Phys. Rev. A*, 35, 3142
- Nussbaumer, H. & Storey, P. J. 1988, *A&A*, 193, 327
- Oliva, E., Marconi, A., Maiolino, R., et al. 2001, *A&A*, 369, L5
- Oliva, E., Moorwood, A. F. M., & Danziger, I. J. 1989, *A&A*, 214, 307
- Oliva, E., Moorwood, A. F. M., & Danziger, I. J. 1990, *A&A*, 240, 453
- Origlia, L., Moorwood, A. F. M., & Oliva, E. 1993, *A&A*, 280, 536
- Origlia, L. & Oliva, E. 2000, *A&A*, 357, 61
- Pak, S., Jaffe, D. T., Stacey, G. J., et al. 2004, *ApJ*, 609, 692
- Pérez-Olea, D. E. & Colina, L. 1995, *MNRAS*, 277, 857
- Regan, M. W. & Teuben, P. 2003, *ApJ*, 582, 723
- Rigby, J. R. & Rieke, G. H. 2004, *ApJ*, 606, 237
- Sakamoto, K., Matsushita, S., Peck, A. B., Wiedner, M. C., & Iono, D. 2004, *ApJ*, 616, L59
- Shields, J. C. 1993, *ApJ*, 419, 181
- Sternberg, A. & Dalgarno, A. 1989, *ApJ*, 338, 197
- Takami, M., Usuda, T., Sugai, H., et al. 2002, *ApJ*, 566, 910
- Thatte, N., Tecza, M., & Genzel, R. 2000, *A&A*, 364, L47
- Thim, F., Tammann, G. A., Saha, A., et al. 2003, *ApJ*, 590, 256
- Turner, J. L. & Ho, P. T. P. 1994, *ApJ*, 421, 122
- Vacca, W. D. 1994, *ApJ*, 421, 140
- Van de Ven, G. & Chang, P. 2009, *ApJ*, 697, 619
- Van der Werf, P. P., Genzel, R., Krabbe, A., et al. 1993, *ApJ*, 405, 522
- Vanzi, L. & Rieke, G. H. 1997, *ApJ*, 479, 694
- Vanzi, L., Rieke, G. H., Martin, C. L., & Shields, J. C. 1996, *ApJ*, 466, 150
- Vázquez, G. A. & Leitherer, C. 2005, *ApJ*, 621, 695
- Walmsley, C. M., Natta, A., Oliva, E., & Testi, L. 2000, *A&A*, 364, 301
- Zaritsky, D., Kennicutt, Jr., R. C., & Huchra, J. P. 1994, *ApJ*, 420, 87

The nuclear dynamics of Arp 220



L. Vermaas and P. P. van der Werf

Abstract

We present high-resolution K -band integral field spectroscopy of the nearby Ultraluminous Infrared galaxy Arp 220. The observations provide a detailed view of the nuclear stellar and nebular emission, and allow determinations of both the gas and stellar velocity field, providing independent probes of the dynamical mass. While the stellar emission and the Br γ emission show the two nuclei, the H₂ emission is dominated by a large-scale regularly rotating disk. The stellar velocity field shows that the nuclei are counter-rotating with respect to each other, in agreement with the nuclear gas components as measured from higher resolution CO data. The stellar velocity dispersion does not reveal any peaks. The total dynamical mass of the stellar nuclei is $M_{*,\text{tot}} = (1.2 \pm 0.4) \cdot 10^{10} M_{\odot}$, where the error is dominated by the uncertainty in the effective radii. This value is in excellent agreement with the dynamical mass within 0.6 kpc determined from the H₂ velocity field, which is $M_{\text{tot}} = (1.2 \pm 0.6) \cdot 10^{10} M_{\odot}$, where the uncertainty is dominated by the uncertainty in the inclination of the disk. We find that the molecular gas, with a mass of $5 \times 10^9 M_{\odot}$ constitutes a significant fraction of the dynamical mass. The K -band stellar mass to light ratio, corrected for extinction is $M/L_K \sim 0.05$, with at least a factor of two uncertainty resulting from the uncertainty in the extinction correction. Even taking these uncertainties into account, this value indicates an important starburst contribution to the nuclear K -band emission.

3.1 Introduction

The galaxy Arp 220 is the closest ultraluminous infrared galaxy (ULIRG), with a luminosity distance $D_L = 77 \text{ Mpc}$ (using a flat cosmology with $H_0 = 73 \text{ km s}^{-1} \text{ Mpc}^{-1}$, $\Omega_b = 0.27$ and $\Omega_\Lambda = 0.73$, so that $1'' = 400 \text{ pc}$) and an infrared luminosity (defined as the luminosity between 8 and $1000 \mu\text{m}$ in the rest frame) $L_{\text{IR}} = 1.5 \cdot 10^{12} L_\odot$ (Sanders et al. 2003). It was the first galaxy identified as a ULIRG from the IRAS survey (Soifer et al. 1984). It shows a double nucleus at near-infrared (Graham et al. 1990, Scoville et al. 1998), mid-infrared (Soifer et al. 1999), (sub)millimetre (Scoville et al. 1997, Sakamoto et al. 1999, Downes & Eckart 2007, Sakamoto et al. 2008, Aalto et al. 2009, Matsushita et al. 2009) and radio (Norris 1988, Rodríguez-Rico et al. 2005) wavelengths, with a projected nuclear separation $0''.95 \approx 0.36 \text{ kpc}$. Tidal tails have been detected in the optical regime (Joseph & Wright 1985). This galaxy, like ULIRGs in general, is thus in a final stage of merging and has a large concentration of gas in its centre. The nuclear region harbours an OH megamaser (Baan et al. 1982, Lonsdale et al. 1998, Rovilos et al. 2003) and also displays H_2CO megamaser emission (Baan et al. 1986, 1993, Baan & Haschick 1995, Araya et al. 2004). The molecular gas component in the nuclear region is extraordinarily concentrated: Scoville et al. (1991) estimated an average molecular gas density of 2900 cm^{-3} and surface density of $8 \times 10^4 M_\odot \text{ pc}^{-2}$. Observations of density tracing molecules such as CS, HCN and HCO^+ indicate that the bulk of the molecular gas is dense (Solomon et al. 1990) with densities in the range of 10^{5-6} cm^{-3} (Greve et al. 2009, Papadopoulos et al. 2010a,b).

Scoville et al. (1997) first showed two compact sources in CO $J = 1-0$ and dust continuum observations, embedded in an extended disk-like component of approximately a kpc in diameter. This was confirmed by Downes & Solomon (1998), who estimated the total gas mass within the central region to be approximately $5 \cdot 10^9 M_\odot$, of which 90% is located in the nuclear region within a radius of 600 pc (including both nuclei). The gas mass of the western nucleus was estimated to be $1 \cdot 10^9 M_\odot$, while that for the eastern nucleus was $6 \cdot 10^8 M_\odot$. Similar gas masses were found from CO $J = 2-1$ imaging at $0''.5$ resolution by Sakamoto et al. (1999), who found the gaseous disks in the two nuclei to counter-rotate, which is also observed in HI absorption observations (Mundell et al. 2001).

The origin of the infrared luminosity, intense star formation or a significant contribution from an Active Galactic Nucleus (AGN), has been debated for decades. The relative faintness of hydrogen recombination lines such as Br γ has been used to argue in favour of an obscured AGN (Rieke et al. 1985), but as shown by van der Werf (2001), this is naturally expected in a starburst dominated by compact HII regions, where a large fraction of UV photons is absorbed by dust, so that starburst analysis based on standard (dust-free) photoionization models yields incorrect results. The presence of intense star formation in the nuclei is shown directly by radio VLBI measurements, which resolve the radio emission from the two nuclei into large numbers of radio supernova remnants (Smith et al. 1998, Rovilos et al. 2005, Lonsdale et al. 2006, Parra et al. 2007), and through radio recombination lines from the nuclei (Zhao et al. 1996, Anantharamaiah et al. 2000, Rodríguez-Rico et al. 2005). Optical studies of the Arp 220 stellar system also reveal a young stellar population and massive young super star clusters (Shaya et al. 1994, Shioya et al. 2001a, Wilson et al. 2006, Rodríguez Zaurín

et al. 2008). Models to account for these properties also point towards a strongly obscured nuclear starburst (Shioya et al. 2001b). There is also a prominent optical superwind and X-ray (Heckman et al. 1987, 1996, Arribas et al. 2001, McDowell et al. 2003, Colina et al. 2004), presumably powered by this starburst. The question is therefore not whether a starburst is present in Arp 220, but whether it is the only power source. Hard X-ray and soft γ -ray observations failed to provide direct evidence for an AGN (Dermer et al. 1997, Iwasawa et al. 2001, Clements et al. 2002, Iwasawa et al. 2005), but an AGN hidden by a column density of at least $5 \cdot 10^{24} \text{ cm}^{-2}$ cannot be ruled out. Very large amounts of extinction towards the source of luminosity, irrespective of its nature, are certainly indicated by observations in the mid-infrared (Spoon et al. 2004, 2007). The fact that even mid-infrared tracers show no high-excitation lines that could betray the presence of a hidden AGN (Genzel et al. 1998, Imanishi & Dudley 2000, Imanishi et al. 2006, Armus et al. 2007, Imanishi et al. 2007, Farrah et al. 2007, Risaliti et al. 2010).

Early near-IR spectra of Arp 220 (Rieke et al. 1985, Goldader et al. 1995) showed prominent H_2 2.12 μm emission lines, and early images of the $\text{Pa}\beta$ and [Fe II] near-IR J -band lines were presented by Armus et al. (1995b). Near-IR long slit spectroscopy of Arp 220 in the H and K -bands was presented first by Armus et al. (1995a) and Larkin et al. (1995). The latter authors showed that that hydrogen recombination lines ($\text{Pa}\beta$, $\text{Br}\gamma$) in Arp 220 are associated with the near-IR nuclei, while the H_2 rovibrational 2.12 μm line and [Fe II] have a significant part of their flux in between. They also suggested that H_2 and [Fe II] are also kinematically decoupled from $\text{Pa}\beta$ and $\text{Br}\gamma$.

The near-infrared K -band offers the opportunity for simultaneously measuring gas kinematics (from various emission lines) and stellar kinematics (from sharp stellar photospheric absorption features). The first analysis of stellar kinematics in Arp 220 using photospheric features in the K -band was done by Doyon et al. (1994) using long slit spectroscopy, resulting in a stellar velocity dispersion $\sigma_* = 150 \pm 21 \text{ km s}^{-1}$. The same technique was used in a series of much more comprehensive and sensitive studies of significant samples of ULIRGs and QSOs (Genzel et al. 2001, Tacconi et al. 2002, Dasyra et al. 2006a,b). These studies indicated that the stellar dynamics of ULIRGs is dominated by random motions, but that rotation is often important as well. Pre-merging ULIRGs were found to be major mergers where in most cases the merging galaxies have similar masses, and the end products of the mergers were found to be moderate mass ellipticals.

The advent of near-IR integral field spectroscopy enables a new step forwards in this field. Where slit observations can be affected by kinematic misalignments, integral field data allow a clean separation of rotation and dispersion over the field. The high resolution afforded by adaptive optics is an additional advantage that minimises beam smearing and allows accurate measurements of velocity dispersion even in the presence of strong velocity gradients. A final advantage of near-IR integral field spectroscopy is the presence of nebular emission lines, that provide an independent probe of the gravitational potential (e.g., Neumayer et al. 2007, Cappellari et al. 2009). In order to fully explore this method, we here present and analyse adaptive-optics assisted near-IR integral field spectroscopy of Arp 220.

Table 3.1 – K-band continuum and line fluxes in both nuclei, measured in a rectangular region of $1''0 \times 1''25$ (see section 3.3.1). Errors in the fluxes are typically 10%.

	F_{east}	F_{west}	
K cont ($\lambda_c=2.2\mu\text{m}$)	$1.65 \cdot 10^{-12}$	$2.01 \cdot 10^{-12}$	$\text{erg s}^{-1} \text{cm}^{-2} \mu\text{m}^{-1}$
H ₂ (2.12 μm)	$37.5 \cdot 10^{-16}$	$42.6 \cdot 10^{-16}$	$\text{erg s}^{-1} \text{cm}^{-2}$
Br γ (2.17 μm)	$18.1 \cdot 10^{-16}$	$15.2 \cdot 10^{-16}$	$\text{erg s}^{-1} \text{cm}^{-2}$
Br δ (1.95 μm)	$7.8 \cdot 10^{-16}$	$8.5 \cdot 10^{-16}$	$\text{erg s}^{-1} \text{cm}^{-2}$

3.2 Observations and data reduction

The central region of Arp 220 was observed with SINFONI, the Spectrograph for INtegral Field Observations in the Near Infrared (1.1 - 2.45 μm), which is installed on UT4 of the VLT (Eisenhauer et al. 2003, Bonnet et al. 2004). The observations were carried out in the night of July 19, 2009. The Laser Guide Star was used for Adaptive Optics. Tip/tilt correction was attempted on the optical galaxy, but due to its faintness it does not provide a strong correction. The intermediate platescale was used, with a field of view of $3'' \times 3''$ onto 64×64 spatial pixels. Each of these pixels is projected onto 2218 spectral elements in the K-band, with a central wavelength of 2.2 μm . This results in spatial pixels with a resolution of $0''.05 \times 0''.10$, and a spectral resolution $\lambda/\Delta\lambda$ of 4000.

The nuclear separation of Arp 220 is about $1''$, so with this setup both nuclei and their surroundings can be observed in one field. For the pointings, an ABA' nodding mode was used, i.e. object-sky-object with equal integration times of 900 s, with the A' frame slightly shifted with respect to the A frame. The total (on-source) integration time was 5×900 s, or 75 minutes.

The data were reduced with the SINFONI pipeline, version 2.0.5, which was developed by ESO and the Max-Planck-Institut für extraterrestrische Physik. The default procedure included corrections for non-linearity, distortion and wavelength calibration.

For both flux calibration and telluric feature removal, a standard star was observed with the same setup as used for the science frames, typically an early type star containing few stellar lines in the near-IR. After standard reduction, the average stellar spectrum was extracted and the photospheric stellar lines were removed (Br γ). Finally, each spectrum of the reduced object frame was divided by this extracted spectrum. The size of the point spread function (PSF) is estimated to be $0''.4$ (150 pc); this fairly large PSF results from the lack of a suitably bright tip-tilt star.

3.3 Results

The continuum was determined by linear interpolation of the broad-band spectra, emission lines were fitted with single Gaussians in each pixel. The resulting maps of the K-band continuum, Br γ and the rovibrational H₂ (2.12 μm) line emission are shown in Fig. 3.1. The

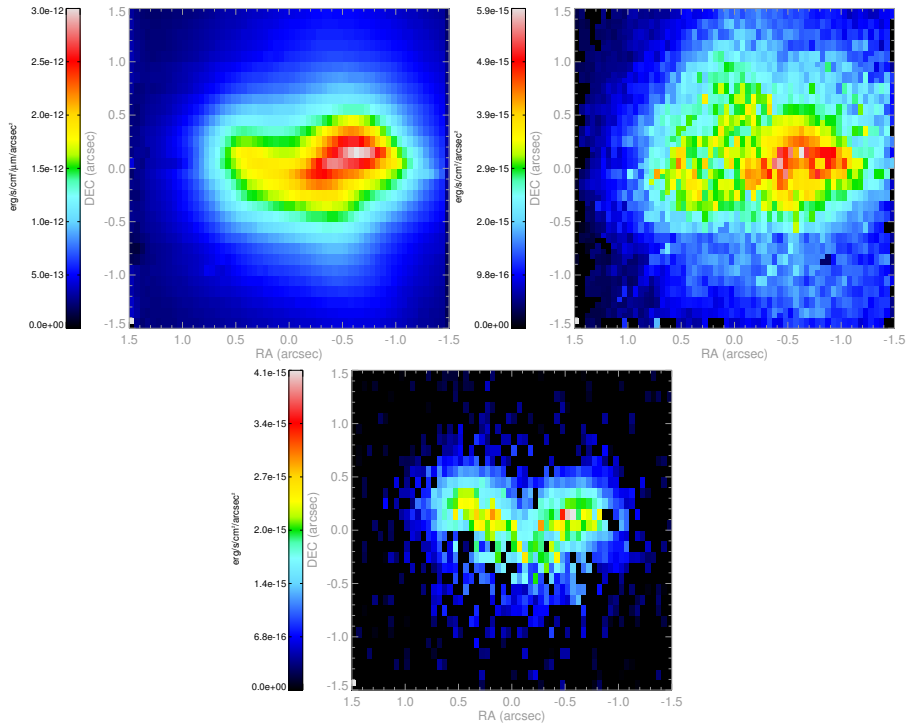


Figure 3.1 – SINFONI flux maps of K band continuum (left), H₂ 2.12 μm (middle) and Brγ 2.17 μm (right). The location (0,0) in these images is set to the pointing position of the observation, RA: 15h 34m 57.2s; DEC: +23d 30m 11.5s. East is left and north is up.

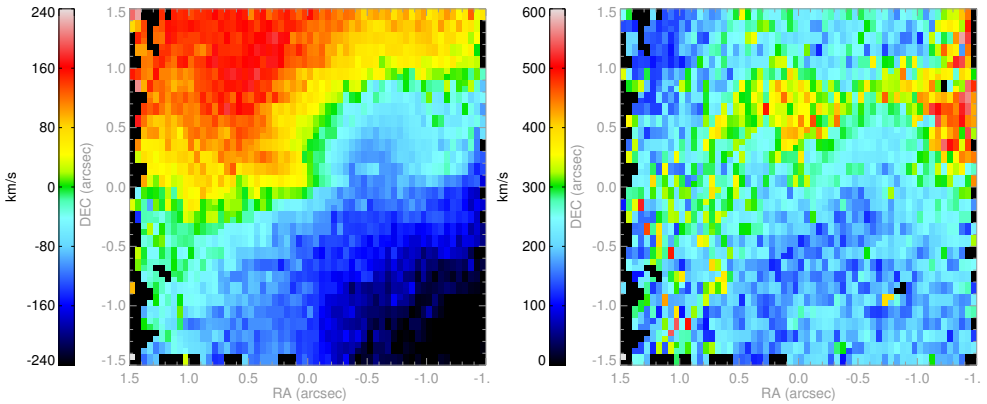


Figure 3.2 – H₂ velocity (left) and velocity dispersion (right). The systemic velocity has been set to 5434 km/s. The location (0,0) denotes the pointing position of observation, as in Fig. 3.1.

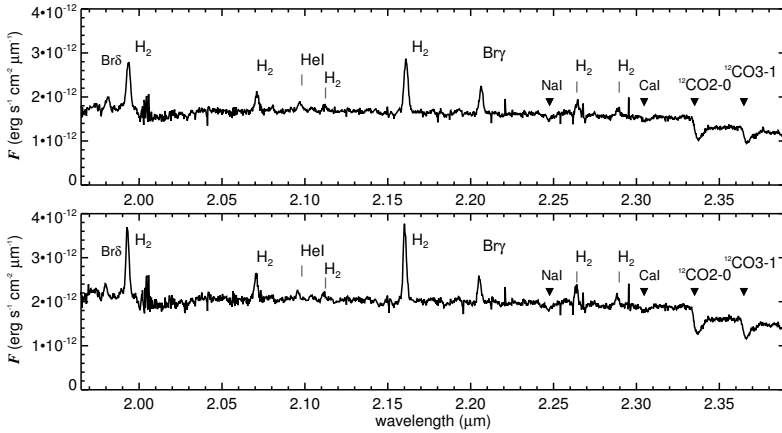


Figure 3.3 – Integrated K-band spectra of the east (left) and west (right) nucleus, from rectangular boxes of $1''.0 \times 1''.25$ centred on the nuclear positions. Central coordinates in Fig. 3.1 of east spectrum: $(0.3, 0.0)$; of west spectrum: $(-0.7, 0.05)$.

K-band continuum has a shape in which the original two nuclei are recognised. However, the right (western) peak clearly dominates the NIR continuum. The H_2 emission at $2.12 \mu\text{m}$ follows this shape and also peaks on the western nucleus, while the $Br\gamma$ line map shows equal contributions from both nuclei.

3.3.1 Spectra

The K-band spectra (Fig. 3.3) of the east and west nucleus are quite similar. Both spectra were integrated in a rectangular region of $1''.0 \times 1''.25$, centred on the nuclear positions: $(0.3, 0.0)$ for the east nucleus and $(-0.7, 0.05)$ for the west nucleus, using the coordinates of Fig. 3.1. The recombination lines $Br\gamma$, $Br\delta$ and $He I$ are comparable in strength in both nuclei. However, the level of the K-band continuum as well as the strength of the excited H_2 lines is higher in the west nucleus. Stellar absorption features of $Na I$ ($2.21 \mu\text{m}$), $Ca I$ ($2.26 \mu\text{m}$), and CO (^{12}CO 2–0 at $2.29 \mu\text{m}$ and ^{13}CO 2–0 at $2.34 \mu\text{m}$) are recognised in both, and these are slightly narrower in the western nucleus.

3.3.2 Gas kinematics

The H_2 ($2.12 \mu\text{m}$) velocity field is shown in the left frame of Fig. 3.2. The gas velocity field is dominated by large scale, almost regular rotation. Closer inspection reveals signatures associated with the two nuclei, which may reflect the local effect of the nuclear gravitational potentials, but these features are much weaker than the overall rotation. The H_2 velocity dispersion (Fig. 3.2, right) shows two relatively shallow peaks that are not directly related to the nuclei.

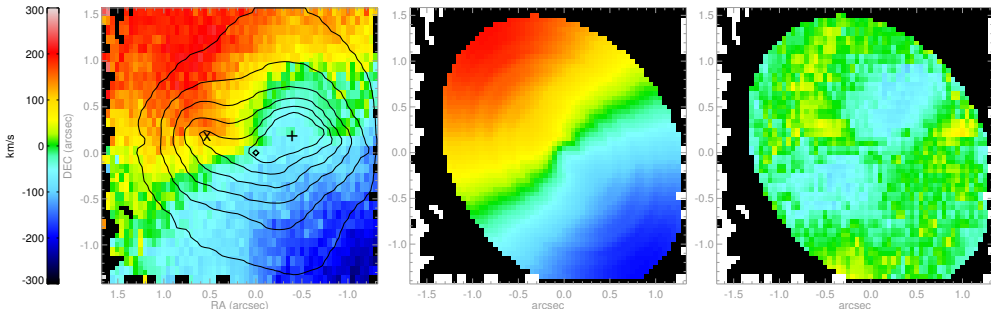


Figure 3.4 – Left: original H₂ velocity field (v_{orig}). X marks the location of the east nucleus, + marks the west nucleus and the diamond (\diamond) marks the kinematic centre of the Kinemetry-model. Centre: Circular H₂ velocity field (v_{circ}), resulting from the tilted ring model. Right: residual velocity field ($v_{\text{res}}=v_{\text{orig}}-v_{\text{circ}}$). All images have the same colour scale, and (0,0) is the location of the kinematic centre.

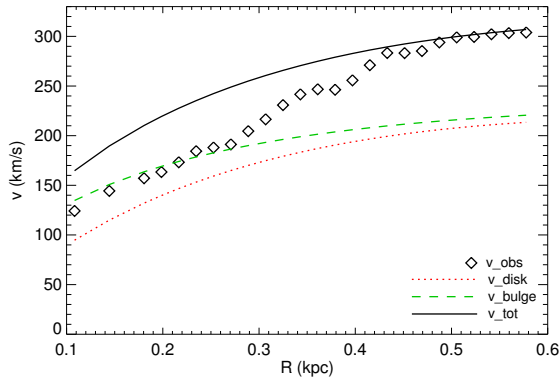


Figure 3.5 – Rotation curve of H₂, resulting from the tilted ring model fit described in the text, out to 0.6 kpc along the major axis. The open diamonds indicate the observed points, while fitted disk, bulge and total mass model are shown by the red dotted line, dashed green line and drawn black line respectively. The fit was constrained to reproduce the observed rotation curve at large radii.

The H₂ velocity field was fitted with a set of tilted rings, using the IDL-based code Kinemetry (Krajinović et al. 2006). The kinematic centre position was fixed at the centre of the outer K-band isophotes, which roughly corresponds to the point in between the maximum and minimum velocities. This location matches the kinematic centre in the CO velocity field of Downes & Solomon (1998). Tilted rings were fitted at increasing radii (r), with position angle (PA) as free parameter, and inclination (i) fixed to 40° , following the inclination of the CO-disk (Downes & Solomon 1998, Eckart & Downes 2001). Fig. 3.4 shows the original H₂ velocity field, now with (0,0) at the kinematic centre (left), the fitted circular velocity field (v_{circ} , middle) and the residual velocity field ($v_{\text{res}}=v_{\text{orig}}-v_{\text{circ}}$, right). The velocity field is dominated by the large scale rotation of a gas disk, instead of the rotation of the nuclei themselves, as opposed to for instance high resolution CO observations by Sakamoto et al.

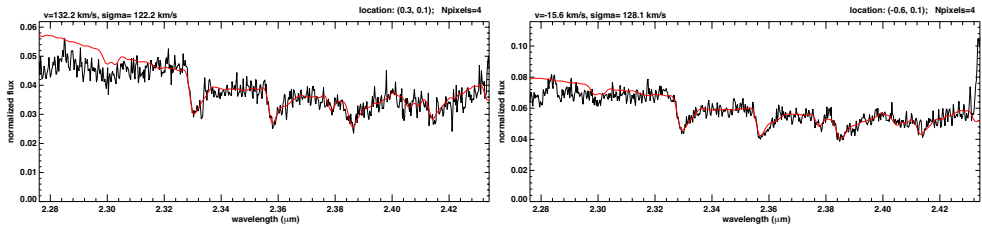


Figure 3.6 – Part of the K-band spectrum with absorption features (black), with the PPXF-fit with 6 template spectra overlaid (red). Left: east nucleus. Right: west nucleus. Note that the strong CO bands are well matched, as well as several other stellar absorption features.

(1999), who did find significant rotation of the nuclei separately in the CO gas. We do see some rotation that is associated with the nuclei in the residuals, but it is clear that its signature is unimportant compared to the large scale structure of the nuclear velocity field, which can be modelled as a simple rotating disk.

The central rotation curve of H_2 resulting from our tilted ring fit is shown in Fig. 3.5. The inner part rises linearly (solid body rotation), and bends at 0.5 kpc, although the point where the rotation curve will flatten cannot be exactly determined from these data. The PSF size is small compared to the scale of the rotation curve, so the slow rising of the curve is real and is not a result of beam smearing.

3.3.3 Stellar kinematics

The stellar absorption features of CO (^{12}CO 2-0 at $2.29\mu\text{m}$ and ^{12}CO 3-1 at $2.32\mu\text{m}$) were fitted with 6 stellar template spectra of different spectral types, which originated from SINFONI observations as well. For this fit we used Penalised Pixel Fitting (PPXF) from Cappellari & Emsellem (2004). Before the fitting, the spatial pixels were combined according to the Voronoi method, and in our case a S/N of 20 for each bin was sufficient for high quality fits in order to obtain a coherent stellar velocity field. Fitted spectra at the nuclear locations are shown in Fig 3.6. The resulting stellar velocity field and velocity dispersion field are shown in Fig. 3.7, left and right respectively. The (formal) errors in the fit of the velocity dispersion are typically 10-20 km/s in most of the bins, except the large bins in the outer parts where the error is larger.

3.3.4 Velocity profiles

Contrary to the situation with the gas, the stellar kinematics shows quite clearly the rotation of the two nuclei. The stellar velocity fields in the two nuclei actually match well the velocity fields derived from high resolution CO observations Sakamoto et al. (1999, 2008). Cuts in stellar velocity and velocity dispersion through the two nuclei are shown in Fig. 3.8. This figure also shows the velocity profiles of Br γ and H_2 in these same cuts. The cuts are centred on the infrared nuclei (pixels of maximum flux) and the position angles are chosen along

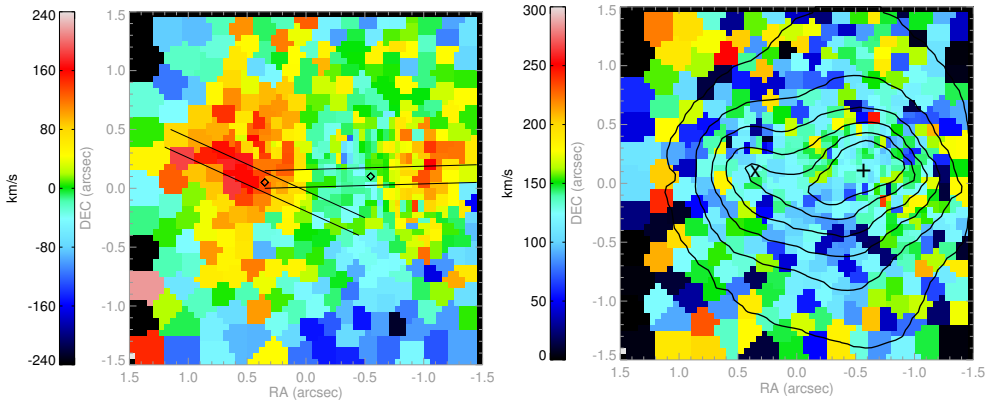


Figure 3.7 – Left: stellar velocity field, with profile cut positions. Right: stellar velocity dispersion, with K-band continuum contours.

highest stellar velocity gradient. The orientations of both cuts are shown in Fig. 3.7 (right). The velocity profiles of the Br γ and H₂ gas match quite well. The profiles of stellar velocity deviate from the gas, especially in the western nucleus, and these deviations are due to the fact that H₂ and Br γ trace the large-scale rotation at central gas disk, while the stellar kinematics is dominated by the two nuclei. This result also implies that a dominant part of the ionised gas (Br γ) is taking part in the dynamics of the large-scale gas disk, even though the Br γ flux distribution peaks at the positions of the two nuclei (Engel et al. 2011).

The rotation of the stellar system as a whole, outside the nuclear region, is slower than the rotation of the gas. Therefore, the stellar system must to a large extent be dynamically supported by random motions. The stellar velocity dispersion is essentially constant: no peak is seen in either of the nuclei, nor between the nuclei at the centre of the weaker isophotes, and the measured velocity dispersion is $\sigma_* = 130 \pm 10 \text{ km s}^{-1}$. This value is within the error bars compatible with the early value $\sigma_* = 151 \pm 25 \text{ km s}^{-1}$ measured by Doyon et al. (1994). A somewhat higher velocity dispersion $\sigma_* = 165 \pm 10 \text{ km s}^{-1}$ was found by Genzel et al. (2001) using single slits. The discrepancy with our data may arise from the uncertainties of separating rotation and random motions in single slit data. A much larger velocity dispersion of 275 to 300 km s^{-1} is found by Engel et al. (2011). This value is absolutely ruled out by our results, as can be seen easily from Fig. 3.6. We note however that the results by Engel et al. (2011) were obtained using the lower resolution $R \approx 1500 H+K$ grating of SINFONI. Their data therefore do not have sufficient spectral resolution for resolving the stellar kinematics, and we adopt here our own measurement $\sigma_* = 130 \pm 10 \text{ km s}^{-1}$ as the best measurement of the stellar velocity dispersion.

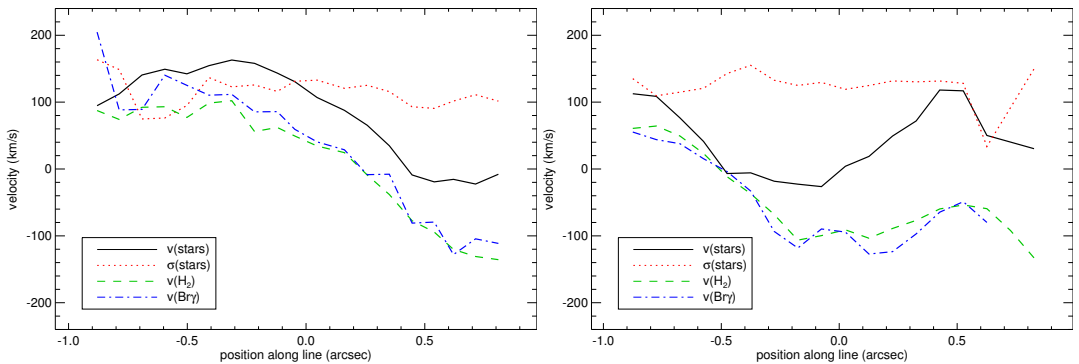


Figure 3.8 – Left: velocity profiles through the east nucleus. Right: velocity profiles through the west nucleus. Positions of the profile cuts are indicated in Fig. 3.7, right-hand panel.

3.4 Discussion: nuclear dynamics

In this section, we will first use the stellar dynamics to determine the mass of the near infrared nuclei. Then we will discuss the gas dynamics by taking the H_2 rotation curve (section 3.3.2) and use it to make a model of the mass. Consequently, we will discuss the importance of the gas and stellar components for the nuclear dynamics of Arp 220.

3.4.1 Mass estimate from stellar kinematics

For a non-rotating stellar system, the dynamical mass M_* can be calculated from the expression

$$\frac{M_*}{M_\odot} = 1.4 \cdot 10^6 \left(\frac{\sigma_*}{\text{km s}^{-1}} \right)^2 \frac{R_{\text{eff}}}{\text{kpc}}, \quad (3.1)$$

where σ_* is the stellar velocity dispersion and R_{eff} is the effective radius (i.e., the radius enclosing half the total light). This equation is an application of the general expression in Bender et al. (1992, their Eq. (3)), and the numerical factor in this equation depends on the adopted mass distribution. The factor $1.4 \cdot 10^6$ results from a constant M/L King model with $R_{\text{tidal}}/R_{\text{core}} = 50$, an appropriate choice of parameters for spheroids between a dwarf and a giant elliptical (Bender et al. 1992, see Appendix A of), following Tacconi et al. (2002) and Dasyra et al. (2006b). For a spherical system, this formula can be modified to include the effects of rotational support by adopting the expression

$$\frac{M_*}{M_\odot} = 4.7 \cdot 10^5 \left[3 \left(\frac{\sigma_*}{\text{km s}^{-1}} \right)^2 + \left(\frac{v_*}{\text{km s}^{-1}} \right)^2 \right] \frac{R_{\text{eff}}}{\text{kpc}}, \quad (3.2)$$

where v_* is the stellar rotational velocity at radius R_{eff} (Appendix B of Bender et al. 1992, Dasyra et al. 2006b).

For R_{eff} , Scoville et al. (2000) give 0.58 kpc for Arp 220 as a whole. Genzel et al. (2001) use this result to adopt values 0.6 ± 0.3 kpc for each of the two nuclei, but since the distance

between the nuclei is only 0.36 kpc, this approach is not tenable. While the nuclei do not show a peak in velocity dispersion, they do show considerable rotation, and the measured rotation velocity is $v_* = 90 \pm 10 \text{ km s}^{-1}$ for the eastern nucleus and $v_* = 70 \pm 10 \text{ km s}^{-1}$ for the western nucleus. The rotation patterns can be traced out to a radius of $\sim 0''.5$ (0.2 kpc) from the centre of each nucleus. The nuclei may actually be somewhat more extended, but beyond this radius their light is no longer dominant over the larger scale host galaxy. We therefore adopt the value $R_{\text{eff}} = 0.2 \pm 0.1 \text{ kpc}$ for each of the two nuclei. Since the stellar velocity fields match very well the velocity fields derived from high resolution CO data for the two nuclei Sakamoto et al. (1999, 2008), we can use the inclinations derived from the CO data. For the western nucleus, Engel et al. (2011) give $i \approx 50^\circ$ based on the CO data, where we estimate the error $\Delta i \approx 10^\circ$. For the eastern nucleus, Engel et al. (2011) could not derive an inclination from the CO data, so we follow these authors and adopt $i \approx 50 \pm 25^\circ$. The inclination-corrected stellar rotation velocities are then $90_{-10}^{+20} \text{ km s}^{-1}$ and $120_{-25}^{+100} \text{ km s}^{-1}$ for the western and eastern nucleus. The implied dynamical masses are $M_* = (5.7 \pm 3.0) \cdot 10^9 M_\odot$ for the western nucleus and $M_* = (6.0 \pm 3.0) \cdot 10^9 M_\odot$ for the eastern nucleus, within a 0.2 kpc radius for both. The total dynamical mass of the two nuclei is then $M_{*,\text{tot}} = (1.2 \pm 0.4) \cdot 10^{10} M_\odot$.

3.4.2 Mass estimate from gas kinematics

The H_2 rotation curve (Fig. 3.5) rises slowly, thus suggesting that there is no dominant central concentration in the distribution of stellar and gas mass. Only a mass concentration smaller than our PSF ($0.4''$ or 150 pc) could be hidden by beam smearing in our velocity field, but this would manifest itself as a peak in the gas velocity dispersion, which is not observed. Of course local mass concentrations do exist in the form of the two nuclei, but these have only subtle effects on the local H_2 velocity field. CO observations clearly reveal the nuclei in the molecular gas velocity field, and the absence of signatures of the nuclei in the present data is most likely due to significant nuclear extinction (see Sect. 3.4.3). The fact that these nuclei are separated by a significant distance, so that their mass is effectively spread over a much larger volume than the combined volumes of the nuclei themselves, may be responsible for the slowly rising rotation curve. We note that the flux distribution of H_2 is quite smooth, no clear peaks are observed so that there is no reason to assume a central concentration of gas, unless it is selectively extinguished. Nevertheless, these considerations show that it is difficult to model the inner part of the H_2 rotation curve accurately, in spite of its regular appearance. In order to model the mass distribution giving rise to the H_2 rotation curve we therefore focus on the outer parts of the rotation curve only, which is relatively insensitive to the precise distribution of mass close to the kinematic centre. In order to have sufficient freedom in our mass model we adopt a combination of a disk and bulge. The bulge has a Hernquist profile (Hernquist 1990) with characteristic radius $a = R_{\text{eff}}/(1 + \sqrt{2})$ and total mass M_{bulge} as free parameters. The disk parameters, scale length h and central surface brightness Σ_0 , are not entirely free but in combination satisfy the condition that the gas mass within the region is approximately $5 \cdot 10^9 M_\odot$ (Downes & Solomon 1998, Sakamoto et al. 2008). We imported the inclination corrected H_2 gas rotation curve into GIPSY (the Groningen Image Processing SYstem, van der Hulst et al. 1992, Vogelaar & Terlouw 2001) and used the procedure

ROTMAS. The resulting mass model, considering only the outer points of the rotation curve, is shown in Fig. 3.5. The resulting mass model consists of a disk with a mass, by construction, of $M_{\text{disk}} = 5 \cdot 10^9 M_{\odot}$ (with $\Sigma_0 = 1.3 \cdot 10^4 M_{\odot} \text{pc}^{-2}$ and $h = 0.35 \text{kpc}$) and a bulge with a mass $M_{\text{bulge}} = 7 \cdot 10^9 M_{\odot}$ ($R_{\text{eff}} = 2.5 \text{kpc}$) within the a radius of 0.59 kpc, the outermost point on the rotation curve. The total mass within this region is then $M_{\text{tot}} = (1.2 \pm 0.6) \cdot 10^{10} M_{\odot}$. Even when ignoring the gas mass condition, introducing a considerable freedom in how the total mass is apportioned between the model disk and model bulge, the total mass of the two is well determined (for instance, fitting only an exponential disk yields a result that is only 15% larger). Consequently, the error in the total mass is dominated by the uncertainty in the inclination of the disk, and this is the uncertainty quoted in our result. This mass determination, which considers radii out to 0.59 kpc is in excellent agreement with the mass determined for the two nuclei in Sect. 3.4, but there is sufficient error margin to include some additional mass for the host galaxy and the gas component. The mass of the gas disk in the nuclear region of Arp 220 of $5 \cdot 10^9 M_{\odot}$ (Downes & Solomon 1998, Sakamoto et al. 2008) therefore forms a significant part of the total dynamical mass.

3.4.3 Mass to light ratio

We calculate the total K -band luminosity within a radius of 0.6 kpc to be $L_K = 1.8 \cdot 10^{10} L_{K,\odot}$, where we have used a solar absolute K -band magnitude of 3.28. Without extinction correction, the value of M/L_K is then $0.6 \pm 0.3 M_{\odot}/L_{K,\odot}$. Since there is a good match between the flux distribution in Br γ and the K -band continuum, both can be extinction corrected using the ratio of hydrogen recombination lines and assuming the near-IR extinction curve of Martin & Whittet (1990). In the present case we use the pixel-by-pixel ratio of $F_{\text{Br}\gamma}/F_{\text{Br}\delta}$, which has an intrinsically constant value of 1.519 (Hummer & Storey 1987). The Br δ -line is detected with confidence over the whole nuclear region where we assume extinction is not negligible (e.g., Scoville et al. 2000). The extinction-corrected K -band luminosity in the same region is then $1.05 \cdot 10^{11} L_{K,\odot}$; in other words, 83% of the emitting K -band emission is absorbed, consistent with the analysis by Engel et al. (2011). In terms of an effective extinction integrated over the nuclei, we find $A_K = 1.9$ or $A_V = 17$, following Fitzpatrick (1999). The resulting extinction-corrected M/L_K is $0.11 \pm 0.5 M_{\odot}/L_{K,\odot}$, over an area of 6.1arcsec^2 or 0.82kpc^2 . Comparison with the synthetic starburst models of STARBURST99 (Leitherer et al. 1999, Vázquez & Leitherer 2005, Leitherer et al. 2010) shows that for an instantaneous burst of star formation, this M/L_K is reached at a time of about $1.8 \cdot 10^8$ years. In this model a power law stellar initial mass function (IMF) is used with a slope $\alpha = 2.35$ for stellar masses between 1 and $100 M_{\odot}$. Comparisons with starburst models should be viewed with some caution, since a significant fraction of the nuclear light may represent older stars from the bulges of the progenitor nuclei, and the M/L_K of the starburst component alone is in general hard to determine. However, evolved populations have significantly higher values than observed here (e.g., Vázquez & Leitherer 2005), and the present measurements thus at least indicate an important starburst contribution.

The extinction derived here for the central region is significant but not extreme, and this result is in agreement with earlier extinction determinations for the nuclei (e.g., Scoville et al.

1998, Engel et al. 2011). We derive maximum values of $A_V \sim 45$ in each of the nuclei. The central region of Arp 220 does harbour regions of very high column density (e.g., Scoville et al. 1991, Downes & Solomon 1998, Spoon et al. 2004, Sakamoto et al. 1999, Papadopoulos et al. 2010a,b), which could amount to $A_V \sim 1000$ if located in an absorbing foreground screen, and regions behind such a screen would be undetected in our data. In the context of this model, Scoville et al. (1998) have proposed that the nuclei are intersected by totally opaque gas disks, which would completely hide 50% of the nuclear emission from view. Adopting this additional correction would provide an intrinsic $M/L_K \sim 0.05$. In terms of the starburst model referred to above, the implied age would then be 6×10^7 years. Clearly the quality of these estimates are very sensitive to the extent to which the extinction can be reliably corrected.

3.5 Conclusions

We have obtained high resolution near-IR K -band integral field spectroscopy of the nearby ULIRG Arp 220. The data provide a detailed view of the nuclear stellar and nebular emission and extinction, as well as of the velocity and velocity dispersion fields of both gas and stars. These independent velocity fields provide independent probes of the nuclear dynamical mass. We obtain the following results:

1. While the stellar emission and also the Br γ nebular emission reveal the two remnant nuclei, the H₂ emission reveals an extended disk, with little evidence of influence from the two nuclei.
2. The velocity field of the H₂ emission reveals a regularly rotating disk, with minor velocity distortions at the positions of the two nuclei.
3. In contrast, the stellar velocity field shows prominent rotation of the two nuclei, while little rotation is observed in the larger scale host galaxy. The two nuclei counter-rotate with respect to each other, but their rotation patterns agree with that derived from high resolution CO observations. The stellar velocity dispersion field does not reveal any prominent peaks.
4. Analysis of the nuclear stellar kinematics gives a total dynamical mass of $M_{*,\text{tot}} = (1.2 \pm 0.4) \cdot 10^{10} M_\odot$ for the two nuclei together, where the error is dominated by the uncertainty in the effective radii.
5. The H₂ velocity field provides a dynamical mass within a radius of 0.6 kpc of $M_{\text{tot}} = (1.2 \pm 0.6) \cdot 10^{10} M_\odot$, where the uncertainty is dominated by the uncertainty in the disk's inclination. The determinations from gas dynamics and stellar dynamics are in excellent agreement.
6. The molecular gas, with a mass of $5 \times 10^9 M_\odot$ constitutes a significant fraction of the dynamical mass.

7. The K -band stellar mass to light ratio, corrected for extinction and is $M/L_K \sim 0.05$, with at least a factor of two uncertainty resulting from the uncertainty in the extinction correction. Even taking these uncertainties into account, this value indicates an important starburst contribution to the nuclear K -band emission.

These results illustrate the power of high resolution near-IR integral field spectroscopy for analysing the nuclear starburst and the dynamical properties of the nuclear regions of ULIRGs in general.

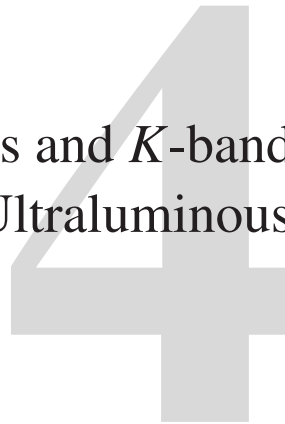
References

- Aalto, S., Wilner, D., Spaans, M., et al. 2009, *A&A*, 493, 481
- Anantharamaiah, K. R., Viallefond, F., Mohan, N. R., Goss, W. M., & Zhao, J. H. 2000, *ApJ*, 537, 613
- Araya, E., Baan, W. A., & Hofner, P. 2004, *ApJS*, 154, 541
- Armus, L., Charmandaris, V., Bernard-Salas, J., et al. 2007, *ApJ*, 656, 148
- Armus, L., Neugebauer, G., Soifer, B. T., & Matthews, K. 1995a, *AJ*, 110, 2610
- Armus, L., Shupe, D. L., Matthews, K., Soifer, B. T., & Neugebauer, G. 1995b, *ApJ*, 440, 200
- Arribas, S., Colina, L., & Clements, D. 2001, *ApJ*, 560, 160
- Baan, W. A., Guesten, R., & Haschick, A. D. 1986, *ApJ*, 305, 830
- Baan, W. A. & Haschick, A. D. 1995, *ApJ*, 454, 745
- Baan, W. A., Haschick, A. D., & Uglesich, R. 1993, *ApJ*, 415, 140
- Baan, W. A., Wood, P. A. D., & Haschick, A. D. 1982, *ApJ*, 260, L49
- Bender, R., Burstein, D., & Faber, S. M. 1992, *ApJ*, 399, 462
- Bonnet, H., Abuter, R., Baker, A., et al. 2004, *The Messenger*, 117, 17
- Cappellari, M. & Emsellem, E. 2004, *PASP*, 116, 138
- Cappellari, M., Neumayer, N., Reunanen, J., et al. 2009, *MNRAS*, 394, 660
- Clements, D. L., McDowell, J. C., Shaked, S., et al. 2002, *ApJ*, 581, 974
- Colina, L., Arribas, S., & Clements, D. 2004, *ApJ*, 602, 181
- Dasyra, K. M., Tacconi, L. J., Davies, R. I., et al. 2006a, *ApJ*, 638, 745
- Dasyra, K. M., Tacconi, L. J., Davies, R. I., et al. 2006b, *ApJ*, 651, 835
- Dermer, C. D., Bland-Hawthorn, J., Chiang, J., & McNaron-Brown, K. 1997, *ApJ*, 484, L121+
- Downes, D. & Eckart, A. 2007, *A&A*, 468, L57
- Downes, D. & Solomon, P. M. 1998, *ApJ*, 507, 615
- Doyon, R., Wells, M., Wright, G. S., et al. 1994, *ApJ*, 437, L23
- Eckart, A. & Downes, D. 2001, *ApJ*, 551, 730
- Eisenhauer, F., Abuter, R., Bickert, K., et al. 2003, in Presented at the Society of Photo-Optical Instrumentation Engineers (SPIE) Conference, Vol. 4841, Society of Photo-Optical Instrumentation Engineers (SPIE) Conference Series, ed. M. Iye & A. F. M. Moorwood, 1548–1561
- Engel, H., Davies, R. I., Genzel, R., et al. 2011, *ApJ*, 729, 58
- Farrah, D., Bernard-Salas, J., Spoon, H. W. W., et al. 2007, *ApJ*, 667, 149
- Fitzpatrick, E. L. 1999, *PASP*, 111, 63
- Genzel, R., Lutz, D., Sturm, E., et al. 1998, *ApJ*, 498, 579
- Genzel, R., Tacconi, L. J., Rigopoulou, D., Lutz, D., & Tecza, M. 2001, *ApJ*, 563, 527
- Goldader, J. D., Joseph, R. D., Doyon, R., & Sanders, D. B. 1995, *ApJ*, 444, 97
- Graham, J. R., Carico, D. P., Matthews, K., et al. 1990, *ApJ*, 354, L5
- Greve, T. R., Papadopoulos, P. P., Gao, Y., & Radford, S. J. E. 2009, *ApJ*, 692, 1432
- Heckman, T. M., Armus, L., & Miley, G. K. 1987, *AJ*, 93, 276
- Heckman, T. M., Dahlem, M., Eales, S. A., Fabbiano, G., & Weaver, K. 1996, *ApJ*, 457, 616

- Hernquist, L. 1990, *ApJ*, 356, 359
- Hummer, D. G. & Storey, P. J. 1987, *MNRAS*, 224, 801
- Imanishi, M. & Dudley, C. C. 2000, *ApJ*, 545, 701
- Imanishi, M., Dudley, C. C., Maiolino, R., et al. 2007, *ApJS*, 171, 72
- Imanishi, M., Dudley, C. C., & Maloney, P. R. 2006, *ApJ*, 637, 114
- Iwasawa, K., Matt, G., Guainazzi, M., & Fabian, A. C. 2001, *MNRAS*, 326, 894
- Iwasawa, K., Sanders, D. B., Evans, A. S., et al. 2005, *MNRAS*, 357, 565
- Joseph, R. D. & Wright, G. S. 1985, *MNRAS*, 214, 87
- Krajinović, D., Cappellari, M., de Zeeuw, P. T., & Copin, Y. 2006, *MNRAS*, 366, 787
- Larkin, J. E., Armus, L., Knop, R. A., Matthews, K., & Soifer, B. T. 1995, *ApJ*, 452, 599
- Leitherer, C., Ortiz Otlávaro, P. A., Bresolin, F., et al. 2010, *ApJS*, 189, 309
- Leitherer, C., Schaerer, D., Goldader, J. D., et al. 1999, *ApJS*, 123, 3
- Lonsdale, C. J., Diamond, P. J., Thrall, H., Smith, H. E., & Lonsdale, C. J. 2006, *ApJ*, 647, 185
- Lonsdale, C. J., Lonsdale, C. J., Diamond, P. J., & Smith, H. E. 1998, *ApJ*, 493, L13
- Martin, P. G. & Whittet, D. C. B. 1990, *ApJ*, 357, 113
- Matsushita, S., Iono, D., Petitpas, G. R., et al. 2009, *ApJ*, 693, 56
- McDowell, J. C., Clements, D. L., Lamb, S. A., et al. 2003, *ApJ*, 591, 154
- Mundell, C. G., Ferruit, P., & Pedlar, A. 2001, *ApJ*, 560, 168
- Neumayer, N., Cappellari, M., Reunanen, J., et al. 2007, *ApJ*, 671, 1329
- Norris, R. P. 1988, *MNRAS*, 230, 345
- Papadopoulos, P. P., Isaak, K., & van der Werf, P. 2010a, *ApJ*, 711, 757
- Papadopoulos, P. P., van der Werf, P., Isaak, K., & Xilouris, E. M. 2010b, *ApJ*, 715, 775
- Parra, R., Conway, J. E., Diamond, P. J., et al. 2007, *ApJ*, 659, 314
- Rieke, G. H., Cutri, R. M., Black, J. H., et al. 1985, *ApJ*, 290, 116
- Risaliti, G., Imanishi, M., & Sani, E. 2010, *MNRAS*, 401, 197
- Rodríguez-Rico, C. A., Goss, W. M., Viallefond, F., et al. 2005, *ApJ*, 633, 198
- Rodríguez Zaurín, J., Tadhunter, C. N., & González Delgado, R. M. 2008, *MNRAS*, 384, 875
- Rovilos, E., Diamond, P. J., Lonsdale, C. J., Lonsdale, C. J., & Smith, H. E. 2003, *MNRAS*, 342, 373
- Rovilos, E., Diamond, P. J., Lonsdale, C. J., Smith, H. E., & Lonsdale, C. J. 2005, *MNRAS*, 359, 827
- Sakamoto, K., Scoville, N. Z., Yun, M. S., et al. 1999, *ApJ*, 514, 68
- Sakamoto, K., Wang, J., Wiedner, M. C., et al. 2008, *ApJ*, 684, 957
- Sanders, D. B., Mazzarella, J. M., Kim, D.-C., Surace, J. A., & Soifer, B. T. 2003, *AJ*, 126, 1607
- Scoville, N. Z., Evans, A. S., Dinshaw, N., et al. 1998, *ApJ*, 492, L107+
- Scoville, N. Z., Evans, A. S., Thompson, R., et al. 2000, *AJ*, 119, 991
- Scoville, N. Z., Sargent, A. I., Sanders, D. B., & Soifer, B. T. 1991, *ApJ*, 366, L5
- Scoville, N. Z., Yun, M. S., & Bryant, P. M. 1997, *ApJ*, 484, 702
- Shaya, E. J., Dowling, D. M., Currie, D. G., Faber, S. M., & Groth, E. J. 1994, *AJ*, 107, 1675
- Shioya, Y., Taniguchi, Y., & Trentham, N. 2001a, *MNRAS*, 321, 11
- Shioya, Y., Trentham, N., & Taniguchi, Y. 2001b, *ApJ*, 548, L29
- Smith, H. E., Lonsdale, C. J., Lonsdale, C. J., & Diamond, P. J. 1998, *ApJ*, 493, L17
- Soifer, B. T., Neugebauer, G., Helou, G., et al. 1984, *ApJ*, 283, L1
- Soifer, B. T., Neugebauer, G., Matthews, K., et al. 1999, *ApJ*, 513, 207
- Solomon, P. M., Radford, S. J. E., & Downes, D. 1990, *ApJ*, 348, L53
- Spoon, H. W. W., Marshall, J. A., Houck, J. R., et al. 2007, *ApJ*, 654, L49
- Spoon, H. W. W., Moorwood, A. F. M., Lutz, D., et al. 2004, *A&A*, 414, 873
- Tacconi, L. J., Genzel, R., Lutz, D., et al. 2002, *ApJ*, 580, 73
- van der Hulst, J. M., Terlouw, J. P., Begeman, K. G., Zwitter, W., & Roelfsema, P. R. 1992, in *Astronomical Society of the Pacific Conference Series*, Vol. 25, *Astronomical Data Analysis Software and Systems I*, ed. D. M. Worrall, C. Biemesderfer, & J. Barnes, 131–+

- van der Werf, P. P. 2001, in *Starburst galaxies: near and far*, 151
- Vázquez, G. A. & Leitherer, C. 2005, *ApJ*, 621, 695
- Vogelaar, M. G. R. & Terlouw, J. P. 2001, in *Astronomical Society of the Pacific Conference Series*, Vol. 238, *Astronomical Data Analysis Software and Systems X*, ed. F. R. Harnden Jr., F. A. Primini, & H. E. Payne, 358–4
- Wilson, C. D., Harris, W. E., Longden, R., & Scoville, N. Z. 2006, *ApJ*, 641, 763
- Zhao, J.-H., Anantharamaiah, K. R., Goss, W. M., & Viallefond, F. 1996, *ApJ*, 472, 54

Nuclear stellar dynamics and *K*-band mass-to-light ratios of Ultraluminous Infrared Galaxies



L. Vermaas and P. P. van der Werf

Abstract

We present high resolution K -band integral field spectroscopy of a small sample of nearby ultraluminous infrared galaxies (ULIRGs), and use the CO bandhead data to derive the kinematics of the stellar components in these systems. Dynamical masses are derived, considering both the rotation and velocity dispersion of the stellar components. These masses are combined with the extinction-corrected K -band luminosities to derive K -band stellar mass to light ratios. We discuss the main uncertainties in our analysis which are dominated by the inclination angle of the rotating stellar system and the measurement of the effective radius. Our results show M/L_K values which are lower (and in several cases much lower) than those of evolved elliptical galaxies, and this reflects the lower age of the K -band stellar population. Given that M/L_K correlates with starburst age, we look at evolutionary trends with M/L_K , but find none. We conclude that M/L_K measures the age of the most recent starburst in the system, which cannot easily be related to the evolutionary stage of the system. Finally, we suggest a way to use M/L_K in the analysis of the starbursts ULIRGs, where it has the advantage that it does not depend on photoionization models, which are known to fail in ULIRGs due to the preponderance of (ultra)compact HII regions.

4.1 Introduction

Ultraluminous infrared galaxies (ULIRGs) are spectacular systems with infrared luminosities $L_{\text{IR}} \geq 10^{12} L_{\odot}$. Nearly all are strongly interacting merger systems with a large amount of molecular gas, while most of the interstellar matter is concentrated in the inner regions of these objects, with extreme nuclear starbursts. The energy source is a combination of starburst and an active galactic nucleus (AGN), in varying proportion, as derived from spectroscopy and imaging at wavelengths from radio to X-rays. ULIRGs have a range in infrared spectral energy distributions, which is often expressed in the ratio of flux in the $25 \mu\text{m}$ and the $60 \mu\text{m}$ bands: “cool” ULIRGs have a typical ratio $f_{25}/f_{60} \leq 0.10$, whereas for “warm” ULIRGs $f_{25}/f_{60} > 0.2$. Warm ULIRGs have compact, bright nuclei compared to cool ULIRGs.

The AGN-starburst connection has become a central issue with the discovery of the relation between stellar velocity dispersion and mass of the central black hole in spheroidal stellar systems (Magorrian et al. 1998, Ferrarese & Merritt 2000, Gebhardt et al. 2000). Given that elliptical galaxies are mainly old, this relation has to be put in place at their formation history. Since ULIRGs form stars at prodigious rates, $10^2 - 10^3 M_{\odot} \text{yr}^{-1}$, and often host an AGN as well, they may be regarded as local analogs to forming spheroids. These points have been emphasised in extensive studies by Genzel et al. (2001) and Tacconi et al. (2002). While these studies indicate that local ULIRGs evolve into intermediate mass rather than giant ellipticals, they are still the best available local laboratories for studying the processes occurring in more luminous high- z objects such as the sub-mm galaxies, which may be the sites of the coeval explosive buildup of stellar mass and a supermassive black hole.

A conceptually simple mechanism for establishing a relation between stellar mass and black hole mass is based on feedback from the AGN terminating star formation. Sanders et al. (1988) argue that ULIRGs are dust-obscured precursors of QSOs. On this evolutionary path, the AGN disperses the dust and gas, shifting the bulk of energy toward shorter wavelengths, eventually becoming an optically bright QSO. In the context of the coeval buildup of stellar mass and black hole mass, the dispersal of dust and gas would also terminate star formation, and thus provides a possible mechanism for establishing a relation between black hole mass and stellar mass: once the black hole becomes so massive that its feedback on the environment disperses the gas, it shuts down star formation and the stellar mass is fixed. The dispersal of the gas also limits further growth of the black hole. The stellar mass is then given by the integral of star formation over time during the ULIRG phase, the black hole mass by the integral of accretion rate over time.

If ULIRGs indeed evolve into elliptical galaxies, they should also show the characteristic scaling relations of elliptical galaxies, in particular the so-called Fundamental Plane (FP), which relates the effective radius R_{eff} , the average surface brightness within R_{eff} , and the central velocity dispersion of an elliptical galaxy. On the other hand, the location of a galaxy with respect to the FP depends on its mass to light ratio (M/L), and an important evolving young stellar population will have a different M/L than a quiescent elliptical galaxy. In this paper we therefore focus on the M/L ratio of ULIRGs as derived from our near-infrared integral field spectroscopic, AO-assisted data from SINFONI of a sample ULIRGs/QSOs. The data allow us to constrain the gravitational potential of the nuclear region as derived

Table 4.1 – Observed sources

Name	z	$\log(L_{\text{ir}}/L_{\odot})$	f_{25}/f_{60}	kpc''
IRAS 01388-4618 ^a	0.090289	12.03	0.12	1.79
IRAS F05189-2524	0.042563	12.09	0.26	0.84
IRAS F09111-1007	0.054141	11.95	0.11	1.07
IRAS F17208-0014	0.042810	12.33	0.05	0.86
IRAS F20551-4250	0.042996	11.98	0.15	0.86
Arp 220 ^a	0.018126		0.06	0.36

^a No new data is presented for these sources, they are included for comparison.

from the modelling of the observed profile of the stellar CO absorption features in these objects. The dynamical properties of the nuclear gas disks, determined from the same data, is described in Chapter 5 of this thesis.

4.2 Observations and data reduction

Six objects were selected from the IRAS Revised Bright Galaxy Sample (Sanders et al. 2003), for gas kinematics as well as for stellar kinematics. These datasets provide measurements of gas kinematics and stellar kinematics in the same dataset, but in this chapter we focus on only the stellar kinematics, and describe the gas kinematics separately in Chapter 5. For qualification as an ULIRG, $L_{\text{ir}} \geq 10^{12}$. The redshift criterion was $z \leq 0.12$, in order to have enough spatial resolution and to be able to detect stellar CO-bandheads. The sample spans a range in infrared colours, in order to have a “sequence” from cool to warm ULIRGs (QSOs), albeit with very limited statistics. The infrared colour is determined by the ratio of flux in the $25\mu\text{m}$ band and the $60\mu\text{m}$ band (f_{25}/f_{60} ; < 0.2 qualifies as ‘cool’ and > 0.2 qualifies as ‘warm’). While we observed 6 targets (Table 4.1), the CO bandheads were detected in only 5 of these, including Arp 220, which has been discussed in Chapter 3.

The objects were observed with SINFONI, the Spectrograph for INtegral Field Observations in the Near Infrared ($1.1 - 2.45\mu\text{m}$), which is installed on UT4 of the VLT (Eisenhauer et al. 2003, Bonnet et al. 2004), with the Laser Guide Star facility was used for Adaptive Optics. Since no nearby bright field stars were available, tip-tilt correction was done on the optical nucleus of the objects. The intermediate platescale was used, with a field of view of $3'' \times 3''$ onto 64×64 spatial pixels. Each of these pixels is projected onto 2218 spectral elements in the K-band, with a central wavelength of $2.2\mu\text{m}$. This results in spatial pixels with a resolution of $0.05'' \times 0.10''$, and a spectral resolution $\lambda/\Delta\lambda$ of 4000.

For the pointings, an ABA'-nodding mode was used, i.e. object-sky-object with equal integration times of 900 s, with the A' frame slightly shifted with respect to the A frame. The total (on-source) integration time was 6×900 s, or 75 minutes in most cases. The observations

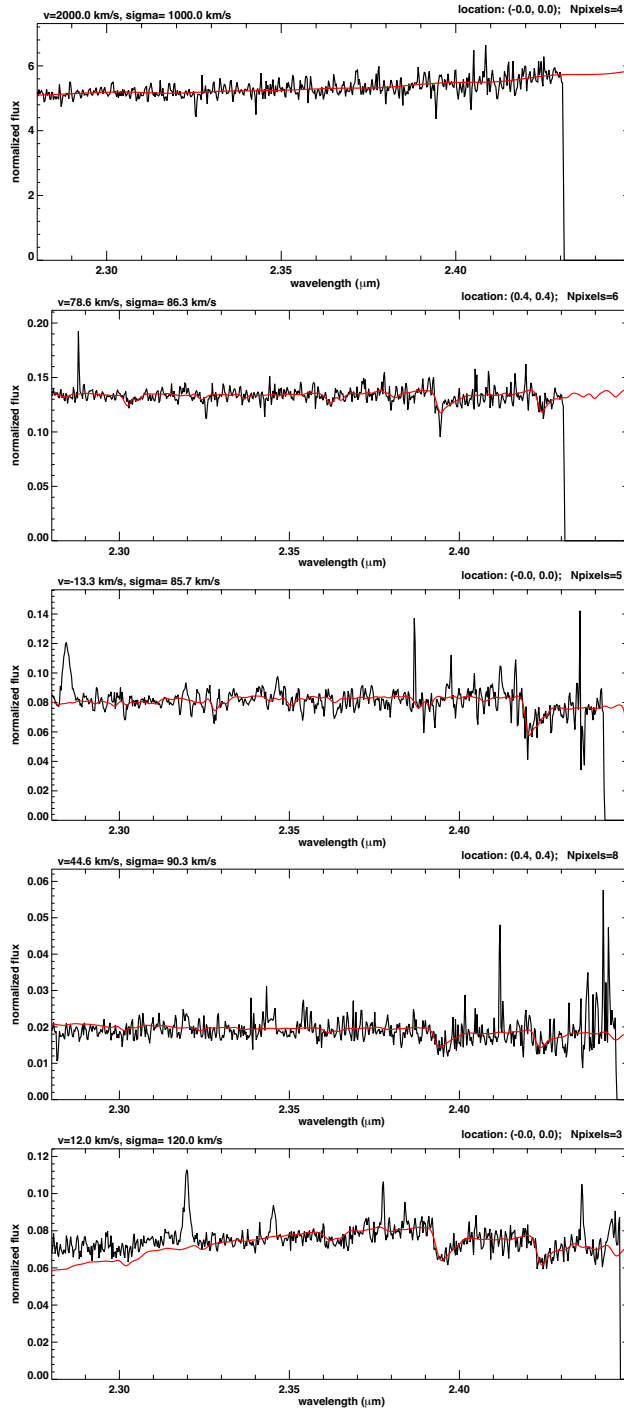


Figure 4.1 – Part of the K-band spectrum (black), with overplotted the PPXF-fit with 3-6 template spectra overplotted (red). Top to bottom: IRAS 05189-2524 nucleus, IRAS 05189-2524 outer location; IRAS 09111-1007 nucleus; IRAS 17208-0014 nucleus; IRAS 20551-4250 nucleus.

of IRAS 05189-2524 and IRAS 09111-1007 were carried out on December 29 and 30, 2007, with average seeing of $0.8''$. The observations of IRAS 17208-0014 and IRAS 20551-4250 were carried out on July 18 and 19 of 2009 with an average seeing of $0.7''$. Achieved Strehl ratios were of the order of 0.20-0.30.

The data were reduced with the SINFONI pipeline, which was developed by ESO and the Max-Planck-Institut für extraterrestrische Physik. The default procedure included corrections for pixel non-linearity, distortion and wavelength calibration.

For both flux calibration and telluric feature removal, a standard star was observed with the same setup as was used for the science frames, typically an early type star containing few stellar lines in the NAIR. After reduction, the average stellar spectrum was extracted and the stellar lines were removed ($\text{Br}\gamma$). Finally, each spectrum of the object frame was divided by this extracted spectrum.

In the case of IRAS 05189-2524 and IRAS 09111-1007, a PSF of $0.24''$ was determined from the [SiVI] line map of IRAS 09111-1007, which is assumed to originate from a point-source. For IRAS 17208-0014 and IRAS 20551-4250, the PSF-size was determined from observations of QSO Mrk 1014, in the same night, with the same instrumental setup and was measured to be $0.2''$.

4.3 Results and analysis

In this paper, we focus on the stellar dynamics, while the gas morphology (H_2 $2.12\mu\text{m}$ and $\text{Pa}\alpha$) and kinematics are analysed and *K*-band spectra are presented in Chapter 5. In all of these objects, stellar absorption features of CO (^{12}CO 2-0 at $2.29\mu\text{m}$ and in some cases ^{12}CO 3-1 at $2.32\mu\text{m}$) were detected (if not redshifted out of the *K*-band range).

4.3.1 Method

Deriving stellar kinematics

In order to derive stellar kinematics we followed the procedure described in Chapter 3. The parts of the *K* band nuclear spectra where the strongest CO-absorption features are present, were fitted with 6 stellar template spectra of different types, which originated from SINFONI observations as well. The Penalised Pixel Fitting (PPXF) from Cappellari & Emsellem (2004) was used for the fitting process. Before the fitting, the spatial pixels were combined according to the Voronoi method, and in our case a S/N of 20 for each bin was sufficient for high quality fits in order to obtain a coherent stellar velocity field. Fitted and measured spectra at the nuclear locations are shown in Fig. 4.1. Figure 4.2 shows for each galaxy the *K*-band continuum map, while Fig. 4.3 shows the resulting stellar velocity field (v_*) and the stellar velocity dispersion field (σ_*).

Dynamical mass estimate from σ_* and v_*

The dynamical mass M_{dyn} can be calculated from the stellar velocity dispersion, using

$$\frac{M_{\text{dyn}}}{M_{\odot}} = 1.4 \cdot 10^6 \left(\frac{\sigma_*}{\text{km s}^{-1}} \right)^2 \frac{R_{\text{eff}}}{\text{kpc}}, \quad (4.1)$$

where R_{eff} is the effective (half light) radius. This is an application of the general formula in Bender et al. (1992, Eq. 3), where the factor of $1.4 \cdot 10^6$ results from a constant M/L King model with $R_{\text{tidal}}/R_{\text{core}} = 50$: between a dwarf and a giant elliptical (Bender et al. 1992, Appendix A). For a spherical system with significant rotational support, this formula can be modified to the expression

$$\frac{M_{\text{dyn}}}{M_{\odot}} = 4.7 \cdot 10^5 \left[3 \left(\frac{\sigma_*}{\text{km s}^{-1}} \right)^2 + \left(\frac{v_*}{\text{km s}^{-1}} \right)^2 \right] \frac{R_{\text{eff}}}{\text{kpc}}, \quad (4.2)$$

where v_* is the stellar velocity measured at R_{eff} (Appendix B of Bender et al. 1992, Dasyra et al. 2006, Davies et al. 2007).

The dynamical mass within a radius R_{out} is calculated assuming a Hernquist potential, which has the analytical property $M(r) = M_{\text{tot}} \frac{r^2}{(r+a)^2}$, where a is related to the half-mass radius $r_{1/2}$ by $r_{1/2} = (1 + \sqrt{2})a$ (Hernquist 1990). The mass within this radius, i.e. our field of view, can now be compared to the K -band luminosity in the same region.

Our calculation is quite sensitive to the value of R_{eff} , the radius enclosing half the total light. Determinations of R_{eff} for ULIRGs are however strongly compromised by the large amounts of nuclear extinction. Since the extinction is typically highest at the nuclei, where the intrinsic surface brightness is highest, values of R_{eff} will be overestimated if nuclear extinction plays a role. In principle, an accurate extinction correction should be able to alleviate this problem, but accurate extinction corrections are challenging for these highly obscured systems. The fact that published values of R_{eff} (even from extinction corrected data) for the same ULIRG often depend on the observing wavelength illustrates the severity of this problem. Therefore, in stead of attempting to derive R_{eff} from an extinction corrected image, we circumvent the problem by noting that if M/L does not vary with radius, R_{eff} should equal the radius enclosing half of the total mass. We then use dynamically determined values of R_{eff} , derived from the nuclear gas dynamics discussed in Chapter 5. The reader is referred to that chapter for further discussion.

The dynamical masses are also dependent on the presence of rotational dynamical support, and indeed rotation of the stellar component is observed in several of our targets. The importance of rotational support for the derived dynamical mass then depends on the assumed inclination of the rotational pattern. Our data are not sufficiently accurate that the inclination can be determined from the data themselves and we therefore assume the rotation of the stellar body to have the same inclination as the gas disks, as described in Chapter 5. Table 4.2 has a column v_*/σ_* which shows values both uncorrected and corrected for inclination. The resulting dynamical masses (including the inclination correction) are listed in the same table.

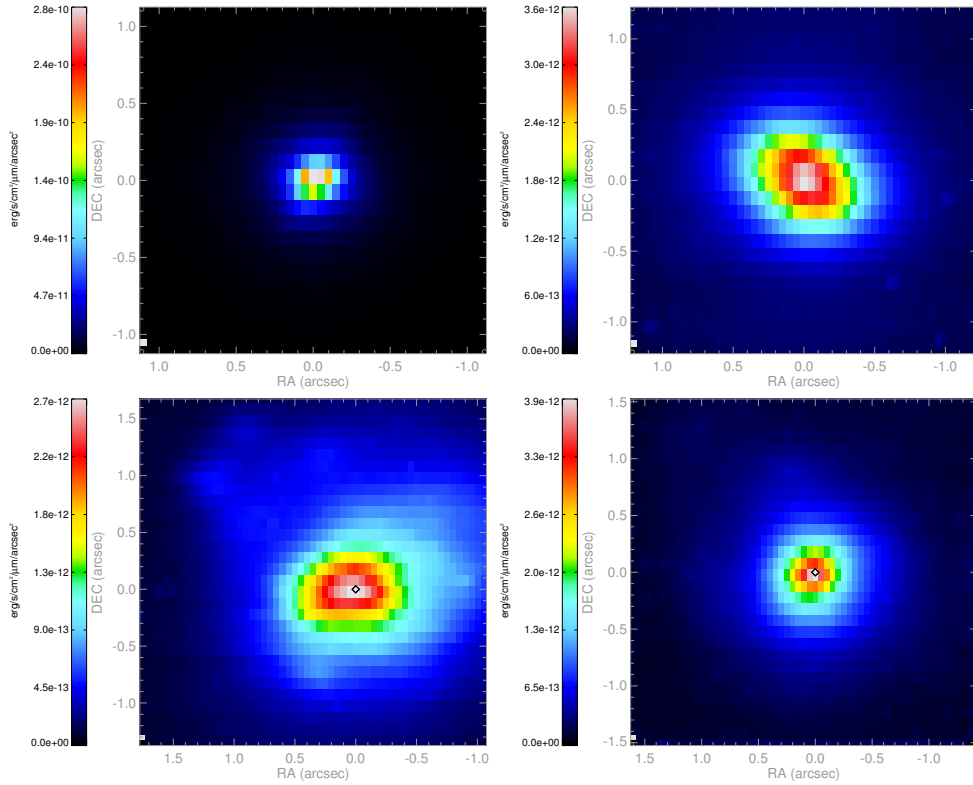


Figure 4.2 – K -band continuum; top left: IRAS 05189-2524; top right: IRAS 09111-1007; bottom left: IRAS 17208-0014; bottom right: IRAS 20551-4250.

K -band luminosity and extinction

In all cases except IRAS 05189-2524 (see below, Sect. 4.3.3), the K -band luminosity (L_K) was determined and extinction corrected from a pixel-to-pixel derived extinction map from the line ratio $\text{Pa } \alpha/\text{Br } \gamma$, which has an intrinsic ratio of 12.07 (Hummer & Storey 1987). In regions where no reliable extinction measurement could be made, a value of $A_K=0.7$ was used, following Tacconi et al. (2002). The values of L_K (uncorrected and corrected for extinction) and M_{dyn}/L_K , calculated for the extinction-corrected values of L_K are stated in Table 4.3.

4.3.2 IRAS 01388-4618

With f_{25}/f_{60} of 0.12, this is a “medium” ULIRG in the sample. This is the object where we could not measure the CO bands, due to the high redshift of 0.09. However, since we did measure its gas dynamics, we do include it in our sample and for the stellar kinematics we adopt ($v_* = 130 \pm 15$, $\sigma_* = 144 \pm 10$) km/s from Genzel et al. (2001). The K -band luminosity

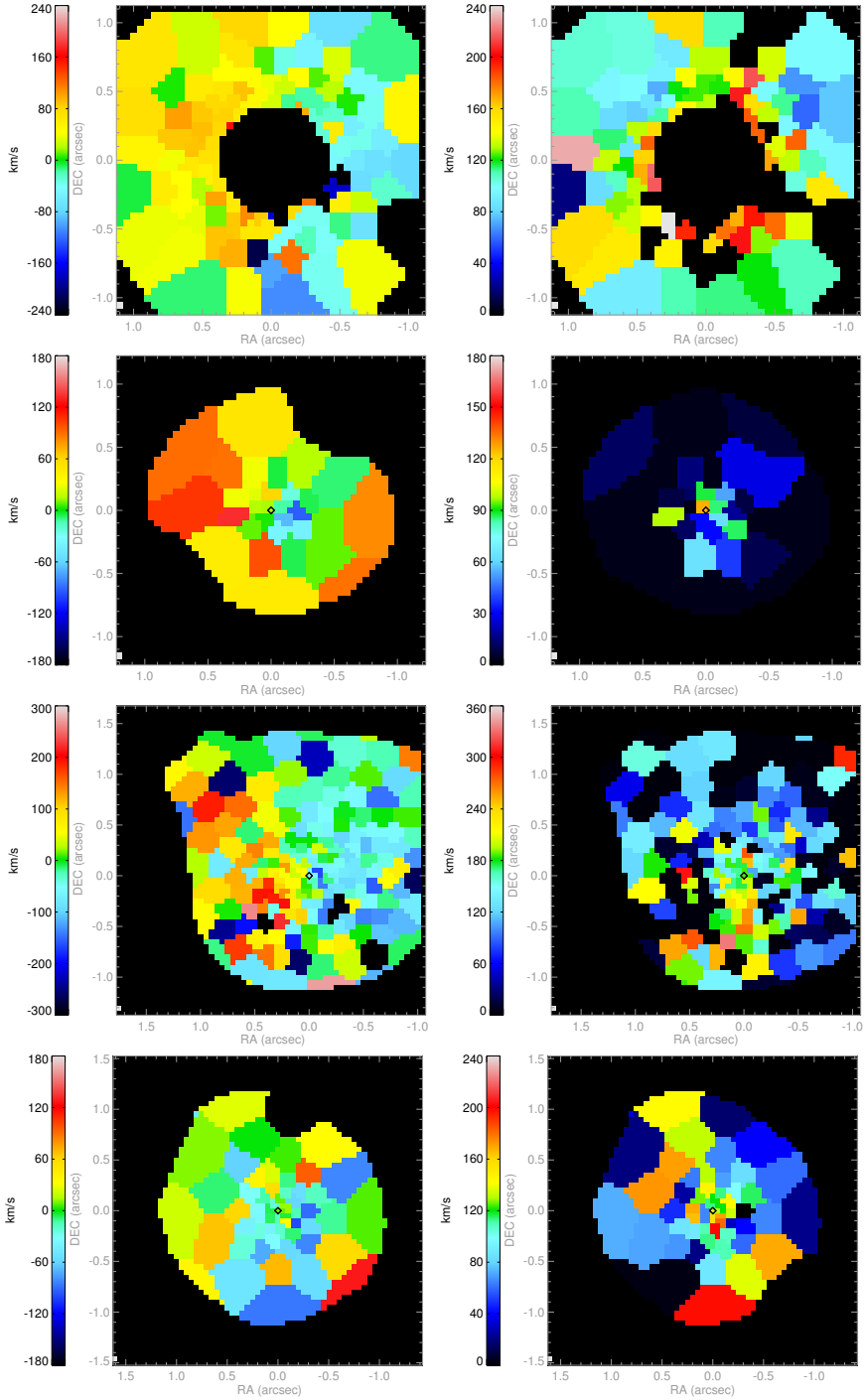


Figure 4.3 – Left: stellar velocity; right: stellar velocity dispersion. From top to bottom: IRAS 05189-2524, IRAS 09111-1007, IRAS 17208-0014 and IRAS 20551-4250. In all images, the (0,0) coordinate is located on the K-band continuum peak, which is also used as the kinematic centre, unless stated otherwise.

and extinction were determined from our SINFONI-data. The average nuclear value was $A_K \sim 1.1$, with a range of A_K between 0 and 1.8 over the whole region. Analysis of the gas dynamics (Chapter 5) using a combination of a spheroid and a disk resulted in an effective radius for the spheroid of 1.6 kpc, slightly outside the range 1.0 ± 0.4 kpc adopted by Genzel et al. (2001). With these values, the total dynamical mass from stellar kinematics is $(6.0 \pm 1.0) \cdot 10^{10} M_\odot$.

The inclination of the gas disk is 30° , and if this inclination is also assumed for the stellar spheroid, the corrected stellar rotation velocity of 260 km/s makes the mass increase by a factor of 1.6, resulting in an M/L_K of $0.06 \pm 0.02 M_\odot/L_{K,\odot}$. Chapter 5 also shows the presence of a disk component of containing 0.46 of the total dynamical mass within the region considered. However, since the (*H*-band) light profile of IRAS 01388–4618 accurately follows a De Vaucouleurs law (Genzel et al. 2001), the stellar light is dominated by the spheroid. It is possible that the disk is largely gaseous, which would result in a nuclear gas fraction of $\sim 50\%$ which is a high value, but not outside the bounds of plausibility. Unfortunately, there is no direct measurement of the molecular gas mass available for this object. Note, however, that because of the relatively high redshift, the field of view covers the galaxy out to a radius of 2.4 kpc, which is significantly beyond R_{eff} . The stellar/bulge component is more important in the central part and the gas fraction within the effective radius is lower (see the fit in Chapter 5). A correction for a $\sim 50\%$ gas component would result in a M_*/L_K of $0.030 \pm 0.01 M_\odot/L_{K,\odot}$.

4.3.3 IRAS 05189-2524

This warm ULIRG has an approximately face-on orientation with literature values for the inclination of ~ 20 - 30° . The *K*-band continuum map shows a compact and regular nucleus, with a strong peak. The stellar absorption bands could only be identified outside a radius of $\sim 0.4''$ (0.34 kpc) from the centre of the nucleus, which is most probably an effect of the AGN which contributes about 55% to the NIR continuum (e.g. Davies et al. 2007), diluting the absorption bands. The velocity field outside this region, however, shows regular stellar rotation with a maximum velocity of ~ 85 km/s. The stellar velocity dispersion seems to rise towards the centre, reaching maximum detectable values of ~ 180 - 200 km/s but the precise value is hard to determine.

The inclination used in the gas velocity model from Pa α (Chapter 5) is 22° . The fitted spheroid has an effective radius of 0.35 kpc, which is a factor 2 smaller than the photometric value found by Dasyra et al. (2006). Given the large contribution of the QSO to the nuclear light, which is not easily removed from the radial light profile, we here use our dynamically determined value for R_{eff} . The kinematic major axis of the stellar velocity field is the same as for the gas, and they therefore likely have the same inclination. The inclination-corrected stellar rotation velocity is then 225 km/s, and the total dynamical mass is $1.8 \cdot 10^{10} M_\odot$. Within the radius $R_{\text{out}}=0.34$ kpc (the radius out to which the gas kinematics was analysed), $M_{\text{dyn}}=8.7 \cdot 10^9 M_\odot$.

Linemaps of Pa α and/or Br γ were not clean enough to determine a pixel-by-pixel extinction correction, and an average value of $A_K = 0.2$ was adopted from Severgnini et al. (2001),

who derive this value for the inner $1.1''$, using the near-IR line ratio $\text{Pa } \alpha / \text{Pa } \beta$. The extinction corrected value of L_K is $3.89 \cdot 10^{11} L_{K,\odot}$. However, the AGN in IRAS 05189-2524 is estimated to be responsible for about 55% of the near-IR radiation (Davies et al. 2007; see also Nardini et al. 2009, Farrah et al. 2003). Then, only taking into account the stellar contribution to the luminosity, the K -band mass-to-light ratio $M_{\text{dyn}}/L_{*,K}$ ($=M_*/L_{*,K}$) is $0.05 \pm 0.02 M_{\odot}/L_{K,\odot}$, where we have used the inclination-corrected stellar rotation velocity.

4.3.4 IRAS 09111-1007

The K -band continuum shows an elongated distribution, with a position angle that is aligned with that of the stellar velocity field. The inclination derived from the axis ratio b/a fitted in the K -band is $\sim 40^\circ$. Stellar rotation is detected, but not defined very accurately and we estimate the value of v_* (uncorrected for inclination) to be ~ 60 -100 km/s. The stellar velocity dispersion shows values varying between 30 and 100 km/s around a single, unresolved peak of 130 km/s that coincides very accurately with the K -band centre, as well as with the peak of the [SiVI] line map detected in the K -band spectrum. This ULIRG thus harbours an AGN, but its contribution to the (near-)IR luminosity is probably very small (e.g. Farrah et al. 2003). A value of σ_* of 110 km/s was derived from a central aperture with a radius of $\sim 0.4''$. The effective radius from the gas dynamical model (Chapter 5) is 2.3 kpc. The total dynamical spheroid mass from stellar kinematics (using an inclination-corrected rotation velocity) is $8.3 \pm 3.4 \cdot 10^{10} M_{\odot}$, the mass within a radius of 1.05 kpc (the radius out to which the gas kinematics was analysed) is $1.8 \pm 0.7 \cdot 10^{10} M_{\odot}$.

The pixel-by-pixel extinction map determined from the $\text{Pa } \alpha / \text{Br } \gamma$ line ratio shows K -band extinctions (A_K) between 0 and 1.6, with an average/maximum central value of $A_K = 1.5$. The value of M_{dyn}/L_K is $0.03 \pm 0.01 M_{\odot}/L_{K,\odot}$ (using the extinction-corrected rotation velocity). The gas kinematic data indicates a disk component with a mass of 30% of the total mass for this object, or $M = 3.6 \cdot 10^9 M_{\odot}$. This is in excellent agreement with the gas mass $M = 3.1 \cdot 10^9 M_{\odot}$ derived for this object by Chung et al. (2009) using CO 1–0 data. Correcting for this gas mass, the stellar mass to light ratio becomes $M_*/L_K = 0.02 \pm 0.01 M_{\odot}/L_{K,\odot}$.

4.3.5 IRAS 17208-0014

This is the “coolest” ULIRG of the sample, with f_{25}/f_{60} of 0.05, while it is also the most luminous in the infrared. The K -band image shows a single nucleus, though the central part has no regular shape and the weaker parts also show some distortion features. The CO-absorption bands were detected with quite high S/N and the stellar rotation map could be derived with high resolution, showing regular rotation over the whole nuclear region. The stellar velocity dispersion map shows mean values of 40-150 km/s in the outer parts, rising to ~ 250 km/s on a location that is offset south of the K -band nucleus position by $0.3''$, a characteristic that is also detected in the gas velocity dispersion ($\text{Pa } \alpha$, H_2), while the gas velocity field centres on the same location. However, also two bins with higher values (~ 250 and 300 km/s) are detected $2''$ north of (0,0) and values are slightly higher (~ 180 km/s) in between these two locations. In the gas kinematic (bulge+disk) model, the exponential disk

Table 4.2 – Stellar kinematics and dynamical mass.

Name	R_{eff} (kpc)	v_* (km/s)	σ_* (km/s)	i ($^\circ$)	v_*/σ_* uncorr/corr	M_{dyn} ($10^{10} M_\odot$)	$M_{\text{dyn}}(\text{corr})$ ($10^{10} M_\odot$)
(1)	(2)	(3)	(4)	(5)	(6)	(7)	(8)
IRAS 01388-4618 ^a	1.6	130^{+15}	144^{+10}	30	0.9 / 1.8	$6.0^{+1.0}$	$9.8^{+1.8}$
IRAS F05189-2524 ^b	0.35	85^{+15}	137^{+16}	22	0.6 / 1.6	$1.1^{+0.3}$	$1.8^{+0.5}$
IRAS F09111-1007	2.3	100^{100}_{68}	110^{+20}	38	0.9 / 1.4	$5.0^{+2.0}$	$8.3^{+3.4}$
IRAS F17208-0014	0.54	120^{150}_{100}	225^{275}_{160}	28	0.5 / 0.9	$4.2^{+2.0}$	$4.8^{+2.3}$
IRAS F20551-4250	1.5	30^{+10}	160^{200}_{80}	36	0.2 / 0.3	$5.5^{+3.5}$	$5.6^{+3.5}$
Arp 220 ^c	2x0.2	130^{+30}	120^{150}_{100}	40	(1.1 / 1.4)	-	$1.2^{+0.4}$

Columns: (2) R_{eff} is derived from a Hernquist profile fit on the gas rotation curve from Pa α or H $_2$ (see Chapter 5). (3) stellar rotation velocity (4) central stellar velocity dispersion (5) inclination, determined by gas disk dynamics or from K-band image. (6) (v_*/σ_*): left value is uncorrected, right value is corrected for inclination. (7) M_{dyn} is the total dynamical mass, calculated using both σ_* and v_* , with formula 4.2. The velocity is *not* corrected for inclination. The error is conservatively estimated by calculating the smallest and largest possible values using the limiting values of v_* and σ_* . (8) $M_{\text{dyn}}(\text{corr})$ is the total dynamical mass with the stellar velocity corrected for inclination.

^a Stellar CO absorption bands were redshifted out of the K-band; values of v_* and σ_* were adopted from Genzel et al. (2001).

^b The CO absorption bands were not detectable in the central $0.4''$ (0.34 kpc) of the nucleus; v_* was measured outside the central region, the measured average value of σ_* on the inner edge is 120 km/s. The value stated is the value adopted from Dasyra et al. (2006).

^c The analysis of this source is described in Chapter 3. M_{dyn} is calculated by summing the values calculated for each nucleus separately, while v_* of the fastest rotating nucleus has individually been corrected for an inclination of 50° . The value of v_*/σ_* is stated in brackets because the stellar nuclei have not merged yet, and only the value of the fastest rotating nucleus has been used.

Table 4.3 – Dynamical mass, K -band luminosity and M/L_K within R_{out} .

Name	R_{out} (kpc)	M_{dyn} ($10^{10} M_{\odot}$)	$L_K(\text{uncorr})$ ($10^{10} L_{K,\odot}$)	$L_K(\text{corr})$ ($10^{10} L_{K,\odot}$)	M_{dyn}/L_K $\left(\frac{M_{\odot}}{L_{K,\odot}}\right)$	M_*/L_K $\left(\frac{M_{\odot}}{L_{K,\odot}}\right)$	Age (SB99) inst	cont
(1)	(2)	(3)	(4)	(5)	(6)	(7)	(8)	(9)
IRAS 01388-4618	2.4	6.0 ± 1.0	24.3	108	0.06 ± 0.015	0.03 ± 0.01	$13.5 \text{ Myr}_{12}^{15}$	$< 30 \text{ Myr}$
IRAS F05189-2524	0.34	0.87 ± 0.25	32.1	17.5^a	0.05 ± 0.017	0.05 ± 0.02	15 Myr_{13}^{18}	$\sim 50 \text{ Myr}$
IRAS F09111-1007	1.05	1.8 ± 0.7	4.97	63.6	0.03 ± 0.013	0.02 ± 0.01	11 Myr_9^{13}	$< 30 \text{ Myr}$
IRAS F17208-0014	1.0	3.3 ± 1.6	4.73	10.7	0.31 ± 0.16	0.27 ± 0.16	$120 \text{ Myr}_{32}^{240}$	$\sim 1.5 \text{ Gyr}$
IRAS F20551-4250	0.9	1.9 ± 1.4	3.15	5.62	0.34 ± 0.26	0.27 ± 0.21	$120 \text{ Myr}_{15}^{240}$	$\sim 1.5 \text{ Gyr}$
Arp 220	0.6	1.2 ± 0.4	1.8	9.01	0.13 ± 0.04	0.05 ± 0.02	15 Myr_{13}^{18}	$\sim 50 \text{ Myr}$

Columns: (2) R_{out} is the major axis length of an ellipse shape within the SINFONI field of view, for which gas dynamics is analysed in Chapter 5. M_{dyn} , L_K and M/L_K in this table are calculated within R_{out} . (3) Inclination corrected dynamical mass within R_{out} . (4) $L_K(\text{uncorr})$ is the total uncorrected K -band luminosity from the same dataset, measured within the ellipse with major axis R_{out} , expressed in solar K -band luminosities ($M_{K,\odot}=3.28$). The typical error in L_K is 10%. (5) $L_K(\text{corr})$ is corrected for extinction. The error in $L_K(\text{corr})$ is $\sim 20\%$, based on the error in $L_K(\text{uncorr})$ and the extinction correction. (6) M_{dyn}/L_K within R_{out} , using extinction corrected value of L_K . (7) M_* is M_{dyn} with a gas component subtracted as described in the text. (8) Starburst age from M_*/L_K value for an instantaneous burst model, see text (Discussion). (9) Age from M_*/L_K value for continuous star formation with a star formation rate of $100 M_{\odot}/\text{yr}$.

^a For IRAS 05189-2524, an extinction correction of $A_K \sim 0.2$ was adopted from Davies et al. (2007), and a component of 55% has been subtracted for the AGN. The error estimate in $L_K(\text{corr})$ of IRAS 05189-2524 is 30%.

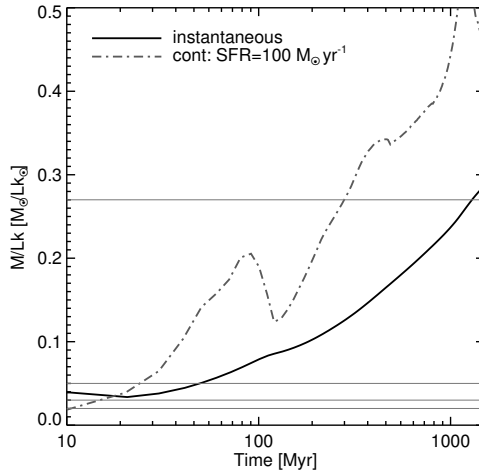


Figure 4.4 – Evolution of the K -band mass to light ratio from Starburst99, for an instantaneous burst (solid black line) and continuous star formation at a rate of $100 M_{\odot} \text{ yr}^{-1}$ (dot-dashed line). The horizontal grey lines denote M/L_K values derived for the targets in this work.

component was constrained to have the mass indicated by molecular gas (CO) data from Downes & Solomon (1998). The spheroid component was then fitted with an effective radius R_{eff} of 0.54 kpc. The gas fraction within the central region (out to $R_{\text{out}}=1.05$ kpc) is 10%. An inclination of the gas disk of 27° was used for gas kinematic model, whereas from the K -band axial ratio it is estimated 35° . Using the conservative value of 35° , v_* becomes 209 km/s, resulting in a total $M_{\text{dyn}}=4.8 \pm 2.3 \cdot 10^{10} M_{\odot}$ ($3.3 \pm 1.6 \cdot 10^{10} M_{\odot}$ out to $R_{\text{out}}=1.05$ kpc).

The central extinction map from $\text{Br}\gamma/\text{Pa}\alpha$ has values of A_K ranging from 0 to 2.0, with an average of ~ 1.2 . The extinction corrected value of M_{dyn}/L_K then is $0.31 \pm 0.16 M_{\odot}/L_{K,\odot}$ (using the stellar velocity corrected for inclination). Subtracting the 10% gas mass corrects this value to $M_*/L_K = 0.27 \pm 0.16 M_{\odot}/L_{K,\odot}$.

4.3.6 IRAS 20551-4250

Considering its infrared colours ($f_{25}/f_{60}=0.15$), this is a moderately warm ULIRG. The K -band nucleus is rather compact, but not as sharp as IRAS 05189-2524. The stellar velocity field does have signs of rotation, but the direction is not as clear as in the other objects. The value for rotation is estimated to be only 30 km/s. The velocity dispersion map has a peak of 200 km/s just south of (0,0), but consistent with the peak position in the K -band continuum image. The average velocity dispersion value was taken 120 km/s. The effective radius from bulge component of the gas kinematic fit was $R_{\text{eff}}=1.5$ kpc, within the range estimated by Genzel et al. (2001). The axis ratio of the gas disk (Chapter 5) gives an inclination of 36° , different from that derived from the axis ratio of the K -band image, 17 - 25° . The effect on the dynamical mass is small (2% for 30° inclination, 12% for 20° inclination), and since the

velocity field is not very regular, this effect is not taken into account.

The extinction map derived from Pa α /Br γ has values of A_K between 0 and 1.0, the average value is $A_K = 0.9$. The K -band mass-to-light ratio M_{dyn}/L_K is $0.34 \pm 0.26 M_{\odot}/L_{K,\odot}$. Subtracting a gas fraction of 20% (the disk component of the gas dynamical fit) results in a M_*/L_K of $0.27 \pm 0.21 M_{\odot}/L_{K,\odot}$.

4.4 Discussion

4.4.1 Uncertainties in mass determinations

Formula 4.1, calculating the dynamical mass from stellar velocity dispersion or also taking into account stellar rotation (Form. 4.2) are often used for mass determinations of spheroidal objects, e.g. by Tacconi et al. (2002), Dasyra et al. (2006), Davies et al. (2007). The reliability of the spectrum fit with one or more stellar templates, resulting in a velocity and a velocity dispersion is only one of the complicating factors. Rotation of the stellar component is taken into account, but deriving the inclination is not trivial and can be a major source of uncertainty. For face-on objects like IRAS 05189-2524, the effect can be quite large. Also, the resulting mass scales linearly with the assumed effective radius (R_{eff}), defined as the radius within which half of the light is contained. Although the formula suggests one fixed value, R_{eff} is known to depend on the wavelength of the observation (Temi et al. 2008). We have avoided this uncertainty by using the effective radius as determined from the Hernquist-bulge potential (Hernquist 1990), which was used to fit a stellar spheroid (bulge) component to the gas rotation curve, thus resulting in a mass-based value rather than a light-based value. The value of the mass-based effective radius is generally smaller than the value determined from the light profile, which could be caused by high extinction in the nuclear region. The effect is described in more detail in Chapter 5. A further complication is the mass model. While we adopt a spherically symmetric Hernquist model, our K -band images show that for several objects spherical symmetry is at best only approximately correct. Furthermore, in at least one object a dynamically important disk component is found. In summary, even with our high quality data the derivation of dynamical masses is fraught with considerable uncertainties, and this is reflected by the error margins.

4.4.2 Uncertainties in luminosity determinations

The greatest uncertainty in the derived K -band luminosity is the extinction. Although we attempt to make extinction-corrections from near-IR line ratios, one should be aware of the fact that if extinctions are very high in (the very centre of) a nuclear region, radiation in the K -band emission is absorbed. For all of our sample ULIRGs, we find central values of A_K of ~ 1 , which is what is to be expected when essentially looking at the edge of an optically thick region instead of into it. If this is the case, intrinsic values can be even higher.

4.4.3 M/L_K : expectations and implications

A summary of our M/L_K values is given in Table 4.3. While the uncertainties are considerable (see above), it is clear that the results separate into two groups: values of a few tenths and values of a few hundredths. All of our mass-to-light ratios are much lower than those of old ($> 10^{10}$ yr), early type galaxies, consistent with the result of Tacconi et al. (2002), who also find the higher and comparable values for IRAS 17208-0014 and IRAS 20551-4250 (although not all of our objects are covered in their sample). The young implied ages also indicate that a significant (possibly dominant) fraction of the K-band light is contributed by the starburst, consistent with the conclusion by Engel et al. (2011) for Arp 220.

If an instantaneous burst of star formation would be responsible for the complete build-up of the stellar population, the ages corresponding to the mass-to-light ratios are typically $(1-2) \cdot 10^7$ yr for values of M/L_K between 0.02 and 0.05 (IRAS 01388-4618, IRAS 09111-1007, IRAS 05189-2524 and Arp 220), and $(1-2) \cdot 10^8$ yr for values of M/L_K between 0.2-0.4 (IRAS 17208-0014 and IRAS 20551-2450), column (9) of table 4.3. These ages are based on synthetic stellar population models of Starburst99 (Leitherer et al. 1999, Vázquez & Leitherer 2005), with a power law stellar initial mass function with slope $\alpha=2.35$, solar metallicity ($Z_{\odot}=0.020$) and upper and lower mass cutoffs of 100 and $0.1 M_{\odot}$, respectively, see Fig. 4.4. Note that using stellar population models with a lower mass cutoff of $1 M_{\odot}$ (as sometimes proposed for starburst regions) increases the ages by a factor of at least 2 with respect to a lower mass cutoff of $0.1 M_{\odot}$ which we adopt here. When assuming a constant star formation rate, the only period where values $M/L_K \leq 0.03$ are found, is in the first 10 Myr (see also Fig. 4.4). The value starts to gradually increase at ~ 30 Myr (see column (10) of table 4.3). A value of 0.05 is reached at an age of ~ 50 Myr, steadily rising to $M/L_K \sim 0.1$ at 1 Gyr, and further. This means that the ages for values of $M/L_K \leq 0.05$ are of the same order for an instantaneous burst and continuous star formation, but that values of $M/L_K \geq 0.2$ imply higher ages with continuous star formation (> 1 Gyr) than for a burst. Since the high star formation rates for ULIRGs cannot be sustained over periods of the order of a Gyr, we consider only the ages implied by the instantaneous burst model.

4.4.4 An evolutionary path with M/L_K ?

Given that the M/L_K appears to be rough age indicator, it is interesting to look for evolutionary trends with M/L_K . We do not find an evolutionary trend with infrared colour (f_{25}/f_{60}), which would confirm the scenario where these objects are on an evolutionary path from cool to warm ULIRGs to QSOs. While this may partly be due to small number statistics, it is remarkable that our coolest ULIRG (IRAS 17208–0014) has a high derived age, while our warmest ULIRG (IRAS 05189–2524) has a low derived age, and this is opposite from the effect expected if there is a simple evolutionary path from cool to warm ULIRG. Likewise, there is no trend of gas mass fraction with M/L_K . The most likely explanation is that our model where one starburst characterises the entire evolution of a ULIRG is too simplistic. Models of merging galaxies in fact indicate several burst events, first when the galaxies have their first encounter (as represented by IRAS 17208–0014) and then when they have their

final merging event (as exemplified by IRAS 05189–2524). While M/L_K would still be time-dependent in this model, the derived age is only the age since the most recent starburst event. Since our data shows that the circumnuclear starburst in IRAS 05189–2524 is quite young, this explanation suggests that its final merging event occurred only recently.

4.5 Conclusions and outlook

We have analysed the stellar kinematics of 6 ULIRGs using high resolution near-IR integral field spectroscopy. Our main findings are as follows:

1. The ULIRGs in this study have low central K -band mass-to-light ratios, $< 0.3 M_{\odot}/L_{K,\odot}$, and even $< 0.1 M_{\odot}/L_{K,\odot}$ for several objects. These values are significantly lower than those of evolved elliptical galaxies. Starburst ages related to these M/L_K -values range from ~ 10 -200 Myr.
2. We do not see evidence for an evolutionary connection between infrared colour (f_{25}/f_{60}) and the stellar K -band mass-to-light ratios (or derived starburst ages), and conclude that the M/L_K traces only the stage of the most recent starburst in the system, which is not easily related to the evolutionary stage of the total ULIRG system.

The ability of these data to trace the age of the most recent significant starburst event in ULIRGs opens the way to interesting new applications in the modelling of these systems. Star formation in ULIRGs occurs in very dense regions and as a result, a large fraction of the star formation occurs in compact or ultracompact HII regions. In this situation, a large fraction of the Lyman continuum photons are absorbed by dust in the HII regions and not used for photoionization. As a result, models for ULIRGs based on standard photoionization methods (e.g., Starburst99) will fail. Since M/L_K as derived here does not depend on photoionization, it will circumvent this problem and readily provide an age determination for the most recent starburst. This application will be explored in a future paper.

References

- Bender, R., Burstein, D., & Faber, S. M. 1992, ApJ, 399, 462
 Bonnet, H., Abuter, R., Baker, A., et al. 2004, The Messenger, 117, 17
 Cappellari, M. & Emsellem, E. 2004, PASP, 116, 138
 Chung, A., Narayanan, G., Yun, M. S., Heyer, M., & Erickson, N. R. 2009, AJ, 138, 858
 Dasyra, K. M., Tacconi, L. J., Davies, R. I., et al. 2006, ApJ, 651, 835
 Davies, R. I., Sánchez, F. M., Genzel, R., et al. 2007, ApJ, 671, 1388
 Downes, D. & Solomon, P. M. 1998, ApJ, 507, 615
 Eisenhauer, F., Abuter, R., Bickert, K., et al. 2003, in Proceedings of the SPIE, Vol. 4841, Instrument Design and Performance for Optical/Infrared Ground-based Telescopes., ed. M. Iye & A. F. M. Moorwood, 1548–1561
 Engel, H., Davies, R. I., Genzel, R., et al. 2011, ApJ, 729, 58
 Farrah, D., Afonso, J., Efstathiou, A., et al. 2003, MNRAS, 343, 585
 Ferrarese, L. & Merritt, D. 2000, ApJ, 539, L9
 Gebhardt, K., Bender, R., Bower, G., et al. 2000, ApJ, 539, L13

- Genzel, R., Tacconi, L. J., Rigopoulou, D., Lutz, D., & Tecza, M. 2001, *ApJ*, 563, 527
- Hernquist, L. 1990, *ApJ*, 356, 359
- Hummer, D. G. & Storey, P. J. 1987, *MNRAS*, 224, 801
- Leitherer, C., Schaerer, D., Goldader, J. D., et al. 1999, *ApJS*, 123, 3
- Magorrian, J., Tremaine, S., Richstone, D., et al. 1998, *AJ*, 115, 2285
- Nardini, E., Risaliti, G., Salvati, M., et al. 2009, *MNRAS*, 399, 1373
- Sanders, D. B., Mazzarella, J. M., Kim, D.-C., Surace, J. A., & Soifer, B. T. 2003, *AJ*, 126, 1607
- Sanders, D. B., Soifer, B. T., Elias, J. H., et al. 1988, *ApJ*, 325, 74
- Severgnini, P., Risaliti, G., Marconi, A., Maiolino, R., & Salvati, M. 2001, *A&A*, 368, 44
- Tacconi, L. J., Genzel, R., Lutz, D., et al. 2002, *ApJ*, 580, 73
- Temi, P., Brighenti, F., & Mathews, W. G. 2008, *ApJ*, 672, 244
- Vázquez, G. A. & Leitherer, C. 2005, *ApJ*, 621, 695

Nuclear gas dynamics of Ultraluminous Infrared Galaxies



L. Vermaas, N. Neumayer and P. P. van der Werf

Abstract

We present high resolution near-infrared integral field spectroscopy of a sample of ultraluminous infrared galaxies (ULIRGs). We derive velocity fields for the nebular emission lines and model these using sets of tilted rotating rings. The resulting rotation curves are analysed with mass models consisting of a combination of a purely stellar Hernquist bulge and an exponential disk, which is mostly or completely gaseous. This analysis results in dynamical masses, stellar masses, and stellar K -band mass to light ratios, within the region observed, for all our targets. The most important source of uncertainty in the analysis is the inclination of the gas disks. We find that for 50% of our targets, the derived stellar masses match the independently determined values based on the stellar dynamics (derived in Chapter 4). These objects display gas velocity fields that are well represented by the tilted ring models. In the other 50% of the cases discrepancies are found between the masses derived using gas dynamics and stellar dynamics, and we attribute these mostly to bulk gas motions that are not well represented using a set of tilted rings. We use our results to investigate the location of our targets with respect to the fundamental plane of dynamically hot stellar systems, and find an offset which can be attributed fully to the M/L ratios of our targets, which are lower than those of quiescent more evolved ellipticals. Passive evolution in the light profile will eventually bring these objects on the fundamental plane in the region of intermediate mass and luminosity ellipticals (and not of giant, massive ellipticals), unless further dynamical evolution would increase the effective radii by factor of about three.

5.1 Introduction

Ultraluminous infrared galaxies (ULIRGs) are spectacular systems with infrared luminosities $L_{\text{IR}} \geq 10^{12} L_{\odot}$. Nearly all are strongly interacting merger systems with a large amount of molecular gas, while most of the interstellar matter is concentrated in the inner regions of these objects, with extreme nuclear starbursts. The energy source is a combination of starburst and an active galactic nucleus (AGN), in varying proportion, as derived from spectroscopy and imaging at wavelengths from radio to X-rays. ULIRGs have a range in infrared spectral energy distributions, which is often expressed in the ratio of flux in the $25 \mu\text{m}$ and the $60 \mu\text{m}$ bands: “cool” ULIRGs have a typical ratio $f_{25}/f_{60} \leq 0.10$, whereas for “warm” ULIRGs $f_{25}/f_{60} > 0.2$. Warm ULIRGs have compact, bright nuclei compared to cool ULIRGs.

The AGN-starburst connection has become a central issue with the discovery of the relation between stellar velocity dispersion and mass of the central black hole in spheroidal stellar systems (Magorrian et al. 1998, Ferrarese & Merritt 2000, Gebhardt et al. 2000). Given that elliptical galaxies are mainly old, this relation has to be put in place at their formation history. Since ULIRGs form stars at prodigious rates, $10^2 - 10^3 M_{\odot} \text{yr}^{-1}$, and often host an AGN as well, they may be regarded as local analogs to forming spheroids. These points have been emphasised in extensive studies by Genzel et al. (2001) and Tacconi et al. (2002). While these studies indicate that local ULIRGs evolve into intermediate mass rather than giant ellipticals, they are still the best available local laboratories for studying the processes occurring in more luminous high- z objects such as the sub-mm galaxies, which may be the sites of the coeval explosive buildup of stellar mass and a supermassive black hole.

A conceptually simple mechanism for establishing a relation between stellar mass and black hole mass is based on feedback from the AGN terminating star formation. Sanders et al. (1988) argue that ULIRGs are dust-obscured precursors of QSOs. On this evolutionary path, the AGN disperses the dust and gas, shifting the bulk of energy toward shorter wavelengths, eventually becoming an optically bright QSO. In the context of the coeval buildup of stellar mass and black hole mass, the dispersal of dust and gas would also terminate star formation, and thus provides a possible mechanism for establishing a relation between black hole mass and stellar mass: once the black hole becomes so massive that its feedback on the environment disperses the gas, it shuts down star formation and the stellar mass is fixed. The dispersal of the gas also limits further growth of the black hole. The stellar mass is then given by the integral of star formation over time during the ULIRG phase, the black hole mass by the integral of accretion rate over time.

The accumulation of gas, followed by star formation and subsequent dispersal of the gas thus forms a key process in the evolution of ULIRGs. While the stellar components of the original galaxies are in a slow process of merging by dynamical friction, the gas components merge much faster because the gas can dissipate mechanical energy. The gas thus flows toward the centre of the potential well on a short timescale, where it forms a disk or ring. CO interferometry (e.g., Downes & Solomon 1998) shows that such structures are ubiquitous in local ULIRGs, and that gas moves on circular orbits in an ordered velocity field characterised by a rising rotation curve in the inner part which flattens at a radius of about 0.5 kpc or smaller. A theory by Elmegreen (1994) is that the molecular disk is initially stable against

star formation because of the high shear in the nuclear region, which keeps the Toomre Q -parameter high. The continuing buildup of surface density in the disk makes it eventually Toomre-unstable and an explosive phase of star formation follows, because the gas density must be very high before the shear can be overcome. This process is expected to destroy the disk and disperse the gas, and a forming AGN, if present, becomes visible.

Near infrared observations show that H_2 emission is an excellent tracer of these disks. The bright emission of the vibrational H_2 $2.12\ \mu\text{m}$ line is a general characteristic of ULIRGs (Goldader et al. 1995), while this line is much weaker (relative to total IR luminosity) in less luminous starbursts. A detailed study of the nucleus of Cen A with SINFONI data by Neumayer et al. (2007) shows that the H_2 is the best gas tracer of the potential in galactic nuclei. The H_2 emission has a fairly complex flux distribution but its velocity field is characteristic of a rotating disk. This disk can be modelled by a set of tilted rings, which fits the data extremely well, in spite of the complex flux distribution. In contrast, the other emission lines ([FeII], Br γ , [SiVI]) are increasingly affected by non-gravitational motions. The fact that H_2 traces the potential well closely is confirmed by the agreement in black hole masses as derived from the H_2 data and the stellar kinematics using CO bandhead from the same dataset (Cappellari et al. 2009). Neumayer et al. show that any residual unresolved gas velocity dispersion in the disk can be included using a small pressure term in the dynamical equations.

If ULIRGs indeed evolve into elliptical galaxies, they should also show the characteristic scaling relations of elliptical galaxies, in particular the so-called Fundamental Plane (FP), which relates the effective radius R_{eff} , the average surface brightness within R_{eff} , and the central velocity dispersion of an elliptical galaxy. On the other hand, the location of a galaxy with respect to the FP depends on its mass to light ratio (M/L), and an important evolving young stellar population will have a different M/L than a quiescent elliptical galaxy.

In this paper we present our SINFONI, AO-assisted near infrared integral field spectroscopic observations of a small sample of ULIRGs with colours ranging from “cool” to “warm”. While the stellar dynamics are analysed in Chapter 4, here we focus on the dynamical properties of the nuclear gas disks determined from the same data sets. We derive rotation curves, and present dynamical models for these. Finally, we discuss the implications of our results for the understanding of the evolution of these systems.

5.2 Observations and data reduction

Six objects were selected from the IRAS Revised Bright Galaxy Sample (Sanders et al. 2003). For qualification as an ULIRG, $L_{\text{ir}} \geq 10^{12}$ and our targets meet this requirement within the errors of measurement for L_{ir} . We used a redshift criterion $z \leq 0.12$, in order to have enough spatial resolution and to be able to detect stellar CO-bandheads. The sample spans a range in infrared colours, in order to have a “sequence” from cool to warm ULIRGs (QSOs), albeit with very limited statistics. The infrared colour is determined by the ratio of flux in the $25\ \mu\text{m}$ band and the $60\ \mu\text{m}$ band (f_{25}/f_{60} ; < 0.2 qualifies as ‘cool’ and > 0.2 qualifies as ‘warm’). The analysis of Arp 220, has been discussed in Chapter 3, and is here included for comparison.

Table 5.1 – Observed sources

Name	z	$\log(L_{\text{ir}}/L_{\odot})$	f_{25}/f_{60}	kpc $''$
IRAS 01388-4618	0.090289	12.03	0.12	1.79
IRAS F05189-2524	0.042563	12.09	0.26	0.84
IRAS F09111-1007	0.054141	11.95	0.11	1.07
IRAS F17208-0014	0.042810	12.33	0.05	0.86
IRAS F20551-4250	0.042996	11.98	0.15	0.86
Arp 220	0.018126	12.21	0.06	0.36

^a The analysis of Arp 220, with a double nucleus in the K -band, is described in Chapter 3 and is included for comparison reasons.

The objects were observed with SINFONI, the Spectrograph for INtegral Field Observations in the Near Infrared (1.1 - 2.45 μm), which is installed on UT4 of the VLT (Eisenhauer et al. 2003, Bonnet et al. 2004), the Laser Guide Star facility was used for Adaptive Optics. Since no bright nearby reference stars were available, the optical host galaxies were used for tip-tilt sensing. Since this procedure is not optimal (but no better option was available), Strehl ratios and angular resolution were somewhat reduced with respect to the ideal case. The intermediate platescale was used, with a field of view of $3'' \times 3''$ onto 64×64 spatial pixels. Each of these pixels is projected onto 2218 spectral elements in the K -band, with a central wavelength of 2.2 μm . This results in spatial pixels with a resolution of $0.05'' \times 0.10''$, and a spectral resolution $\lambda/\Delta\lambda$ of 4000.

For the pointings, an ABA'-nodding mode was used, i.e. object-sky-object with equal integration times of 900 s, with the A' frame slightly shifted with respect to the A frame. The total (on-source) integration time was 6x900 s, or 75 minutes in most cases. The observations of IRAS 01388-0014, IRAS 05189-2524 and IRAS 09111-1007 were carried out on December 29 and 30, 2007, with average visual seeing of $0.8''$. The observations of IRAS 17208-0014 and IRAS 20551-4250 were carried out on July 18 and 19 of 2009 with an average visual seeing of $0.7''$. Achieved Strehl ratios were in the order of 0.20-0.30.

The data were reduced with the SINFONI pipeline, which was developed by ESO and the Max-Planck-Institut für extraterrestrische Physik. The default procedure included corrections for pixel non-linearity, distortion and wavelength calibration.

For both flux calibration and telluric feature removal, a standard star was observed with the same setup as was used for the science frames, typically an early type star containing few stellar lines in the NIR. After reduction, the average stellar spectrum was extracted and the stellar lines were removed (Br γ). Finally, each spectrum of the object frame was divided by this extracted spectrum.

In the case of IRAS 01388-4618, IRAS 05189-2524 and IRAS 09111-1007, the PSF was $0.24''$ (FWHM) as determined from the [SiVI] line map of IRAS 09111-1007, which is as-

sumed to originate from a point-source. For IRAS 17208-0014 and IRAS 20551-4250, the PSF-size was determined from observations of QSO Mrk 1014, in the same night, with the same instrumental setup and was measured to be $0.2''$ (FWHM).

Our datasets provide measurements of gas kinematics and stellar kinematics in the same dataset, but in this chapter we focus on only the gas kinematics, and describe the stellar kinematics separately in Chapter 4.

5.3 Results and analysis

5.3.1 Spectra and images

Fig. 5.1 shows the nuclear spectra of the observed ULIRGs. The Pa α and Br γ recombination lines are generally strong in ULIRGs that are in their “cool” phase. Also luminous H₂ is a general characteristic of ULIRGs. Stellar CO absorption bands are detected in some ULIRGs, dependent on redshift; an analysis of stellar kinematics is carried out in Chapter 4.

The emission lines Pa α , Br γ , and the H₂ vibrational lines were fitted with single Gaussians in each pixel. The resulting maps of the H₂ and Pa α line emission, as well as the *K*-band continuum are shown per galaxy in Figs. 5.2-5.11 (a), (c) and (e). In most objects, Pa α as well as H₂ are peaking at the nucleus position. In some cases, the Pa α map shows a distorted morphology, most likely a result of the merging process. The same figures show the velocity field of H₂ (b) and Pa α (d) and the velocity dispersion of either H₂ or Pa α (f).

5.3.2 Tilted ring fitting

The H₂ and Pa α velocity fields were fitted with a set of tilted rings, using the IDL-based code Kinemetry (Krajnović et al. 2006). The kinematic centre position was fixed, tilted rings were fitted at increasing radii (r), with position angle (PA) as free parameter and the flattening ($q = b/a = \cos i$) fixed, or free within a very small range. The inclination was determined by either (literature) measurements of molecular (CO) gas, or using axis ratios from high resolution radio continuum or the *K*-band image, in that order of preference, as specified in Table 5.2. The fit parameters are also in table 5.2.

The bottom panels of Figs. 5.2-5.11 show the Kinemetry model velocity field from either Pa α or H₂ (g) and the residual map ($v_{\text{res}} = v_{\text{orig}} - v_{\text{circ}}$) (h). The (symmetric) model rotation curve (inclination-corrected) extracted along the line of nodes (marked by \diamond) is for each object presented in a separate figure in the text.

5.3.3 Rotation curves, dynamical masses and M/L_K

We inserted the inclination corrected gas rotation curve from Pa α , or H₂ in the case of IRAS 05189-2524, in GIPSY (the Groningen Image Processing SYstem, an interactive software system for the reduction and display of astronomical data) and used the procedure ROTMAS to make a model of the mass. Each rotation curve was fitted with a combination of a

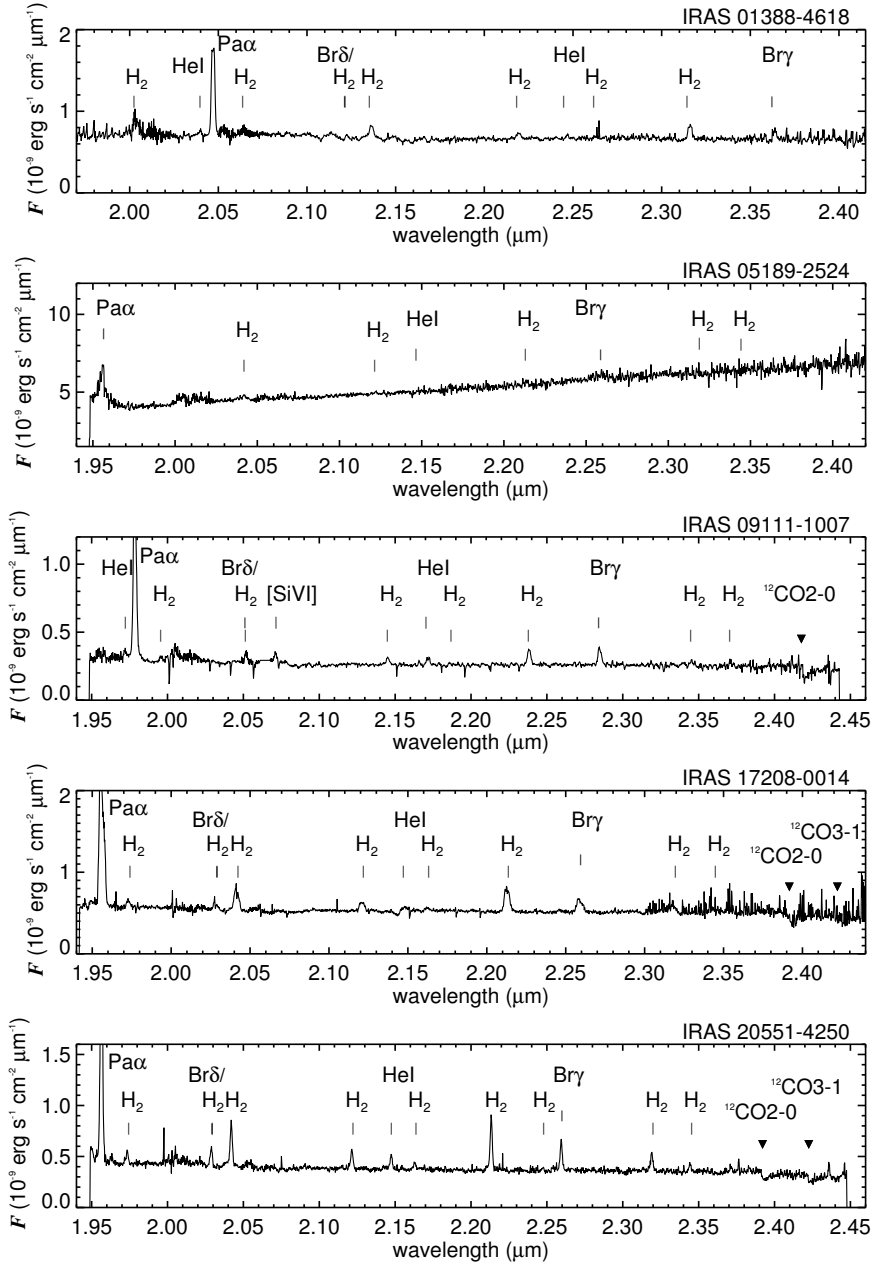


Figure 5.1 – Integrated K-band spectra of (top to bottom) IRAS 01388-4618, IRAS 05189-2524, IRAS 09111-1007, IRAS 17208-0014, IRAS 20551-4250.

Table 5.2 – Kinemetry parameters: inclination (i , fixed in the fit) and its possible range range, position angle (PA) and range (free in the fit), the radius of flattening of the rotation curve (R_{flat}) and the maximum velocity (v_{max}). Results of the GIPSY-fit of the rotation curve with exponential disk and bulge and bulge (Hernquist) components are also given.

Name	$\langle i \rangle$ ($^\circ$)	[range i] ($^\circ$)	$\langle \text{PA} \rangle$ ($^\circ$)	[range PA] ($^\circ$)	R_{flat} (kpc)	v_{max} (km/s)	exponential disk		Hernquist spheroid	
							h (kpc)	Σ_0 ($M_\odot \text{pc}^{-2}$)	R_{eff} (kpc)	$M_{\text{b,tot}}$ (M_\odot)
(1)	(2)	(3)	(4)	(5)	(6)	(7)	(8)	(9)	(10)	(11)
IRAS 01388-4618	30^b	[22-44]	56	[46-63]	0.7	210	1.1	$2.1 \cdot 10^3$	1.6	$2.0 \cdot 10^{10}$
IRAS F05189-2524 ^a	22^b	[4-27]	90	[81-105]	0.18	91	-	-	0.35	$1.1 \cdot 10^9$
IRAS F09111-1007	38^b	[35-44]	62	[55-80]	0.74	242	0.5	$4.0 \cdot 10^3$	2.3	$3.4 \cdot 10^{10}$
IRAS F17208-0014	28^c	[25-45]	125	[120-129]	0.38	545	0.46	$5.5 \cdot 10^3$	0.54	$6.4 \cdot 10^{10}$
IRAS F20551-4250	36^b	[17-25]	40	[35-47]	0.55	118	0.35	$9.0 \cdot 10^2$	1.5	$5.8 \cdot 10^9$
Arp 220	40^c	-	40	[32-53]	-	-	0.35	$1.27 \cdot 10^4$	2.5	$5.1 \cdot 10^{10}$

Columns: (2) Mean inclination of the fit. i is constraint, or free within a very small range. (3) The range of possible inclinations from ellipse-fitting to the SINFONI K -band flux image. (4) Mean position angle of the fit. PA is a free parameter without constraints. (5) The range of PA-values in the model. (6) Radius where rotation curve becomes flat. (7) Maximum velocity reached in the rotation curve, inclination corrected. (8) Scale height of the exponential disk fit. (9) Surface mass density of the exponential disk fit. (10) Effective radius of the bulge fit. (11) Total mass of the bulge fit.

^a Only fit with a bulge component.

^b Inclination derived from K -band image.

^c Inclination derived from CO-data (Downes & Solomon 1998).

Hernquist potential (representing a spheroid or bulge component) and an exponential disk, except the curve of IRAS 05189-2524, which was only fitted with a Hernquist potential.

These objects generally have NIR light profiles that obey a De Vaucouleurs $r^{1/4}$ law (e.g., Scoville et al. 2000), while the gas components have much flatter flux distributions. We therefore take as starting point that the stellar component of the system is represented by the Hernquist bulge in our fit, while the disk in our fit is assumed to represent the gas component. The correctness of this approach can be verified by comparing the resulting disk masses to literature measurements of the gas mass. This procedure results in a stellar bulge, described by the effective (half light or mass) radius R_{eff} and a total bulge mass M_{b} , and a gas disk with a scale length h (kpc) and central surface mass density Σ_0 ($M_{\odot} \text{pc}^{-2}$).

The inner part of the rotation curve is most likely not suitable for a reliable fit, for several reasons. First, the extinction in the very centre of the nucleus can be very high, even in the near-IR, so the measured flux and shift of the line are in fact averaged values of the visible edges of the nucleus. For this reason, even extinction measurements from near-IR line ratios are lower limits. Second, many objects of this kind have a ring-shape in the very central region (e.g. Downes & Solomon 1998), in which case no gas is present within a certain radius. Finally, even our high resolution data may not sufficiently resolve the kinematic structure of the gas disk in the nucleus, leading to significant beam smearing at small radii. Therefore, in this fitting process, we focus on fitting the shape of the outer part of the rotation curve, which is sensitive to the enclosed mass, as well as the effective radius of the bulge and the scale length of the disk. The largest uncertainty in the determination of the rotation curve is the inclination. While the effect on the height of the curve (v_{max}) can be quite large, especially when close to face-on, the spatial scale (or the (relative) values of R_{eff} and h in the fit) are hardly affected by inclination changes. The mass of both components was then computed within R_{out} , which is the physical radius corresponding to the major axis of largest ellipse region fitted by the Kinemetry code. The results are presented in Table 5.3, columns (3)-(5).

For the same region, the K -band luminosity (L_K) was determined and extinction corrected from a pixel-to-pixel derived extinction map from the line ratio $\text{Pa } \alpha / \text{Br } \gamma$, which is described in Chapter 4. The (extinction corrected) values of L_K , M_{dyn}/L_K and M_*/L_K are stated in columns (7)-(9) of table 5.3, respectively. Here L_K is the extinction-corrected K -band luminosity, M_{dyn} is the dynamical mass and M_* is the stellar mass (i.e., the mass of the fitted Hernquist spheroid), all calculated within the radius R_{out} . No formal fit errors are given for the derived masses, this is because the dominant error source is the inclination, and the effects of the uncertainty in the inclination are discussed below in Sect. 5.4.2. The relative contributions of the gas and stellar (or disk and bulge) components of the fit may vary, which directly affects the gas fraction $M_{\text{gas}}/M_{\text{dyn}}$ and M_*/L_K , while the total dynamical mass is quite insensitive to this.

5.3.4 IRAS 01388-4618

This is the most distant ULIRG of the sample, with a redshift of 0.09. H_2 (Fig. 5.2a) shows a regular distribution, similar to the NIR continuum (upper right) which peaks on the same location. $\text{Pa}\alpha$ (c) is wide-spread and peaks in the centre as well, but shows an asymmetric distribution with a distorted, arc-like shape to the north. The velocity fields from H_2 (b) and $\text{Pa}\alpha$ (d), however, are aligned and show very regular rotation about the centre (NIR-peak). The velocity dispersion (only shown for $\text{Pa}\alpha$, f) peaks on the kinematic/NIR centre and is extended perpendicular to the kinematic major axis, most likely as a result of beam smearing.

The Kinemetry model fits the $\text{Pa}\alpha$ velocity field very well, the residual map shows no structure and has very low values. The resulting rotation curve has a maximum (inclination corrected) value of ~ 215 km/s, it turns over at 0.7 kpc and stays flat at least out to a radius of 2.5 kpc. Because of the flat shape, instead of declining, this curve could not be fitted with a Hernquist potential alone and a substantial exponential disk component is inescapable. The resulting effective radius is 1.6 kpc, while literature (H -band) values range from 1.0 kpc in Genzel et al. (2001) to 2.16 kpc in Dasyra et al. (2006). The total dynamical mass inside the outer radius reached of 2.4 kpc was calculated to be $2.21 \cdot 10^{10} M_\odot$, with a gas fraction of 0.46 on this scale. Unfortunately, in this object no molecular gas measurement is available for checking this number. The disk component is however quite obvious in the $\text{Pa}\alpha$ image, which is much more extended than the K -band continuum, and shows a prominent feature that may be interpreted as a spiral arm. Without an independent molecular gas mass measurement we cannot verify whether this disk is indeed mostly gaseous, but K -band light profile is very well fit by a De Vaucouleurs law (Genzel et al. 2001). We note however that because of the relatively high redshift of this object, the physical field of view is large and the rotation curve was measured out to a larger physical radius than in the other objects, in particular significantly beyond R_{eff} . Restricting the calculation to the region within R_{eff} would result in a smaller gas/stellar mass ratio, since the fits to the rotation curve (Fig. 5.3) show that the bulge component is more important in the central part and the gas fraction within the effective radius is smaller. The value of M_{dyn}/L_K is $0.02 M_\odot/L_{K,\odot}$, and M_*/L_K is $0.01 M_\odot/L_{K,\odot}$.

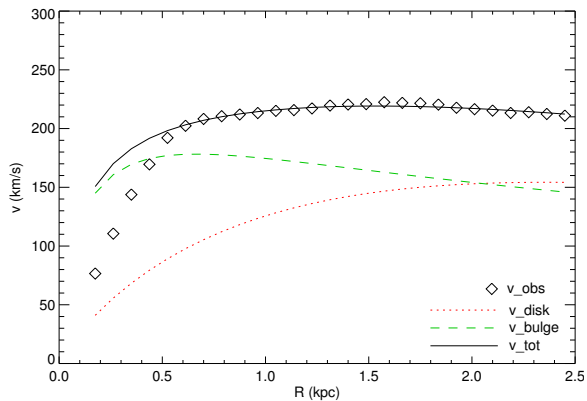


Figure 5.3 – IRAS 01388-4618 gas rotation curve of $\text{Pa}\alpha$.

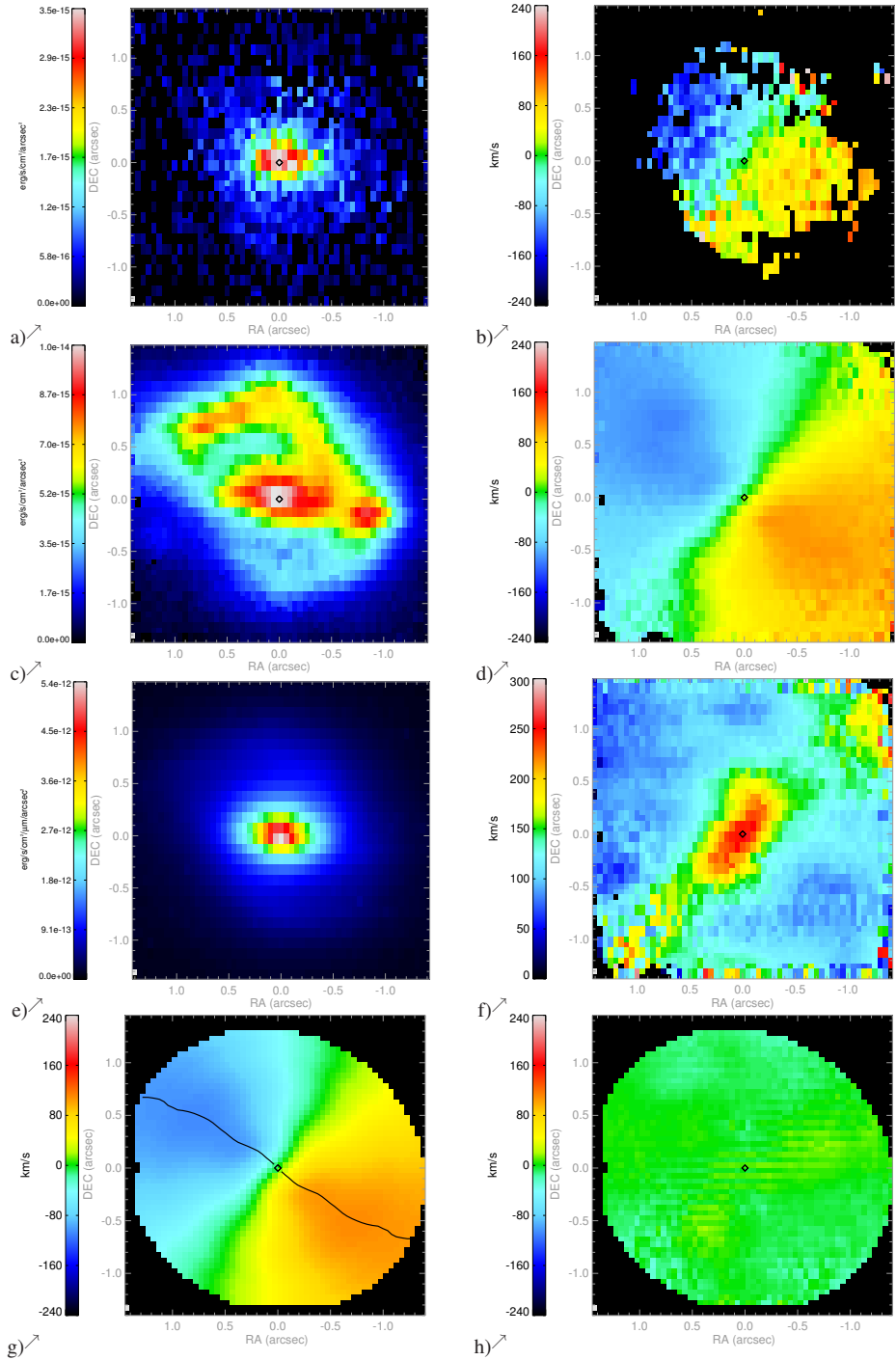


Figure 5.2 – IRAS 01388-4618 ($f_{25}/f_{60}=0.12$; $1'' \pm 1.79\text{kpc}$): a) H₂ flux; b) H₂ velocity; c) Pa α flux; d) Pa α velocity; e) K-band continuum; f) Pa α velocity dispersion; g) velocity model of Pa α and h) residual map. The diamond (◊) marks the peak of the K-band continuum, which we use as the kinematic centre by definition.

5.3.5 IRAS 05189-2524

This is a well known, well studied object, and with f_{25}/f_{60} of 0.26, it is the only ULIRG in our sample that qualifies as “warm” ($f_{25}/f_{60} > 0.2$). The spectrum (Fig. 5.1, upper right) shows Pa α , but not as prominent as in the rest of the sample. Emission lines of excited H₂ are recognised but lines are not prominent in general. This spectrum is the only one with rising K -band continuum, which indicates the presence of hot dust associated with the AGN. Stellar CO-absorption bands are hardly detected. Figure 5.5 shows a compact source in H₂, Pa α and K . The velocity field is more regular in H₂ (b), than in Pa α (d) and the velocity dispersion of Pa α (f) shows a clear peak on the centre location. Since the outer velocity field is noisy, only the very central part of the velocity field is used for modelling, as shown in the bottom panel.

The Pa α kinematics in this object is strongly affected by the broad line associated with the AGN. The derived velocity field of Pa α does not match that of H₂, and is less regular, and based on these arguments, the H₂ velocity map is a better choice for analysing the gravitational dynamics. Because of the compactness of this source, only a small part of the field of view can be used for the Kinemetry-fit. Within this small region, however, the residual map is quite smooth, although the low values are not very low compared to the measured velocities. This warm ULIRG has a face-on orientation with literature values for the inclination of ~ 20 - 30° . The inclination used in the velocity model is 22° , but we point out that the error margin on this value has large effects on the derived parameters. Since only the inner region of the system can be analysed, no attempt has been made to make a combined bulge+disk fit and the curve is fit with a Hernquist (bulge) potential only. This spheroid has an effective radius of 0.35 kpc and a total mass of $1.05 \cdot 10^9 M_\odot$. Dasyra et al. (2006) find an effective radius in K -band of 0.79 kpc. The dynamic/bulge mass within $R_{\text{out}}=0.34$ kpc then is $5.16 \cdot 10^8 M_\odot$. The stellar mass-to-light ratio M_*/L_K is $0.003 M_\odot/L_{K,\odot}$, which is the same as the value of the M_{dyn}/L_K stated in Table 5.3 because only a bulge component was fit to the rotation curve. Besides the extinction correction, a 55% for the AGN component was subtracted in determining L_K , as described in more detail in Chapter 4.

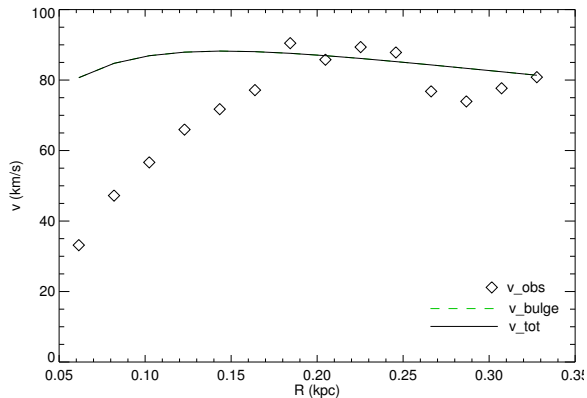


Figure 5.4 – IRAS 05189-2524 gas rotation curve of H₂.

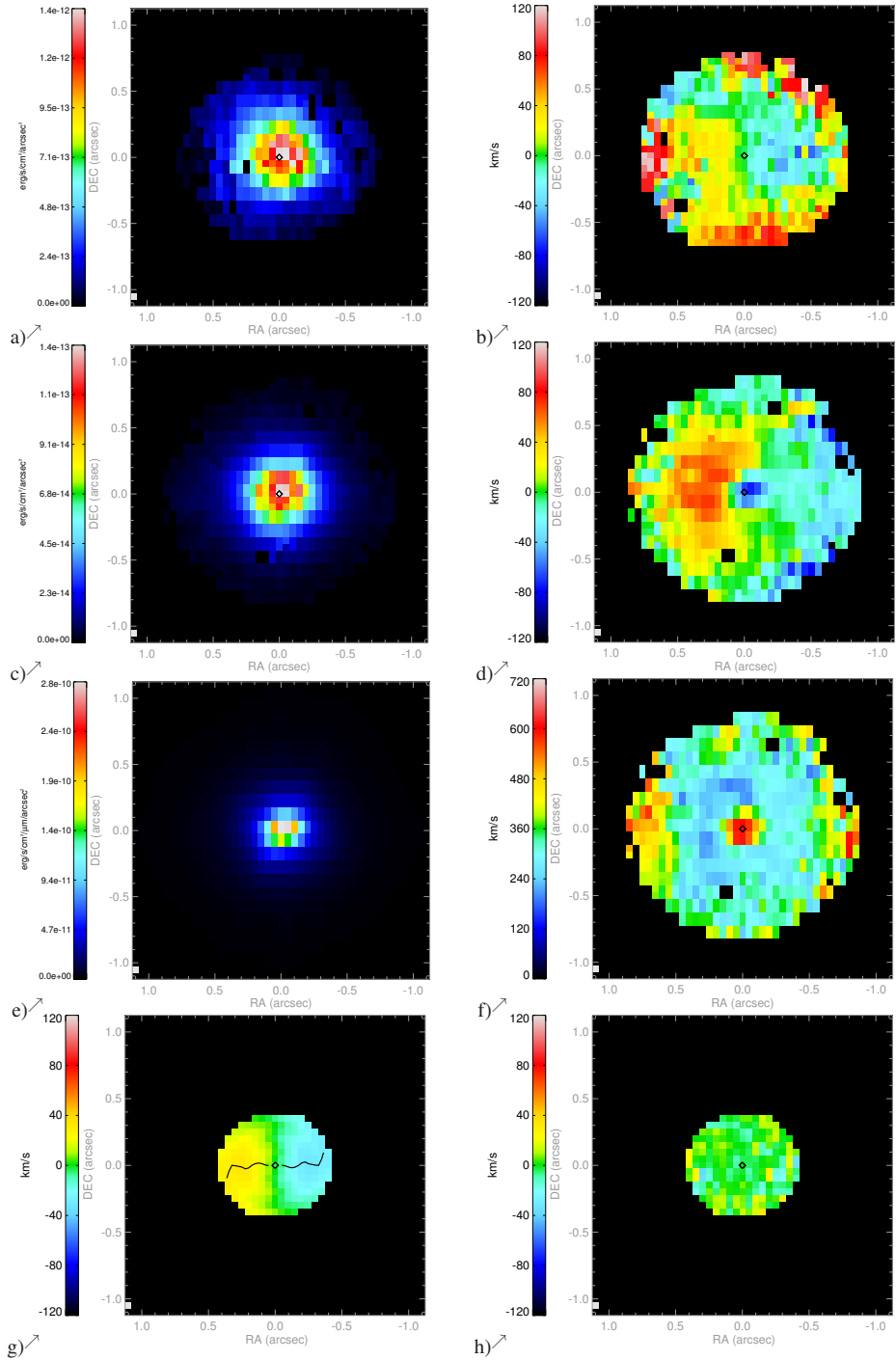


Figure 5.5 – IRAS 05189-2524 ($f_{25}/f_{60}=0.26$; $1''\approx 0.84$ kpc); a) H₂ flux; b) H₂ velocity; c) Pa α flux; d) Pa α velocity; e) *K*-band continuum; f) Pa α velocity dispersion; g) velocity model of H₂ and h) residual map.

5.3.6 IRAS 09111-1007

In the spectrum of this cool ULIRG ($f_{25}/f_{60}=0.11$), the high excitation [SiVI] line is detected, which denotes the presence of an AGN (Fig. 5.1, middle). The morphology of H₂, Pa α and K (Fig. 5.7) is centrally concentrated in a similar way. These maps are all extended in northeast-southwest direction, aligned with the axis of rotation (velocity field, Fig. 5.7b,d), although the H₂ extension and rotation axis seems to be tilted with a slightly different angle. The velocity dispersion map of Pa α (f) is distorted and peaks north, with a dip directly to the south-west of the NIR/kinematic centre. The velocity map of Pa α is used for modelling, but the seemingly symmetric deviations of the rotation axis are not modelled properly, leaving higher residuals on the edges (g) and (h).

The velocity field of Pa α is not symmetric, as can be seen in the residual map of the fit. It should also be noted that the minimum in the blueshifted part does not have a clear corresponding maximum in the redshifted part in the observed Pa α velocity map. These details should be kept in mind when inspecting the fit to the rotation curve, which appears to be satisfactory. The inclination used was 38°. The curve was fit with bulge and a disk components, with resulting values R_{eff} of 2.3 kpc and M_{tot} of $3.44 \cdot 10^{10} M_{\odot}$ for the bulge, and h of 0.5 kpc and Σ_0 of $4.0 \cdot 10^3 M_{\odot} \text{pc}^{-2}$ for the exponential disk. The outer radius R_{out} is 1.05 kpc, and $M(R_{\text{out}})$ is $1.34 \cdot 10^{10} M_{\odot}$. The gas fraction within this radius is 0.29, and the gas mass would be $M = 3.6 \cdot 10^9 M_{\odot}$. This is in excellent agreement with the gas mass $M = 3.1 \cdot 10^9 M_{\odot}$ derived for this object by Chung et al. (2009) using CO 1–0 data. The resulting value of M_{dyn}/L_K is $0.02 M_{\odot}/L_{K,\odot}$, and M_*/L_K is $0.015 M_{\odot}/L_{K,\odot}$ for the stellar component. The contribution of the AGN in IRAS 09111-1007 is estimated to be negligibly small in the near-IR (Farrah et al. 2003).

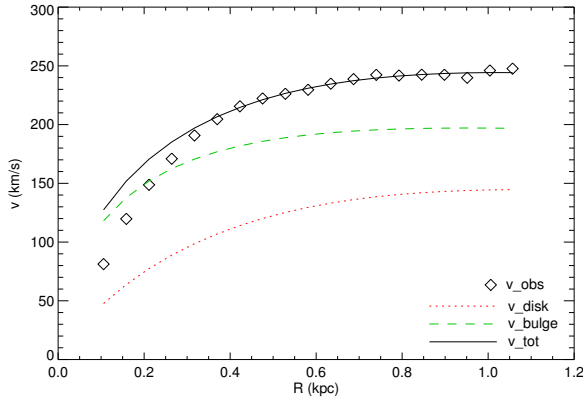


Figure 5.6 – IRAS 09111-2524 gas rotation curve of Pa α .

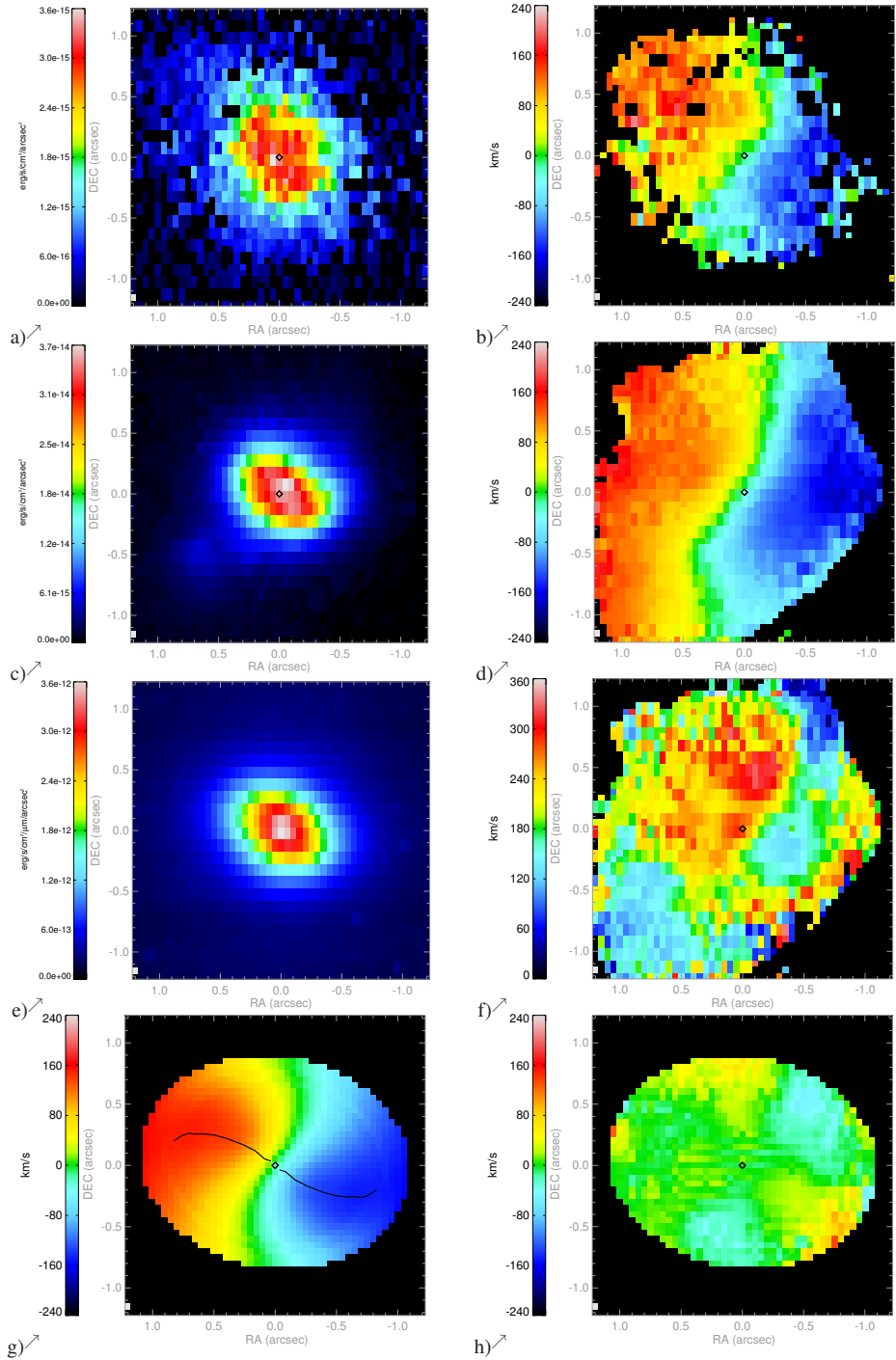


Figure 5.7 – IRAS 09111-1007 ($f_{25}/f_{60}=0.11$; $1'' \approx 1.07\text{kpc}$); a) H₂ flux; b) H₂ velocity; c) Pa α flux; d) Pa α velocity; e) *K*-band continuum; f) Pa α velocity dispersion; g) velocity model of Pa α and h) residual map.

5.3.7 IRAS 17208-0014

This is the ‘coolest’ ULIRG of the sample, with f_{25}/f_{60} of 0.05, while it is also the most luminous in the infrared. The distribution and peak locations of H_2 , Pa α and K are all slightly different (Fig. 5.9). The velocity fields of H_2 (b) and Pa α (d) show minor differences, while the peak of the velocity dispersion (f) is clearly displaced to the south of the K -band peak. The Pa α velocity field was used for modelling (g), and the kinematic centre had to be shifted to the south-east with respect to the K -band peak centre. The resulting rotation curve in Fig. 5.8 shows very rapid rotation (implying a very massive system), and a declining shape beyond 0.35 kpc. A higher inclination would result in a lower derived rotation velocity, formally by at most a factor 2 (for inclination 90°). However, a very edge-on orientation is ruled out by the observed morphology of both the stellar and the gaseous components, based on our data as well as high resolution CO data (Downes & Solomon 1998). So while an underestimated inclination could play a role in producing the very high derived rotation velocity, it will certainly not explain it fully, and this is certainly a rapidly rotating, and therefore massive system.

The velocity fields of H_2 and Pa α have slightly different features, but in both the kinematic centre seems to be shifted to the south, with respect to the K -band peak. The redshifted and blueshifted peaks in the Pa α velocity map are not exactly symmetric, which is seen in the residual map, though the residuals are not high compared to the measured velocities. The used inclination was 28° , based on the CO interferometry of Downes & Solomon (1998). The resulting rotation curve declines after the turnover-point at 0.35 kpc. If only fitted with a Hernquist potential, the effective radius needed to establish this shape would be very small, of the order of 0.05 kpc. The gas component is essential to make a reliable fit. In this case, the mass of the gas disk could be constrained with CO-data from Downes & Solomon (1998). The scale length $h=0.46$ kpc was derived from the gas mass difference between their observed radii of $R_{\text{out}}=1.5$ kpc and $R_{\text{in}}=0.54$ kpc and the mass surface density $\Sigma_0 = 5.5 \cdot 10^3 M_\odot \text{pc}^{-2}$ was calculated accordingly. The spheroid component was then fitted with R_{eff} of 0.54 kpc and M_{tot} of $6.35 \cdot 10^{10} M_\odot$. The outer radius R_{out} is 1.05 kpc, and $M(R_{\text{out}})$ is $1.34 \cdot 10^{10} M_\odot$. The gas fraction within this radius is 10%. M_{dyn}/L_K is $0.43 M_\odot/L_{K,\odot}$, and M_*/L_K is $0.38 M_\odot/L_{K,\odot}$.

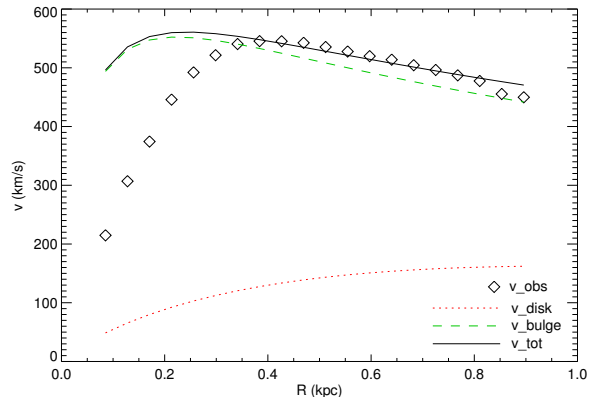


Figure 5.8 – IRAS 17208-2524 gas rotation curve of Pa α .

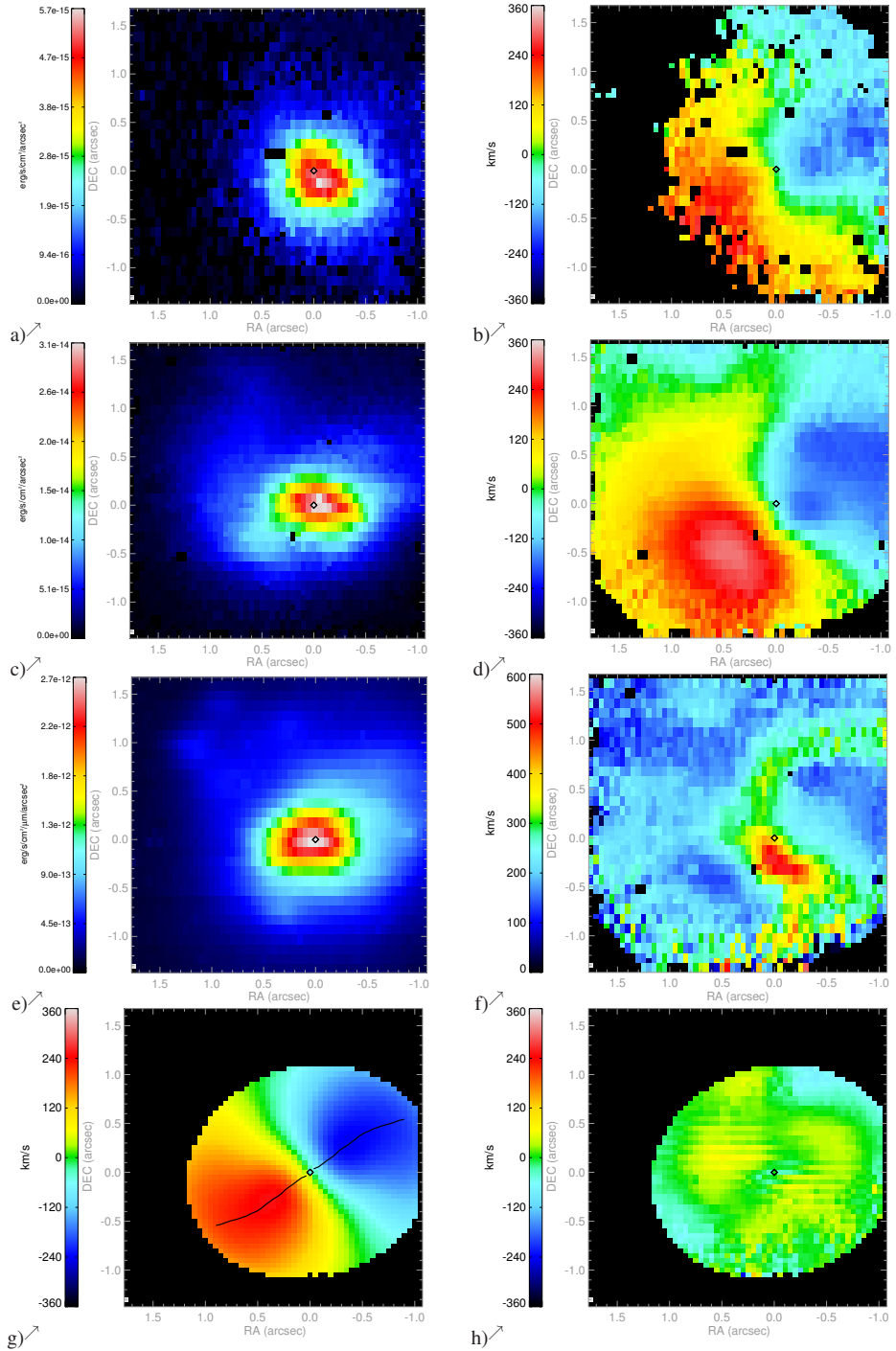


Figure 5.9 – IRAS 17208-0014 ($f_{25}/f_{60}=0.05$; $1'' \approx 0.86\text{kpc}$); a) H₂ flux; b) H₂ velocity; c) Pa α flux; d) Pa α velocity; e) *K*-band continuum; f) Pa α velocity dispersion; g) velocity model of Pa α and h) residual map.

5.3.8 IRAS 20551-4250

Regarding its infrared colours ($f_{25}/f_{60}=0.15$), this is a moderately warm ULIRG. The source is quite compact in H_2 , Pa α and K (Fig. 5.11). Only the relatively faint emission shows some structure, a tail towards the south-east in H_2 , and extension to the north and west in Pa α . The velocity fields of H_2 (b) and Pa α (d) show little rotation, and although it seems regular in H_2 , it is more likely that this velocity field has the same distortions as the Pa α . The velocity dispersion (f) is very distorted with dips and peaks, a dip on the NIR centre location. An attempt has been made to make a model of the Pa α velocity field (g,h), but it only models part of the field and it is not clear that the assumed rotation axis (with the highest gradient in the complex Pa α velocity field) should be correct.

As mentioned above, the velocity field is not regular though part of it seems to show rotation about the centre (centres of H_2 , Pa α and K do coincide, however). Also, the fitted region does not extend to the location where the minimum (blueshifted) velocity is reached (which does not have a maximum/redshifted counterpart). The part that *is* fitted, does not have large values in the residual map (h), but a hint that the minimum velocity is not included can be seen in the southwest. The inclination used was 36° . A combined fit to the rotation curve (Fig. 5.10) was made with a spheroid component with ($R_{\text{eff}}=1.5$ kpc and M_{tot} of $5.75 \cdot 10^9 M_\odot$) and a disk component with ($h=0.35$ kpc and $\Sigma_0 = 9.0 \cdot 10^2 M_\odot \text{pc}^{-2}$). The total dynamical mass within 1.5 kpc is then $2.52 \cdot 10^9 M_\odot$, with a gas fraction of 20%. The value of M_{dyn}/L_K is $0.05 M_\odot/L_{K,\odot}$, and M_*/L_K is $0.04 M_\odot/L_{K,\odot}$.

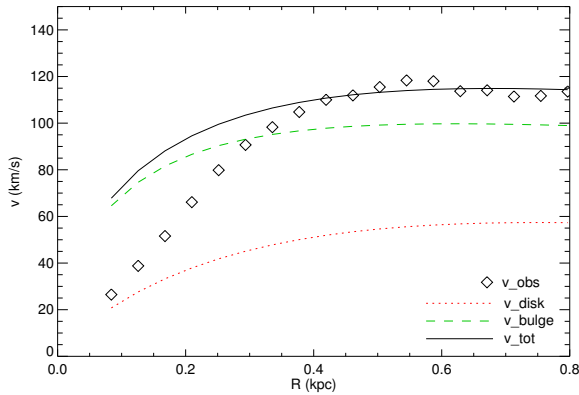


Figure 5.10 – IRAS 20551-4250 gas rotation curve of Pa α .

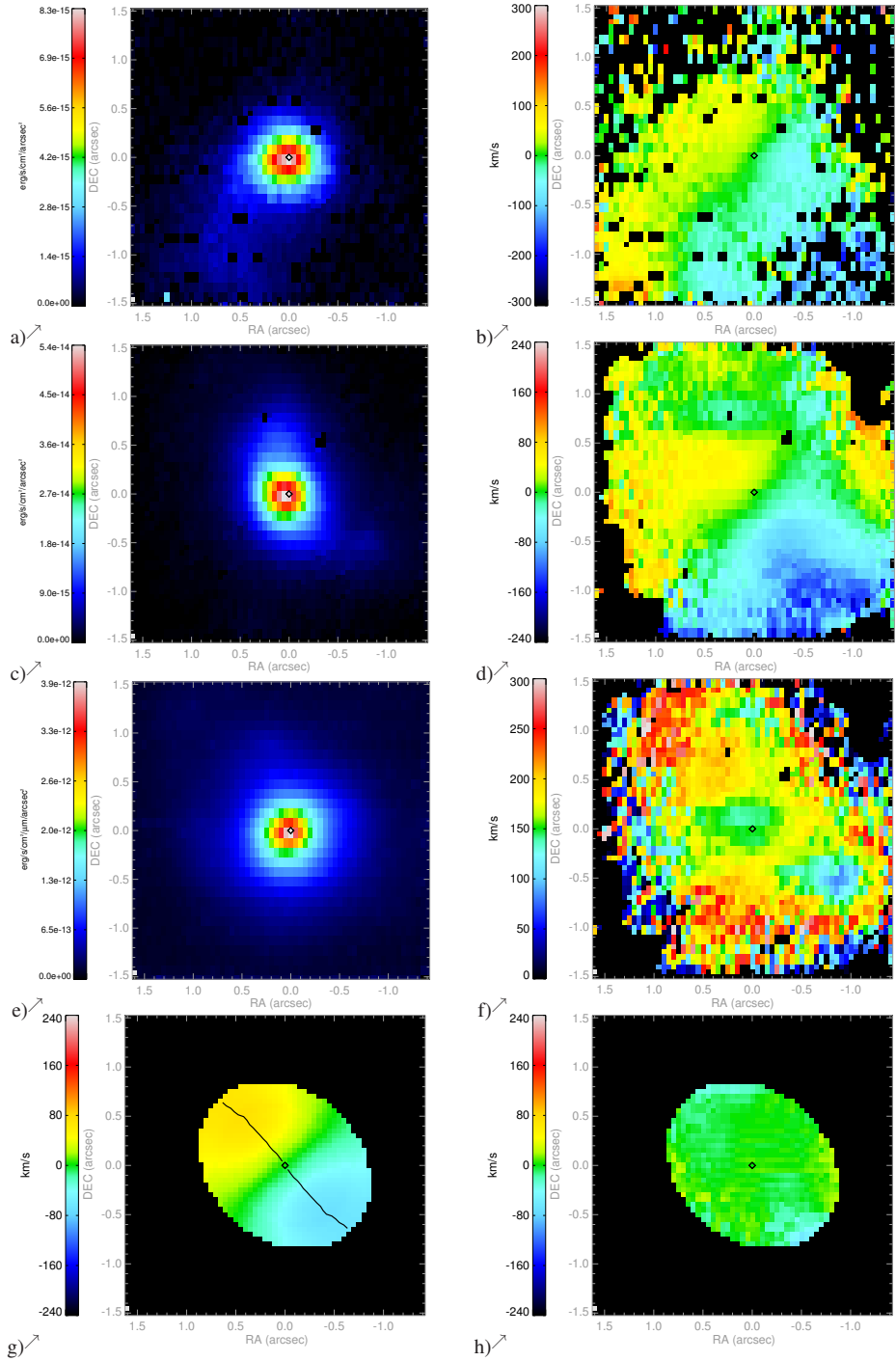


Figure 5.11 – IRAS 20551-4250 ($f_{25}/f_{60}=0.15$; $1'' \approx 0.86 \text{ kpc}$); a) H₂ flux; b) H₂ velocity; c) Pa α flux; d) Pa α velocity; e) K-band continuum; f) Pa α velocity dispersion; g) velocity model of Pa α and h) residual map.

Table 5.3 – Mass and luminosity within the SINFONI-field of view.

Name	R_{out} (kpc)	M_{gas}	M_*	M_{dyn}	$M_{\text{gas}}/M_{\text{dyn}}$	L_K	M_{dyn}/L_K	M_*/L_K	$M_{\text{dyn}}^{(*)}$	$M_*/L_K^{(*)}$
(1)	(2)	(3)	(4)	(5)	(6)	(7)	(8)	(9)	(10)	(11)
		$(10^{10} M_{\odot})$	$(10^{10} M_{\odot})$			$(10^{10} L_{K,\odot})$	$\left(\frac{M_{\odot}}{L_{K,\odot}}\right)$		$(10^{10} M_{\odot})$	$\left(\frac{M_{\odot}}{L_{K,\odot}}\right)$
IRAS 01388-4618	2.4	1.0	1.2	2.2	0.46	108	0.02	0.01	6.0 ± 1.0	0.03 ± 0.01
IRAS F05189-2524	0.34	-	0.052	0.052	-	17.5^a	0.003	0.003	0.87 ± 0.25	0.05 ± 0.02
IRAS F09111-1007	1.1	0.4	0.95	1.3	0.29	63.6	0.02	0.015	1.8 ± 0.7	0.02 ± 0.01
IRAS F17208-0014	1.0	0.47	4.2	4.7	0.10	11.0	0.43	0.38	3.3 ± 1.6	0.27 ± 0.16
IRAS F20551-4250	0.9	0.050	0.20	0.25	0.20	5.62	0.05	0.04	1.9 ± 1.4	0.27 ± 0.21
Arp 220	0.6	0.50	0.70	1.19	0.42	9.01	0.13	0.08	1.2 ± 0.4	0.05 ± 0.02

(*) Note: errors for the derived masses are not stated here, but the effect of the uncertainties are discussed in the text instead (Sections 5.3.3 and 5.4.2). Columns: (2) R_{out} is the major axis length of the outer ellipse of the Kinemetry-fit within the SINFONI field of view. All quantities of M_{dyn} , L_K and M/L_K in this table are calculated within R_{out} . (3) Mass of the gas (exponential disk) component within R_{out} . (4) Mass of the stellar (bulge) component within R_{out} . (5) Total dynamic mass (gas+stars) within R_{out} . (6) Gas mass fraction. (7) L_K is the K -band luminosity within R_{out} , corrected for extinction, expressed in solar K -band luminosities ($M_{K,\odot}=3.28$). The error in L_K is $\sim 20\%$, based on the error in L_K (uncorr) and the extinction correction. (8) M_{dyn}/L_K within R_{out} . (9) M_*/L_K within R_{out} , using only M_b . (10), (11) M_{dyn} and M_*/L_K from stellar kinematics (Chapter 4) in the same the same region, for comparison with columns (5) and (9), respectively.

^a For L_K , a component of 55% has been subtracted for the AGN. The error estimate in L_K of IRAS 05189-2524 is 30%.

5.4 Discussion

5.4.1 Rotation curve fitting and the role of the effective radius, R_{eff}

The effective radius is commonly defined as the radius within which half of the light is contained. However, using this definition the effective radius is known to vary with the wavelength of observation (e.g., Temi et al. 2008). This is also discussed in Chapter 4 (Sect. 4.3.1 and 4.4.1), where the effective radius is important in the calculation of the dynamical mass from stellar kinematics: the total mass scales linearly with R_{eff} . When fitting the rotation curve from gas kinematics, the effective radius is one of the free parameters in the Hernquist potential that constrains the bulge component. We consider this a mass-based effective radius: the mass-to-light ratio is assumed constant, and R_{eff} should in practise be equal to the half-mass radius. The effective radius of the bulge fit is important for the shape of the rotation curve, especially in the outer parts. A declining or flat rotation curve needs a bulge with a small enough effective radius; the scale-length h only has a limited effect and the curve of a purely exponential disk potential only rises. In general, the relative importance of bulge and disk is degenerate, but we try to put constraints on the gas disk e.g. from detailed CO gas measurements, such as in Arp 220 and IRAS 17208-0014. Because literature values of R_{eff} from K -band or H -band imaging can vary greatly between H -band and K -band, and between different observations in the same band as well (compare e.g., Dasyra et al. 2006, Genzel et al. 2001, Scoville et al. 2000, Veilleux et al. 1999), it is difficult to state what is the effect of our approach, although most of the mass-based effective radii are smaller than their K -band or H -band derived counterparts. It is no surprise that the effective radius of the compact source IRAS 05189-2524 is small (0.35 kpc), while the value of IRAS 17208-0014 (0.54 kpc) is much more surprising, compared to 1.4 kpc from Genzel et al. (2001) and 2.6 kpc from Scoville et al. (2000). However, for this target the possible range of R_{eff} was very small because of the declining shape of the, in this case, well defined rotation curve and the gas mass constrained by CO-observations of Downes & Solomon (1998). The value of IRAS 20551-4250 (1.5 kpc) is smaller than the 2.1 kpc determined by both Genzel et al. (2001) and Rothberg & Fischer (2010), but the observed velocity field shows structure that could not be incorporated in the Kinemetry fit and the rotation curve can not be considered reliable. As mentioned before, high extinction values ($A_K \sim 5$, $A_V \sim 50$ for a foreground screen model, or higher) can be expected in the central nuclear regions of ULIRGs which can cause the effective radius to appear larger, even in the K -band where its value is minimum (Temi et al. 2008). Another cause that can affect the observed effective radius is incomplete relaxation, i.e. the stellar components of the objects that are approximated with bulge models, are in fact not spherically symmetric. This affects our approach as well as the fitting of light-curves.

5.4.2 Mass from gas dynamics vs. mass from stellar dynamics

Dynamical masses were also derived from stellar kinematics (σ_* , v_*) from the same dataset, as described in Chapter 4. The derived masses and mass-to-light ratios for the same regions

are stated in columns (10) and (11) of table 5.3, respectively, which can be compared to columns (5) and (9) directly. Except for IRAS 17208-0014, all mass-to-light ratios (masses) derived from the gas kinematics in this work are smaller than those from stellar dynamics. As discussed in Sect. 5.3.3, a major factor in the error of the rotation curve and the derived mass is the inclination. The inclination affects both the mass from gas dynamics and from stellar dynamics, but in different ways: in the stellar dynamics the velocity dispersion σ_* is the dominant factor. Although we do not give an error for the inclination, we did define a plausible inclination-range as given in Table 5.2. We tested if it is possible to match the masses from stellar and gas kinematics within the limiting values of the inclination (assuming in all cases the same inclination for the stellar and gaseous components). This is indeed the case for 3 of the ULIRGs: IRAS 09111-1007, IRAS 17208-0014 and Arp 220, which is also reflected by the fact that the masses from gas dynamics are already within the error margins of the masses from stellar dynamics. For the discrepancy in masses of the other objects, we require different explanations.

In IRAS 20551-4250, a significant part of the gas velocity field (Fig. 5.11b,d) is irregular and disturbed, and even in the direct vicinity of the nucleus where it does show rotation, the minimum values do not have corresponding maximum counterparts. This causes the Kinemetry-fit to stop at a small radius, resulting in a model velocity field that does not represent the actual velocity field well. The stellar kinematics, on the other hand, were derived with good accuracy but even with high error margins they do not come close to the gas dynamics. From this we conclude that the mass from stellar kinematics is the best estimate, whereas the mass from gas dynamics is unacceptably unreliable, since the gas velocity field is not sufficiently accurately represented by our tilted ring model.

In IRAS 05189-2524, the mass difference is quite large, a factor of 17. An interesting finding is that the stars rotate faster than the H_2 gas. The stellar kinematics are only measured for a radius of $\sim 0.4''$ and outwards, while the gas velocity (model) is only derived within a similar radius (Fig. 5.5g), but there is an overlap between the measured velocity fields and furthermore the stellar velocities do not change much towards the outer regions. We conclude that, even though the position angles of the stellar and gas velocity fields are roughly aligned, the kinematics are decoupled, i.e., they have different inclinations, which is not an unexpected observation in an advanced merger remnant. In this case, the gas would be more face-on than the stars.

The mass difference in IRAS 01388-4618 is not very large, a factor of 2.7 which can be brought down to a factor of 1.8 within the error and inclination limits. For this object we did not have 2-d stellar kinematics because of the large redshift, and we used the values for (v_*, σ_*) of Dasyra et al. (2006) that were derived from slit data. We note that their slit position angle of 55° does match that of the kinematic major axis of the gas in our data (56° , table 5.2), so that the comparison is valid. We have already noted the extended nature of the Pa α disk, including a prominent feature that is probably a spiral arm. However, the (total) dynamical mass from the gas kinematics will not be affected too much and we consider this mass to be the more reliable. The value of M_*/L_K is then likely to lie between $0.01-0.02 M_\odot/L_{K,\odot}$, given that the disk likely contains a stellar component as well.

With the stellar and gas kinematic data in hand we can ask the question which one pro-

vides a better dynamical mass tracer. Even based on our limited sample, we have to conclude that the stellar kinematics provide a better measurement. In both measurements the inclination of the rotating system (whether stars or gas) is the dominant source of uncertainty, but for the stars its importance is offset by the effects of the stellar velocity dispersion in these dynamically hot systems. However, even if the inclination could be reliably measured (which is possible using sufficiently accurate and high S/N data), the stellar dynamics still performs better, since in many objects the gas does not appear to have settled in a simple dynamical configuration that can be adequately modelled by a set of tilted rings. In contrast, the stellar components seem to be, within the accuracy of our measurements, dynamically fairly relaxed. This is a somewhat surprising result, since the gas components are dissipative, leading to a rapid merging and loss of memory of its former dynamical properties, while the stellar component would merge on longer timescales due to dynamical friction. Apparently a process of rapid relaxation gives rise to dynamically well-behaved stellar cores, supported by rotation and random motions. It is possible that deeper measurements would reveal traces of unrelaxed dynamics, but at the S/N ratio of our data such traces are not found.

5.4.3 ULIRG evolution: starburst ages and mass fractions

Despite the differences mentioned in the section above, the fact that there is no trend of M/L_K with f_{25}/f_{60} is a confirmation of the result from stellar dynamics (Chapter 4). The ages derived from a starburst model for the most plausible value of M_*/L_K range from ~ 10 Myr for IRAS 01388-4618, IRAS 09111-1007 and probably also for IRAS 05189-2524 to ~ 15 Myr for Arp 220 and ~ 100 Myr for IRAS 17208-0014 and IRAS 20551-4250 (see Chapter 4, section 4.3.1 for a description of the model). These values are consistent with those in Chapter 4, and likewise we confirm the conclusion that these merging galaxies undergo several burst events: one at their first encounter and again when they finally merge, while M/L_K only indicates the age of the most recent merging event.

The gas fractions derived from the rotation curve fit, within the observed radius R_{out} , range from 10% to 50% (no estimate for IRAS 05189-2524). This range is in agreement with the values found by e.g. Tacconi et al. (2002). The gas fraction of 50% found in IRAS 01388-4618 may be somewhat overestimated (see Sect. 5.4.2), but even with this 50% included, the overall gas component is not dominant in these objects. In the possible evolutionary path from ULIRGs to ellipticals, the gas is consumed and the gas fraction is expected to decrease with evolutionary state. No such (anti)correlation is found between infrared colour f_{25}/f_{60} and gas fraction, but because of the limited size of our sample we do not attach significance to this result.

5.4.4 ULIRG evolution: the fundamental plane

With our data, it is possible to pinpoint the location of ULIRGs with respect to the Fundamental Plane to find out if and in what way it is related to the location of (giant) elliptical galaxies and bulges.

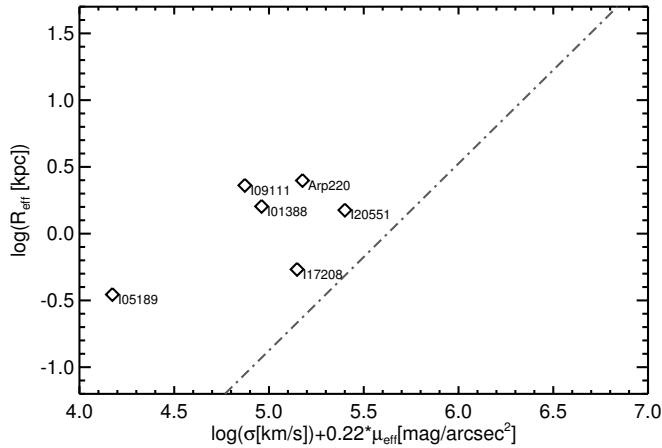


Figure 5.12 – Location of the sample ULIRGs with respect to fundamental plane. The dot-dashed line indicates the location of a projection of the fundamental plane of hot galaxies: it is the best-fit slope from K -band studies of Mobasher et al. (1999) and Pahre (1999): $\log r_{\text{eff}} = 1.4[\log \sigma + 0.22\mu_{\text{eff}}(K)] + \text{const}$, as fitted to the data of Genzel et al. (2001) and Tacconi et al. (2002).

We use the effective radius as derived from the bulge-fit, which should better match the properties of elliptical galaxies, because these do not suffer from the high extinction as is supposed to be the case in ULIRGs, see also Sect. 5.4.1. Next, we calculated μ_{eff} , the extinction corrected value of the K -band surface brightness within R_{eff} . When R_{eff} was outside of our field of view, μ_{eff} was determined by extrapolation, assuming a Hernquist bulge for the light profile (and assuming constant M/L):

$$L_K(R_{\text{eff}}) = \frac{(R_{\text{max}} + a)^2}{(R_{\text{eff}} + a)^2} \left(\frac{R_{\text{eff}}}{R_{\text{max}}} \right) \cdot L(R_{\text{max}}),$$

which is derived directly from the relation $M(r) = M_{\text{tot}} \frac{r^2}{(r+a)^2}$ and $a = R_{\text{eff}}/\sqrt{2}$ from Hernquist (1990). The stellar velocity dispersion (σ_*) was derived in Chapter 4. Fig. 5.12 shows the ULIRGs in a specific projection of the fundamental plane with the least scatter as in Genzel et al. (2001), Tacconi et al. (2002), Dasyra et al. (2006). Our ULIRGs are all located to the left of this particular projection of the fundamental plane, which can be explained entirely by the fact that they all have lower K -band M/L ratios than quiescent ellipticals, and is in agreement with earlier work (e.g., Genzel et al. 2001, Tacconi et al. 2002, Dasyra et al. 2006). Passive evolution (with no evolution in structural properties) would move these objects to the right where they eventually would lie on the fundamental plane. They would however not lie in the region of giant ellipticals (which have larger effective radii), but in the region of intermediate mass (and luminosity) ellipticals, and this conclusion is even stronger than the conclusion from earlier work (Genzel et al. 2001, Tacconi et al. 2002, Dasyra et al. 2006), due to the somewhat smaller R_{eff} found for most of our targets. Therefore we find that ULIRGs

do not evolve into massive giant ellipticals but into intermediate mass and luminosity ellipticals, unless further *dynamical* evolution would lead to higher values of R_{eff} . This is not totally out of the question, given the fact that many of these objects are still in the process of merging, and complex configurations were found in particular in the gas dynamics. Detailed simulations of gas-rich star-forming mergers are needed to address this issue in more detail.

5.5 Conclusions

We have observed the central regions of 6 ultraluminous infrared galaxies with high resolution near infrared integral field spectroscopy. We derived the velocity fields from Pa α and H₂ and modelled the rotation curve with a stellar and a gas component, and derived K -band mass-to-light ratios within the field of view. These were compared with mass-to-light ratios from stellar kinematics from the same dataset. We draw the following conclusions.

1. Stellar mass-to light ratios are generally smaller as derived from gas kinematics as compared to those from stellar kinematics, but they are consistent taking into account the uncertainties of the inclination, which forms the dominant source of uncertainty in the derived parameters.
2. There is no trend of M/L_K with infrared colour f_{25}/f_{60} , which is confirmed by the stellar kinematics.
3. The effective radius is an important factor in the mass-determinations both in gas and stellar kinematics. R_{eff} is generally smaller when derived from the bulge potential than when derived from the K -band lightcurve. We ascribe this to high extinction in the nuclear region.
4. We confirm earlier findings that, in the fundamental plane, ULIRGs are not evolving into giant ellipticals. The difference in effective radius with giant ellipticals is a factor of 3 in our study, which is beyond the error margins and even higher than previous studies.
5. We find that the gas velocity fields are considerably affected by bulk motions and asymmetries, most likely resulting from the merger nature of our targets. These motions cannot be modelled using tilted ring models, and this limits the power of gas dynamics for analysing the gravitational dynamics. The stellar dynamics seem comparably well-behaved and probably provide a cleaner measurement of the dynamical masses of these systems.

References

- Bonnet, H., Abuter, R., Baker, A., et al. 2004, *The Messenger*, 117, 17
Cappellari, M., Neumayer, N., Reunanen, J., et al. 2009, *MNRAS*, 394, 660
Chung, A., Narayanan, G., Yun, M. S., Heyer, M., & Erickson, N. R. 2009, *AJ*, 138, 858

- Dasyra, K. M., Tacconi, L. J., Davies, R. I., et al. 2006, *ApJ*, 651, 835
- Downes, D. & Solomon, P. M. 1998, *ApJ*, 507, 615
- Eisenhauer, F., Abuter, R., Bickert, K., et al. 2003, in *Proceedings of the SPIE, Vol. 4841, Instrument Design and Performance for Optical/Infrared Ground-based Telescopes.*, ed. M. Iye & A. F. M. Moorwood, 1548–1561
- Elmegreen, B. 1994, in *Violent Star Formation from 30 Dor to QSOs*, ed. T. G.
- Farrah, D., Afonso, J., Efstathiou, A., et al. 2003, *MNRAS*, 343, 585
- Ferrarese, L. & Merritt, D. 2000, *ApJ*, 539, L9
- Gebhardt, K., Bender, R., Bower, G., et al. 2000, *ApJ*, 539, L13
- Genzel, R., Tacconi, L. J., Rigopoulou, D., Lutz, D., & Tecza, M. 2001, *ApJ*, 563, 527
- Goldader, J. D., Joseph, R. D., Doyon, R., & Sanders, D. B. 1995, *ApJ*, 444, 97
- Hernquist, L. 1990, *ApJ*, 356, 359
- Krajnović, D., Cappellari, M., de Zeeuw, P. T., & Copin, Y. 2006, *MNRAS*, 366, 787
- Magorrian, J., Tremaine, S., Richstone, D., et al. 1998, *AJ*, 115, 2285
- Mobasher, B., Guzman, R., Aragon-Salamanca, A., & Zepf, S. 1999, *MNRAS*, 304, 225
- Neumayer, N., Cappellari, M., Reunanen, J., et al. 2007, *ApJ*, 671, 1329
- Pahre, M. A. 1999, *ApJS*, 124, 127
- Rothberg, B. & Fischer, J. 2010, *ApJ*, 712, 318
- Sanders, D. B., Mazzarella, J. M., Kim, D.-C., Surace, J. A., & Soifer, B. T. 2003, *AJ*, 126, 1607
- Sanders, D. B., Soifer, B. T., Elias, J. H., et al. 1988, *ApJ*, 325, 74
- Scoville, N. Z., Evans, A. S., Thompson, R., et al. 2000, *AJ*, 119, 991
- Tacconi, L. J., Genzel, R., Lutz, D., et al. 2002, *ApJ*, 580, 73
- Temi, P., Brighenti, F., & Mathews, W. G. 2008, *ApJ*, 672, 244
- Veilleux, S., Kim, D.-C., & Sanders, D. B. 1999, *ApJ*, 522, 113

Nederlandse samenvatting:

Spectroscopie en centrale dynamica van starburst-stelsels

1. Sterrenstels/melkwegstelsels (galaxies)

Een sterrenstelsel is een enorme verzameling van sterren, zo'n paar honderd miljard, die in een bepaalde vorm bij elkaar horen. Naast sterren bevatten deze stelsels ook (waterstof-)gas en stofdeeltjes. Onze Melkweg is ook een sterrenstelsel; daarom worden sterrenstelsels ook wel melkwegstelsels genoemd. Er zijn grofweg twee vormen: spiraalstelsels en elliptische stelsels.

Spiraalstelsels zijn opgebouwd uit een platte schijf van gas en sterren, waarbij de materie duidelijk in spiraalvorm geconcentreerd is, dit kunnen 2 of meer spiraalarmen zijn. Meestal bevat een spiraalstelsel in het midden ook een bolvorm met wat oudere sterren, terwijl nieuwe stervorming in de spiraalarmen plaatsvindt. De Melkweg is een spiraalstelsel. De zon met het zonnestelsel bevindt zich aan de buitenkant iets tussen twee spiraalarmen.

Elliptische stelsels hebben de vorm van een bol die meer of minder afgeplat is. Er vindt in elliptische stelsels minder stervorming plaats en ze zijn over het algemeen ouder dan spiraalstelsels. Een gangbare theorie stelt dat elliptische stelsels ontstaan door botsingen tussen spiraalstelsels, dit kunnen botsingen zijn tussen grote stelsels of tussen kleine stelsels, of een groot stelsel dat op zijn weg steeds kleine stelseltjes is tegengekomen.

De meeste sterrenkundigen zijn het erover eens dat deze stelsels naast sterren, gas en stof ook donkere materie moet bevatten, dit zou zelfs het grootste deel van hun massa uitmaken, zo'n 90%. De belangrijkste aanwijzing hiervoor is gebaseerd op de wetten van Newton: op een bepaald punt eindigt de zichtbare materie van een (spiraal-)stelsel, maar verder naar buiten wordt wel de invloed van massa (zwaartekracht) opgemerkt. Deze massa loopt zelfs ver door buiten het deel van het stelsel dat sterren bevat. Er zijn theorieën die dit (en andere verschijnselen) zonder donkere materie proberen te verklaren, maar die hebben tot nu toe geen bevredigende resultaten opgeleverd. Waar de donkere materie uit bestaat is nog onduidelijk.

2. Starburst-stelsels

Sterren worden gevormd uit koude wolken van waterstofgas, die ook stofdeeltjes bevatten. Meestal gebeurt dit in de spiraalarmen van spiraalstelsels op een rustig tempo van 1 zons-

massa (de massa van de zon) per jaar voor het hele stelsel. In het geval van een starburst-stelsel kan dit 10-100 zonsmassa's per jaar zijn, en in het geval van extreme starbursts wel 100-1000 zonsmassa's per jaar, zoals in de ULIRGs die hieronder worden beschreven. Bij deze mate van stervorming wordt het beschikbare gas in hoog tempo opgebruikt en daarom kan dit maar een beperkte tijd aanhouden, zo'n 10 miljoen tot 100 miljoen jaar. De stervorming in verhoogd tempo kan zich verspreid voordoen over het hele stelsel, maar meestal is het geconcentreerd in een relatief klein gebied van een paar honderd tot duizend lichtjaar rond de kern van het stelsel (ter vergelijking: de diameter van de Melkweg, het gedeelte waar zich sterren bevinden, is ongeveer 100.000 lichtjaar).

Een starburst wordt meestal veroorzaakt door de interactie met een ander sterrenstelsel. De directe aanleiding van de starburst is het botsen van gaswolken op elkaar, wat twee oorzaken kan hebben. Ten eerste kan het zo zijn dat de wolken binnen een stelsel onderling botsen omdat een naburig stelsel het zwaartekrachtveld zo verstoort dat hun beweging is veranderd. In het tweede geval zijn de twee sterrenstelsels daadwerkelijk op elkaar gebotst en komen de gaswolken van de één met die van de ander in botsing. In dit laatste, spectaculaire geval komt het zelden voor dat de *sterren* van de stelsels ook met elkaar botsen, omdat de afstanden tussen de sterren zo groot zijn, maar de sterren hebben wel grote invloed op het zwaartekrachtveld.

3. Dit proefschrift

Het doel van dit werk is inzicht verwerven in starbursts en de bijbehorende dynamische processen. De bestudering van het spectrum, de onderverdeling van het licht bij verschillende golflengtes, is hiervoor heel handig. Een spectraal-lijn betekent dat er bij een nauwkeurig bepaalde golflengte krachtig wordt uitgezonden. De golflengte waarbij dit gebeurt geeft de aanwezigheid van een specifiek element of specifieke stof aan, de sterkte van de lijn vertelt iets over de hoeveelheid van deze stof en de verschuiving in golflengte van de lijn geeft aan wat de snelheid is. Een aantal bekende lijnen in het spectrum geven verschillende stadia van stervorming aan: Brackett-gamma (een atomaire waterstoflijn) en heliumlijnen voor recente stervorming, ijzer voor supernova-resten en moleculair waterstof voor schokgolven of stervormingsgebieden. Aan de hand van spectra van starbursts, is duidelijk dat er behalve 'gemiddelde' sterren zoals de zon, ook hele grote, massieve sterren worden gevormd die zo'n $100\times$ zwaarder zijn dan de zon. Deze sterren zenden licht uit met veel energie in het ultraviolet (UV, korte golflengte), maar veel van juist dit licht wordt tegengehouden door stofkorrels die in grote hoeveelheden voorkomen in stervormingsgebieden. Deze stofkorrels absorberen dit ultraviolette licht, warmen daardoor op en zenden zelf weer licht uit met een langere golflengte die past bij hun temperatuur: in het infrarood. Tussen het ultraviolet en het infrarood ligt nog het optische gebied: het voor onze ogen zichtbare licht. In dit optische gebied, samen met het nabij-infrarood (een klein gedeelte van het infrarood dat daarbij aansluit) wordt licht waargenomen dat direct van sterren afkomstig is.

Met behulp van een techniek genaamd 'integral field'-spectroscopie is het mogelijk om waarnemingen te doen waarbij op elke pixel van het plaatje een spectrum beschikbaar is.

Hierdoor kan goed onderscheiden worden op welke locatie zich welke processen afspelen, en met twee-dimensionale snelheidsvelden kunnen bewegingen goed in kaart gebracht worden. Dit is een grote vooruitgang ten opzichte van de in het verleden veel gebruikte ‘slit’ spectroscopie. Hierbij worden spectra waargenomen door een spleet-vorm over het stelsel te leggen, waardoor ruimtelijke informatie verloren gaat of verborgen blijft. Voor de snelheidsvelden was het daarbij vaak moeilijk de richting en precieze snelheden te bepalen. Alle waarnemingen in dit proefschrift zijn gedaan met integral field spectroscopie, door gebruik van het instrument SINFONI (Spectrograph for INtegral Field Observations in the Near InfraRed), dat gemonteerd zit op één van de vier telescopen van de Very Large Telescope (VLT) op mount Paranal in Chili.

De spiegels van deze telescopen die het licht uit de ruimte opvangen hebben alle een diameter van 8.2 meter, en elke spiegel bestaat uit 150 beweegbare deeltjes. Deze losse delen zorgen ervoor dat de spiegel kan corrigeren voor verstoringen in de aardatmosfeer, waardoor de kwaliteit van de waarnemingen verbetert. Met behulp de Laser Guide Star, die sinds 2007 beschikbaar is op dezelfde telescoop als waar SINFONI aan vast zit, kan de kwaliteit met dit systeem nog verder worden verbeterd. Hiervoor wordt vanuit de koepel een zeer sterke laserstraal de lucht in gestuurd in de richting van het te observeren object. Deze straal reikt tot 90 km hoogte, waar hij zorgt dat het natrium dat zich daar bevindt licht uitzendt. Dit licht wordt weer waargenomen, en aan veranderde eigenschappen kan men zien welke verstoringen zijn opgetreden in de atmosfeer van de aarde. Deze informatie wordt razendsnel doorgegeven aan de beweegbare spiegeldeeltjes die direct van richting veranderen en corrigeren. Dit heet adaptieve optica (‘Adaptive Optics’). Hiervoor kan ook licht van een ster worden gebruikt, maar er is niet altijd een geschikte ster beschikbaar in de buurt van het te observeren object, en de Laser Guide Star biedt dan uitkomst.

Hoofdstuk 2: het starburst-stelsel M83 We selecteerden een spiraalstelsel met een starburst in de kern dat heel dichtbij staat (op een afstand van 15 miljoen lichtjaar): M83. Vanwege de nabijheid hebben we hoge resolutie en kunnen we verschillende processen in het kerngebied nauwkeurig in kaart brengen. Wat hierbij opvalt is dat de voornaamste starburst zich bevindt op een locatie die een stuk uit de buurt van het cluster van sterren dat werd geacht de kern van het stelsel te zijn (de optische piek). Supernova-resten, die aangeven waar stervorming in het verleden heeft plaatsgevonden, werden juist over het hele gebied verspreid aangetroffen. Wat betreft de dynamica komt het centrum van het snelheidsveld ook niet overeen met de optische piek. Het snelheidsveld van het gas laat een ronddraaiende gasring zien, terwijl de sterren in dit gebied weer een ander patroon volgen. Onze conclusie is dat deze starburst werd veroorzaakt door een algehele instabiliteit van het hele kerngebied.

Hoofdstuk 3, 4 en 5: Stelsels met extreme infrarood-straling (ULIRGs) *Ultraluminous infrared galaxies* (ULIRGs) vormen een klasse sterrenstelsels met de gezamenlijke eigenschap dat ze zeer helder zijn in het infrarood. Een stelsel is een ULIRG als hij minstens een infrarood-lichtkracht heeft die 1 biljard (10^{12}) keer zo sterk is als de zon. Maar deze stelsels blijken meer gemeen te hebben: bijna alle ULIRGs zijn het (eind)product van bot-

sende stelsels, ze bevatten grote hoeveelheden moleculair gas, en de infraroodstraling wordt hoofdzakelijk veroorzaakt door stervorming die kan oplopen tot een snelheid van 100-1000 zonsmassa's per jaar. Een theorie die al genoemd werd stelt dat uit zulke botsingen elliptische stelsels ontstaan; daarnaast is er een theorie die stelt dat deze botsingen een vaste volgorde doorlopen waarbij de verschillende stadia van de botsing de ULIRGs iets andere eigenschappen geven. Hierbij wordt onderscheid gemaakt tussen 'koele' en 'warme' ULIRGs, waarbij de 'warmte' bepaald wordt door verhouding tussen sterkte in lichtkracht aan de ene (korte-golflengte) en andere (lange-golflengte) kant van het infrarode spectrum. De warme ULIRGs hebben compactere kernen en stralen sterker dan de koele ULIRGs. Volgens de theorie zouden ULIRGs evolueren van koel naar warm en uiteindelijk zal het stelsel eruit zien als een zogenaamd Quasi-Stellair Object (een actief zwart gat).

Een mogelijk scenario is dat, terwijl het gas snel naar het centrum van de botsing stroomt en daar een starburst veroorzaakt, in het centrum van de botsing tegelijkertijd een zwart gat ontstaat. Beide processen gebruiken het gas, de starburst door er sterren van te vormen en het zwarte gat door het op te slokken en zo aan te groeien (dit wordt ook wel een actieve kern genoemd, of Active Galactic Nucleus, AGN). Op een gegeven moment wordt het zwarte gat zo groot dat het de stervorming tegenhoudt, het gas en stof die het licht van de actieve kern tegenhielden worden weggeblazen en deze kern wordt zichtbaar. In het begin van dit proces is er meer licht-absorberend stof en gas dat ervoor zorgt dat de ULIRG er koel uitziet, waarna dit opgebruikt en opgeslokt wordt zodat deze steeds warmer wordt. Tegelijkertijd groeien dus zowel de sterrenmassa als het zwarte gat. Dit is interessant, omdat studies hebben aangetoond dat er een in elliptische stelsels een relatie bestaat tussen de massa van het centrale zwarte gat en de massa van de sterren, die dus op deze manier tot stand zou kunnen komen.

We hebben een zestal ULIRGs geselecteerd, van koel tot warm. Het doel was om te kijken of we sporen konden vinden van evolutie: kwalitatief door te kijken in welke mate het stadium van de botsing overeenkwam met de koelte/warmte, en kwantitatief door het snelheidsveld te bepalen en hieruit de massa en de massa/lichtkracht-verhouding te bepalen en daarmee de leeftijd. De ULIRG Arp 220 wordt apart gesproken, voornamelijk omdat dit stelsel ten opzichte van de andere ULIRGs erg dichtbij staat en daardoor in detail te bestuderen is.

Hoofdstuk 3: De meest dichtstbijstaande ULIRG, Arp 220 Dit is een koele ULIRG met een betrekkelijk kleine afstand van 250 miljoen lichtjaar. In het centrale deel van de botsing zien nog de twee afzonderlijke kernen van de oorspronkelijke stelsels (de sterren). In beide kernen vindt stervorming plaats, maar het snelheidsveld laat zien dat het moleculaire gas van de stelsels al is samengegaan en ronddraait in een enkele schijf. We hebben de massa binnen het waargenomen gebied bepaald door middel van twee onafhankelijke methodes. Eerst door een model te maken van het snelheidsveld van het gas, waarbij rekening is gehouden met een aandeel sterren en een aandeel gas. Vervolgens hebben we het snelheidsveld van de sterren ingevoerd in een model dat ook voor elliptische stelsels gebruikt wordt. Hoewel in dit geval beide ster-kernen nog zichtbaar zijn, komen de massa's zeer goed overeen. Hiernaast hebben we de verhouding tussen massa en lichtkracht gemeten, en deze gebruikt om de leeftijd van de starburst te bepalen. De massa/lichtkrachtverhouding (of M/L) in het nabij-infrarood die wij vonden is klein, veel kleiner dan bijvoorbeeld die van elliptische stelsels.

Hoofdstuk 4: Ster-dynamica van ULIRGs Op dezelfde manier als beschreven voor Arp 220, zijn voor 5 andere stelsels ook de snelheidsvelden van de sterren in kaart gebracht en is de massa bepaald met behulp van het elliptische stelsel-model. We vonden weer lage waarden voor de massa-lichtkrachtverhouding. Er werd geen verband gevonden tussen kleur en M/L .

Hoofdstuk 5: Gas-dynamica van ULIRGs In hoofdstuk 5 worden de snelheidsvelden van het gas beschreven van dezelfde stelsels als in hoofdstuk 4. Naast Arp 220, komen de massa's van 2 andere stelsels ook goed overeen met de bepalingen uit de sterodynamica, maar voor 3 stelsels vallen de waarden anders uit. Dit geeft aan dat beide methodes niet zonder meer gebruikt kunnen worden. We hebben uitgezocht welk model de voorkeur verdient, dit verschilt per stelsel om verschillende redenen. Weer vonden we geen verband tussen massa/lichtkracht-verhouding en kleur/warmte. Het is belangrijk bij zulke metingen de onzekerheden in het oog te houden: hierin beschouwen we twee grote factoren. Ten eerste is dit de mate waarin het licht wordt tegengehouden door bijvoorbeeld stofdeeltjes en gas (extinctie), waarbij we wel een poging doen deze te bepalen maar het zou kunnen zijn dat deze ruim onderschat wordt. Ten tweede is de orientatie van de draai-as van het snelheidsveld (de inclinatie) van belang, en die is moeilijk te bepalen. De inclinatie heeft invloed op de schatting van de massa, en de extinctie op de berekening van de lichtkracht. Deze onzekerheden in aanmerking genomen, zullen de gevonden waardes van M/L nog steeds laag zijn ten opzichte van de elliptische stelsels waar ze naartoe evolueren. We concluderen ook dat ULIRGs niet zullen evolueren tot grote elliptische stelsels, zoals wel werd beweerd, maar in elliptische stelsels van middelmatige omvang.

4. De toekomst van dit onderzoek

Er is nog veel te bereiken in deze onderzoeksrichting. In onze data zit nog veel informatie die we niet gebruikt hebben voor dit proefschrift. In de spectra van de ULIRGs zitten bijvoorbeeld verschillende spectraal-lijnen van moleculair waterstof die meer inzicht kunnen geven in de lokale omstandigheden. De voorgestelde evolutie van koele ULIRGs naar warme ULIRGs zal nog verder onderzocht moeten worden. De kracht van 'integral field'-spectroscopie (met adaptieve optica) is bij zulk onderzoek essentieel voor de kwaliteit van de resultaten. De volgende stap hierin is bijvoorbeeld het bepalen de verhouding tussen de massa van het gas en de massa van de sterren. Deze massa's hangen voornamelijk af van de eigenschappen van de afzonderlijke stelsels vóórdat deze in botsing kwamen, maar de verhouding $M_{\text{gas}}/M_{\text{sterren}}$ zou moeten afnemen omdat het gas wordt opgebruikt en nieuwe sterren worden gevormd. Het zou de moeite waard zijn om dit in de nabije toekomst te bestuderen voor een voldoende grote selectie van ULIRGs.

Curriculum vitae

Op 10 december 1977 werd ik geboren in Nieuw-Dordrecht, een dorp in de buurt van Emmen. Van 1989 tot 1995 bezocht ik de gemeentelijke scholengemeenschap (GSG) in Emmen, maar ik bracht ook veel tijd door op de muziekschool en achter de piano. De studiekeuze was erg moeilijk; het liefst wilde ik filosofie gaan studeren, maar de slechte beroepsperspectieven hebben me hiervan weerhouden. Daarnaast vond ik bijna alles wel interessant. Na jaren geroepen te hebben dat ik géén dokter wilde worden, begon ik in september 1995 aan een geneeskundestudie in Groningen.

Na twee jaar, in 1997, wist ik weer dat ik géén dokter wilde worden en miste ik de exacte vakken zó, dat ik stopte met geneeskunde en begon met sterrenkunde. Naast mijn studie heb ik actief geroeid bij studentenroeivereniging Gyas, en in de avonden heb ik toch nog wat filosofievakken kunnen volgen. In het kader van een klein onderzoek heb ik waarnemingen gedaan van variabele sterren met de Jacobus Kapteyn Telescoop op La Palma, en in september 2004 studeerde ik af op het gebied van simulaties van grote schaalstructuren van het heelal. Daarna werkte ik ruim een half jaar bij uitgeverij Wolters-Noordhoff, heb ik drie maanden gereisd in Zuid-Amerika (Peru, Chili en Paaseiland) en bivakkeerde ik een tijdje in Californië, tot ik tegen een zeer interessante promotieplaats aanliep en besloot dat ik dus tóch doctor wilde worden.

In februari 2006 begon ik in Leiden aan dit onderzoek naar extreme starburst-stelsels bij Dr. Paul van der Werf, waarvoor ik drie keer ben afgereisd naar Chili om waarnemingen te doen met de Very Large Telescope op Cerro Paranal. Ik heb mijn werk gepresenteerd op conferenties in de oosten en het westen van de Verenigde Staten, en in Duitsland, en ik ben twee keer op werkbezoek geweest bij Nadine Neumayer bij ESO in Duitsland. Tijdens dit promotie-onderzoek kreeg ik een dochter en een zoon.

In september 2011 ben ik begonnen bij softwarebedrijf Topdesk in Delft, op de afdeling support.

Nawoord

Begin 2006 kwam ik van Groningen naar Leiden voor dit promotie-onderzoek. Reinoud, als eerste bedankt, want een betere woning (“naast de Pieterskerk, tegenover La Bota”) had ik me niet kunnen wensen. I would like to thank ESO for making it possible for me to travel three times to Paranal. Thanks to the team that kept up the Laser Guide Star at Paranal during my observations, this has been hard work. Nadine, thank you for teaching me about dynamical modelling and for your warm hospitality during my stays in Garching. Op de Sterrewacht heb ik veel mensen zien komen en gaan. Lottie, bedankt voor al je SINFONI-wijsheid. Leonie, ik ben het met je eens, jammer dat we niet meer samen hebben kunnen doen. Marissa, you’ll be the new SINFONI-expert, good luck with your thesis. Thank you for the (outside) kantine-lunches, the occasional ‘good coffee’ and more fun outside astronomy: Dominic, Stijn, Isa and Simon. Isa & Elisabetta, thank you for your friendship, the early biking sessions and for a most memorable beach walk. The last few years I’ve been running around the STRW in a much less social way; Nikta, Nadine, Emily, Brent, Jeanette, Jo, Ilse, Edo, Rowin and Jelte, thanks for being able to stop me in the corridor for a nice chat once in a while. Ilse bedankt voor alle kleertjes! Anne-Marie, bedankt voor de muzikale noot. Thanks for the good company, office-mates: Elisabetta, Niels, Demerese, Caroline (2x), Carl and Bas. Chris, bedankt voor je gezellige bezoeken aan Leiden. Brent, Dominic, Isa and Cat, thanks for helping me move! Cat, thanks for the furniture, the fridge and the enormous amount of tea, and for good conversations and a very special new year’s party in Chile. Teffie er gaat natuurlijk niks boven Grunn, maar leuk als je weer in de buurt komt wonen! Enja, tweemaal zwanger worden tijdens je promotie is niet niks, ik heb er veel bewondering voor. Veel succes met je laatste hoofdstuk! Laura, bedankt voor de leuke etentjes, doen we gauw weer. Jeroen en Hajni, het is altijd dolle pret met jullie. Renée, laten we binnenkort weer eens afspreken. Leonard, bedankt voor je aanstekelijke enthousiasme voor de muziek, ik hoop gauw weer eens aan te sluiten bij het Luisterrijk of een concert van het Orion ensemble. Marga, bedankt dat je -ondanks de mexicaanse griep- mijn eerste kind op de wereld hebt gezet!

Heleen, Nico, Suzanne, Reijer, Govert, Lisanne, Anna en Sebastiaan, jullie zijn altijd lief voor me; bedankt voor alle steun! Opa Henk, Oma Els, Opa Nico en Oma Heleen, speciaal bedankt voor de geweldige oppas.

Lieve Milou en Tom, jullie waren erbij. Bedankt voor de gezellige tijden binnen en buiten mijn buik. Ik ben ontzettend trots op jullie!

Bedankt Hein, nogmaals, voor het uitnodigen van Ronald en mij voor je afstudeerfeest; gelukkig sloeg onze honderduizendste ontmoeting wél aan! Ronald, je bent de liefste die ik ken. Bedankt dat jij hier bij mij bent!

